UNIVERSITÀ
DEGLI STUDI
FIRENZE

Development and implementation of a novel kinaesthetic Hand Exoskeleton System

A dissertation submitted in partial fulfillment of the
requirements for the Degree of Doctor of Philosophy
in

INDUSTRIAL ENGINEERING
Scientific Disciplinary Sector ING-IND/13

Candidate	Advisor
Lorenzo Bartalucci	Prof. Benedetto Allotta

Co-advisor	Coordinator
Dr. Alessandro Ridolfi	Prof. Giovanni Ferrara Giovanni Ferrara

Department of Industrial Engineering
University of Florence
Florence, Italy

XXXV Ph.D. Cycle - Years 2019/2022

To my family, and Sara

Tons of people have my gratitude for their contribution to my experience at the University of Florence during the last three years.

Firstly, I would like to express my gratitude to Prof. Benedetto Allotta that introduced me to the world of robotics. Thanks to him, I had the opportunity to work in this field for three years, making a long-lasting wish come true.

Special thanks go to my co-advisor, Dr. Alessandro Ridolfi, for his advice, guidance, and time. I would like to sincerely thank you for trusting me during these years and for your precious help in achieving the results reported in this thesis.

"Teamwork makes the dream work!"; a huge thanks goes to my lab mates: Alessandro, Jonathan, Andrea, Chiara, Leonardo, Edoardo, Alberto, Matteo F., Matteo B., Guido, Gherardo, Mirco, Lorenzo, and Nicola. The results of this thesis wouldn't have been possible without them. More friends than just colleagues, they have made these three years stimulating. I want to thank them for their support, for all they have taught me, and for all the fun we have had in these years.

My heartfelt thanks go to my parents and family, who supported and encouraged me during this challenging period. Mom and Dad are the ones who made it possible to start and conclude this journey. My sisters, Valentina and Francesca, have always been close to me by making me feel loved and appreciated.

Thanks to my girlfriend, Sara, who has supported me daily during these years; she has shared with me the joys and the tough times.

Finally, I would like to thank all my friends, who have made these years great and amusing.

Thanks to all the people mentioned here for shaping the person I am!

Lorenzo Bartalucci. University of Florence, January 2023.

In the new *Industry 4.0* era, digitalization and automation are the turning points to address rapidly changing challenges, such as tackling the limited availability of resources and improving the efficiency and sustainability of the industry. The thrust of this movement has pointed to the essential importance of developing new technologies to collect, understand and use the enormous amount of data created. This revolutionary wave also took root in the healthcare industry, leading to the so-called *Health 4.0*, based on smart machines to provide better, more value-added, and more efficient healthcare services to patients. This scenario made Robotics for Medicine and Healthcare products and innovative robot-augmented therapies a hot research topic. In this context, the research and development of an exoskeleton designed to enhance rehabilitation augmented with virtual reality applications have a potentially considerable social impact, representing cutting-edge technology.

The presented work dwells well with the subject by describing the mechatronic design process of a kinaesthetic hand exoskeleton system meant to reproduce proprioceptive stimuli coming from the interaction with a virtual reality. The presented prototype is a modular device, equipped with force and pose sensors, and driven by a Bowden-cable-based remote actuation system. Unlike similar devices, the proposed exoskeleton is specifically thought for virtual reality interaction and is designed to be reversible while exerting up to 15 N per finger. For a more accurate rendering of kinaesthetic finger stimuli, a procedure for reconstructing HMI force as a function of measured force and position signals by employing a system's kinematic and dynamic model is presented, detailed, and followed by some preliminary tests. The results showed that the model can trace forces back to the end-effector with a good performance in replicating the force-profile trend and a percentage error of the force module between 1.2 and 15%. Moreover, this work faced the design of the software architecture issue, along with a dedicated graphical user interface for real-time control and monitoring of the system, and a serious game to stimulate and train the sensorimotor apparatus necessary to perform the kinaesthetic gesture of spherical closing grasping.

The main contribution of this activity is hence not only to propose a novel hand exoskeleton prototype for kinaesthetic and virtual reality purpose but also to provide a detailed explanation of its implementation into a real device.

Contents

1 Introduction **1**
1.1 Overall framework . . . 3
1.2 State of the art . . . 4
1.2.1 State of the art discussion . . . 7
1.3 Contribution and thesis structure . . . 8

2 MDM Lab background **11**
2.1 Finger exoskeleton kinematic . . . 11
2.2 Kinematics optimization algorithm . . . 17

3 Hand Exoskeleton design **23**
3.1 Modular design . . . 24
3.1.1 The Base Platform . . . 25
3.1.2 The Interface Module . . . 27
3.1.3 The Finger Module . . . 28
3.2 Detection of HMI force orientation . . . 32
3.3 FM kinematic model . . . 34
3.4 FM dynamic Model . . . 37
3.4.1 Forces analysis of the FM-IM coupling . . . 41
3.5 Structural analysis . . . 44
3.5.1 Stress analysis . . . 44
3.5.2 Stiffness analysis . . . 49
3.6 HMI-force filter . . . 51
3.6.1 Analytical evaluation of the HMI-force filter . . . 53

4 RAS design **57**
4.1 RAS mechatronics design 57
4.2 The final RAS mechanical layout 61
4.3 The microcontroller firmware 62

5 HES software **65**
5.1 Software architecture 65
5.2 Digital PID algorithm 68
5.3 Finger GUI 71
5.4 Catch the mole application 74

6 Test and evaluation **77**
6.1 Assessment of the quick-magnetic couplings 77
  6.1.1 Discussion of the modular design results 78
6.2 Adjustable bracket 79
6.3 Minimum backdrive force 80
  6.3.1 Discussion of the system backdrivebility results 80
6.4 Dynamic model validation 81
  6.4.1 Discussion of the dynamic model results 83
6.5 HMI-force filter evaluation 85
  6.5.1 Discussion of the HMI-force filter assessment 86
6.6 Test case assessment 87
6.7 Pilot test at Don Carlo Gnocchi Foundation 88

7 Conclusions **91**

References **96**

List of Figures

1.1 An overview of the HES presented during functioning via the custom-developed *Finger GUI* and *Catch the mole* application. . . 8

2.1 Hand exoskeleton susyems evolution in MDM lab since 2013. . . 12
2.2 The main components that comprise the MDM kinematic architecture. 13
2.3 Lateral view of the finger mechanism and the corresponding reference systems used to kinematics analysis. 14
2.4 Joint trajectories of the 1-DOF finger mechanism. 17
2.5 Marker position protocol. 19
2.6 motion analysis camera setup. 19
2.7 Graphical representation of the error between computed and reference trajectories. 20

3.1 The proposed solution based on modular design. 25
3.2 The BP module for the thumb is on the left, the BP for the long finger is on the right. 26
3.3 Main components for FM-BP coupling. 27
3.4 An overview of the IM. 28
3.5 FM kinematic chain. 29
3.6 To the left is shown the maximum opening configuration,and to the right the maximum closing configuration. 30
3.7 The exploded view of the FM. 31
3.8 Procedure to measure the orientation of the interaction force by digital goniometer on the left, and by exploiting the software Kinovea on the right. 33

3.9 Directions of the interaction force as a function of the crank angle. The G_i plot shows the measurements of the i-th subject performed with the digital goniometer, while the K_i plot shows the measures of i-th subject extrapolated with Kinovea software. The reported angle values are expressed in deg. 34
3.10 Lateral view of the FM mechanism and the corresponding kinematic chain. 35
3.11 The local reference systems, h, c, a, z, and b, with respect to which the reaction forces applied to the H point, C point, A point, Z point, and B point were calculated. 41
3.12 The scheme of forces due to the interaction between the IM and the FM. 42
3.13 The wire-capstan contact during the functioning. 42
3.14 The complete rear crank set of loads. 43
3.15 The force values of interest for structural analysis as the crank angle changes (q_{18}). 45
3.16 The values of the static torque module required in Z (T_Z) as the crank angle changes (q_{18}). 46
3.17 The load and constrain set applied as boundary condition to fem analysis for the von Mises stress detection. 47
3.18 The von Mises stress diagram resulting from fem analysis, with stresses at increasing magnitude from elements colored in blue to those in red. 48
3.19 The load and constrain set applied as boundary condition to fem analysis for the stiffness analysis. 49
3.20 ΔE_1, ΔE_2, and ΔE_3 are the displacements of the E point under the application of force profiles of subject 1, subject 2, and subject 3 respectively shown in Figure 3.9. 50
3.21 the best fitting polynomial of the K points collected in the Table 3.5. 52
3.22 the average values of absolute error (e_a) committed to estimate the module of the end-effector force ($|F_E|$) by HMI-force filter as the force intensity changes. 54
3.23 the max values of absolute errors (e_{max}) committed to estimate the module of the end-effector force ($|F_E|$) by HMI-force filter as the force intensity changes. 55

4.1 Components constituting RAM. 58
4.2 lateral and top view of the RAM capstan. 59

4.3 A RAS overview including two RAM mounted. 60
4.4 An overview of the system electric/electronic scheme. Red lines symbolize power cables, blue lines symbolize USB cables, green lines symbolize Inter-Integrated Circuit (I2C) cables, orange lines symbolize Ethernet cables, and purple lines represent analog cables. 61
4.5 frontal view of the final RAS layout. 62

5.1 Summary diagram of the communication flow existing in the system and managed by the software architecture. 68
5.2 The blue line represents the encoder measurement, while the red line represents the reference value to be tracked. 70
5.3 The blue line represents the HMI-force value, while the red line represents the reference value to be tracked. 71
5.4 An overview of the *Finger GUI* with colored frames highlighting the various panels. Specifically: the setting panel, in green; the control panel, in red; the data logger panel, in orange; the graphics area, in blue; the graph control panel, in yellow; and the text box, in white. 72
5.5 An overview of the four pages of the Control panel. Each layout results from pressing the button highlighted with the red frame. . 74
5.6 Opening scene of the *Catch the mole* application. 75
5.7 A progressive sequence of the digital mole capture procedure. Subfigure a depicts the initial phase of the capture, b the reaching of the red disk of the avatar with the captured mole, c the release of the mole within the red disk, and d the point assignment and respawning of the mole to a new location. 76

6.1 The mean time (s) required by the five different subjects for the completion of FM-IM and FM-BP couplings. 78
6.2 The custom bracket equipped with a adjustable orientation basement. 79
6.3 The measured backdrive force in N, as a function of crank angle (q_{18}) in deg, with a Bowden cable pretension between 2-3 Kg. . . 81
6.4 Force measured at joint H by the load cell ($\hat{H}$). The number in superscript indicates the corresponding load in kilogram applied. 83
6.5 The dashed red line is the H-reaction profile measured; the green one, is the H-reaction calculated by the dynamic model. 84

6.6 The module of the interface Force estimated by HMI-filter ($\hat{F_E}$) in Newton. The number in superscript indicates the corresponding load in kilogram applied to the end-effector. 86
6.7 Interaction force tracking during two captures in the Catch the Mole application. The green lines shows the force measured by the exoskeleton, while the red line indicates the reference signal. 88
6.8 Pilot test at Don Carlo Gnocchi Foundation Rehabilitation Center. 89

Acronyms

ABS	Acrylonitrile Butadiene Styrene
BMIFOCUS	Brain Machine Interface in space manned missions: amplifying FOCUSed attention for error counterbalancing
BP	Base Platform
CAD	Computer Aid Design
CAE	Computer Aid Engineering
DIEF	Department of Industrial Engineering
DIP	Distal InterPhalangeal
DoF	Degree of Freedom
FM	Finger Module
GUI	Graphic User Interface
HES	Hand Exoskeleton System
HMI	Human Machine Interface
I2C	Inter-Integrated Circuit
IM	Interface Module

IP Internet Protocol

MCP MetaCarpoPhalangeal
MDM Mechatronics and Dynamic Modeling

PEEK Polyether Ether Ketone
PID Proportional Integral Derivative
PIP Proximal InterPhalangeal

RAM Remote Actuation Module
RAS Remote Actuation System
RoM Range of Motion
RPM Revolutions Per Minute

SISO Single Input Single Output
SMA Spinal Muscular Atrophy

TIP Toe InterPhalangeal

UDP User Datagram Protocol
USB Universal Serial Bus

VR Virtual Reality

Nomenclature

$\boldsymbol{Fx_{Pi}}$	the x-component of the of the external force vector applied on Pi
$\boldsymbol{Fy_{Pi}}$	the y-component of the of the external force vector applied on Pi
$\boldsymbol{T_{Pi}}$	the torque applied on Pi
$\boldsymbol{V}$	the potential function of the system
$\boldsymbol{\beta}$	the angle describing exoskeleton and finger trajectories (ρ, ρ^x) in polar coordinates
γ	the scaling coefficient of the mean error within the objective function concerning the maximum error for the kinematic optimization algorithm
$\boldsymbol{\partial w}$	the virtual work of the generalized coordinates
$\boldsymbol{\partial x_{Pi}}$	the virtual displacements of Pi point along the x-axis of global reference system
$\boldsymbol{\partial y_{Pi}}$	the virtual displacements of Pi point along the y-axis of global reference system
$\boldsymbol{\rho^*}$	the reference trajectory of the medial phalanx midpoint
$\boldsymbol{\rho}$	exoskeleton trajectory
$\boldsymbol{\{S\}}$	the vector that collects geometric parameters of the system involved into optimization process
$\boldsymbol{\{\tilde{R}\}}$	the reaction forces vector
$\boldsymbol{e_k}$	k-th polar error between the reference trajectory of the finger and that of the exoskeleton

$[\boldsymbol{M}]$	the mass matrix
$[\boldsymbol{C}]$	the dumping matrix
$\left[\frac{\boldsymbol{\partial\Psi}}{\boldsymbol{\partial}\mathbf{q}}\right]$	the Jacobian matrix of the constraint vector
$\boldsymbol{\phi}$	the angle between link BC and link CE
$\boldsymbol{\theta_i}$	orientation of the i-th frame with respect to global frame
$\boldsymbol{\varphi}$	the angle between front crank HA and the link AC
$\boldsymbol{\{Gi\}}$	position vector of the origin point of the i-th local frame
$\boldsymbol{\{\Psi\}}$	the constrain vector
$\boldsymbol{\{\ddot{q}\}}$	the acceleration vector of the generalized coordinates
$\boldsymbol{\{\dot{q}\}}$	the velocity vector of the generalized coordinates
$\boldsymbol{\{\lambda\}}$	the vector that collects the Lagrange multipliers
$\boldsymbol{\{\tilde{F}\}}$	the generalized force vector
$\boldsymbol{\{q\}}$	generalized coordinate vector
$\boldsymbol{{}^{j}p_i}$	the i-th component of $\{p\}$ vector with respect to the j-th frame
$\boldsymbol{{}^{i}\{p\}}$	the $\{p\}$ vector with respect to the i-th frame
$\boldsymbol{l_i}$	mid-length of the i-th exoskeleton link
$\boldsymbol{R_i^j}$	rotation matrix of the i-th frame with respect to the j-th frame

Chapter 1

Introduction

The advent of the so-called *Industry 4.0* has raised digitalization and automation as the turning points to address rapidly changing challenges, such as tackling the limited availability of resources and improving the efficiency and sustainability of the industry. The industry's traditional concepts have been revolutionized by introducing a new attitude based on automation and data exchange, increasingly impacting all disciplines, economies, and industries, bringing a new perspective on Human Machine Interface (HMI) by demonstrating that humans and smart machines can now work together, safely, side by side, and even cooperate. This unstoppable movement has also radically reshaped the healthcare industry by prompting a technological revolution in this sector that has led to the coining of the term *Health 4.0* [1, 2, 3]. Ultimately the concept lies around the use of *Industry 4.0* technologies to provide patients with better, more value-added, and more cost-effective services while improving the healthcare industry's efficacy and efficiency. *Health 4.0*, thus, outlines a new and innovative vision for the health sector with smart machines that get access to large amounts of data. The unstoppable surge of this change has paved the way for the advancement of Robotics for Medicine and Healthcare as a powerful tool for enhancing assistive technology. This type of technology is intended as any product (including devices, equipment, tools, and software) that is used by or for people with disabilities to protect, support, train, measure, or replace bodily functions, structures, and activities, or to prevent impairments, activity limitations, or participation restrictions. This branch of robotics is "the domain of systems capable of performing coordinated mechatronic actions (force or motion efforts) based on the processing of information acquired through sensor technology to support people with disabilities". Examples of such systems are powered exoskeletons [4, 5], active prostheses [6, 7], or controlled robotic tools for surgery [8].

Robotics for Medicine and Healthcare solutions provide multiple assets over traditional ones. Having to "perform coordinated mechatronic actions", robotic devices generally incorporate an automatic control system to provide an intuitive and safe utilization. The control systems mentioned above are usually composed of hardware with computing power, such as processors, sensors, remote communication channels, and data storage capacity. The combination of these elements makes robotic devices capable of making possible new rehabilitative clinical paths, such as robot-augmented therapy combined with Virtual Reality (VR) technology [9, 10].

VR, defined as any simulation that allows interaction with a digital environment with which the human subject can interact by engaging one or more perceptive senses, is another rapidly expanding technology improved by the coming of *Industry 4.0*. Thanks to its vast potential, it is rapidly emerging as one of the primary tools to provide augmented HMIs, becoming prevalent in many applications, such as gaming, training [11, 12, 13], product review [14], simulation of industrial operations [15], teleoperation [16, 17, 18], and remote driving [19, 20]. In robot-augmented therapy, VR technology comes in the form of interactive video games, called serious games, specifically designed to train in active movements and refine motor control and coordination skills, improving user engagement. Therefore, in this application, a robotic device is required to provide and oversee the necessary therapy and to play the role of HMI within an interactive video game, increasing the complexity from an engineering design perspective.

However, despite the clinically proven effectiveness of robot-augmented therapy, its current state of the art still has many flaws since Robotics for Medicine and Healthcare is still a relatively new discipline, in the midst of research and development course and lacking a fully developed and dedicated industrial fabric.

The work conducted in the framework of the presented research activity was born to intervene in this issue, focusing on the development of a Hand Exoskeleton System (HES) for robot-augmented therapy designed to rehabilitate people with hand problems. From the engineering point of view, it represents a significant challenge both for the mechanical design and the control strategy because of the hand's complex anatomy, the high dexterity tasks, and the vast set of movements required. Despite these adversities, the proposed HES can replicate force references elaborated within a VR environment on the user's fingers to improve the user's sensorimotor and proprioceptive functions.

Throughout the thesis, all the technical aspects of the device will be presented and addressed, starting from the mechanical and electronic design to writing the software capable of applying the desired control strategy. In addition, a serious game, specially developed in Unity environment, designed for robot-augmented therapy, will also be introduced.

1.1 Overall framework

The research activity began in 2019 and was conducted at the Mechatronics and Dynamic Modeling (MDM) laboratory of the Department of Industrial Engineering (DIEF), University of Florence.

The MDM lab has been active in wearable robotics since 2013. In that year, the development of the very first HES prototype began, explicitly designed to meet the needs and requirements of a specific patient with Spinal Muscular Atrophy (SMA) for assisting him during daily activities. Although with some obvious limitations, this first version showed interesting features, such as a new 1-Degree of Freedom (DoF) exoskeleton kinematic architecture for finger movement. This structure was also applied in the development of the device under review.

In 2016, a collaboration with the Rehabilitation Center of the Don Carlo Gnocchi Foundation in Florence allowed for an expansion of the target group of possible device users. This scenario required adapting the mechanism introduced in 2013 to different patients' hands. Using the MoCap system available at the Don Gnocchi Rehabilitation Center, several hand kinematics studies were conducted to identify the trajectory of a point belonging to a finger concerning specific anthropometric measurements. In addition, a kinematic optimization algorithm was developed, which, depending on the anthropometric measurements of the designed user, allows the identification of the dimensions of the components of the exoskeleton mechanism that allows replicating a trajectory that deviates from the real one with the minimum error. In addition, the devices obtained through the kinematic optimization algorithm were subjected to specific experimental campaigns to evaluate their suitability and effectiveness, resulting in sufficient suitability for clinical or assistive use.

These results, part of the MDM lab's know-how, gave this thesis work a solid background to design the new prototype. Funding for its implementation was obtained from the italian project ”Brain Machine Interface in space manned missions: amplifying FOCUSed attention for error counterbalancing (BMIFOCUS)”, funded by the Tuscany Region and started in conjunction with this work in 2019. The BMIFOCUS project aim was to develop a training platform in a virtual environment to stimulate cognitive, sensory, and locomotor systems by employing multiple robotic systems to recreate the haptic perception of the entire arm sector. In this context, the device under consideration, integrated into the training platform, is tasked with simulating the interaction of the hand with various objects within VR.

1.2 State of the art

Since the 1980s, multiple robotic devices have been developed to replicate the human hand's functions in industrial robotics, telemanipulation, humanoid robotics, and Robotics for Medicine and Healthcare. One particular type of robotic hand is the hand exoskeleton, also known as an active orthosis. An exoskeleton is a mechanism placed around a human body part to mechanically guide it without impeding the natural motion of the human joint. Therefore, an HES is an actuated device directly connected to the human hand, where the movements of the robotic and anatomical systems are coupled through the exchange of forces and moments. The state of the art of exoskeleton hand devices claims a great variety, which differs widely in terms of degrees of freedom, range of motion, type of actuation, and design philosophy. Although the reasons for the development and design of HES can be multiple, in general, they can be grouped into three main functional sets, which result in significantly different design specifications based on the intended use: personal assistance, rehabilitation; and haptic use.

Assistive HESs are meant to be used in daily life activities by users with permanent hand diseases to assist them in performing gestures that would be difficult or even impossible without an active exoskeleton's support. Since they are to be worn for long periods, they are developed based on specific design criteria that significantly differentiate them from the other HESs; for example, the need to optimize fit and energy independence, leading to solutions in lightness, compactness, and efficiency, are mandatory features. In addition, for the most effective assistance, these devices must be able to acquire movement intentions from the user and, therefore, must be equipped with an appropriate sensor system. HESs for rehabilitative purposes are designed as exercise platforms with the task of having patients perform a specific, precise, and repeatable protocol of therapeutic exercises designed to recover the motor capacity, partial or total, of the hand. The rehabilitation exercise can be either a passive movement guided by the exoskeleton or an active movement against the resistance force exerted by the exoskeleton. Commonly, these devices are designed to maximize performance even at the expense of portability, considering that use is not continuous but limited to the duration of the rehabilitation session. A major advantage, offered by this type of device, is the ability to collect a wide variety of data on the training sessions performed, so that therapists can provide a more effective assessment of patients' progress and actual condition. The upcoming new purpose of haptics outlines HES as an intelligent device for human-machine interface in virtual reality applications. The new clinical pathway robot-augmented therapy has called for the development of devices that can combine the latter two fields of application, adding the difficulties for developing a rehabilitation device to those demanded by haptics.

In Robotics, haptics is defined as the "*real and simulated touch interactions between robots, humans, and real, remote, or simulated environments in various combinations*" [21]. In recent years, this field has been very prolific in terms of robotic devices aimed at augmenting human touch sensation in HMI. Haptic devices can be further classified according to the types of perception receptors they stimulate: kinaesthetic devices (force/position) and cutaneous devices (tactile) [22]. The human touch is the result of the combination of the force, position and tactile sensations.

The cutaneous devices are intended to simulate the tactile feel of objects interaction and usually act on the fingertips; the areas with more tactile receptors. In literature, many examples differ in the method of generating cutaneous feedback. The most commonly used approaches are vibrations [23, 24, 25], localized deformations [26, 27, 28], variable pressures [29] and three-dimensional force vectors on one or more contact points [30, 31]. These devices commonly operate with low forces (around 1 N) resulting in very compact and often wearable devices. On the other hand, kinaesthetic devices aim to stimulate proprioceptive receptors, the ones in charge of sending detailed messages to the brain about positions and forces. In order to communicate such sensations to the body, the forces involved are much higher than in the tactile applications, and such devices result in larger and bulkier systems and often involve external supports for grounding.

Several examples of upper-limb kinaesthetic [32, 33], and grasping [34, 35] platforms appear in the literature.

Lately, exoskeletons have originated a considerable fascination in researchers when it comes to force delivery and kinaesthetic systems. These devices, being wearable, allow for a more authentic replication of actions within the VR and, besides, leave the users with a great freedom of movements, resulting in an incredibly immersive experience. However, finding a fair balance between

VR rendering capability, the wearability of the resulting system, and the high performance required remains, to date, a stimulating challenge.

Achieving such a demanding trade-off becomes even more complicated when it comes to designing Hand Exoskeleton Systems due to the minimal space, the high number of DoF, and the articulated hand kinematics. Thus, the mix of the design problems — i.e., interfacing with a very complex anatomical morphology, combining high performance and portability constraints — has slowed the development of HESs with respect to that for other limbs [36, 37, 38, 39, 40, 41]. Despite the adversity, many HESs proposed in the literature are born as haptic platforms for the hand. The variety of these devices is wide; the criteria for differentiating them are no less: the most common are the number of DoF implemented, the type of kinematic architecture (rigid or soft), and type of actuation system.

In recent works, the increased demand for HESs portability has turned the research toward replacing the classic rigid-link-based kinematics with softer architectures similar to robotic gloves, known as soft gloves [42, 43, 44, 45].

The weight reduction and slimness of resulting devices are undeniable; however, these gains cost a less advantageous mode of force exchange than traditional rigid exoskeletons, resulting in a loss of performance. In addition, the interposition of a soft element between the force point and the user's limb is a source of delay in the system that risks undermining force-driven applications. This is why the layout of rigid-link-based exoskeletons is widely preferred in applications where force control is required.

As concern rigid HESs, in [46, 47, 48, 49, 50, 51, 52], the actuators are directly housed over the user limb to reach a wholly portable and wearable device. However, for weight and dimension-related constraints, a wearable-based design strategy has to inevitably compromise the amount of force exerted or the number of fingers controlled independently. Thus, this design philosophy poorly fits scenarios where maximizing performance is demanded. For these cases, the literature presents a wide range of devices developed through an utterly opposed design approach aiming to meet the most force-demanding application requirements through the rigid ground anchoring of the haptic platform [53, 54, 55]. A fully rigid transmission chain allows the ability to transmit forces at high frequencies from actuators to control points, typically where force signals are measured; this is essential for all very demanding real-time haptics applications, such as remote driving and teleoperation. Moreover, such platforms relieve the user of the entire exoskeleton weight, facilitating its use at the expense of losing many DoFs of the wrist and, hence, limiting their integration with more complex virtual reality where many hand DoFs are replicated.

The midpoint between these two opposing design strategies is embodied by those exoskeletons presenting an actuation system placed away from the user's body, typically known as Remote Actuation System (RAS)s. The use of flexible elements in the transmission chain inevitably results in lowering the system cutoff frequency; therefore, remote-actuated systems are not suitable for very accurate real-time haptic applications, but they can still offer satisfactory performance for less demanding applications, such as robot-assisted rehabilitation and gaming. A considerable number of RASs reported in the literature are based on hydraulic or pneumatic actuators [56, 57], but the most popular architecture is Bowden-cable-based [58, 59, 60] since it result less complex and bulky.

Bowden cables consist of an inner wire, typically made of steel, coated with a suitable sheath, and guarantee the transmission of high forces between the two ends of the internal cable, regardless of the relative positions of the cable extremities. Therefore, a Bowden-cable-based RAS ensures sufficient stiffness and high performance while allowing the user's hand to move freely in all spatial directions within a reasonable room determined by the cable length. Despite the many pros, the employment of Bowden cables involves many complications concerning control performance due to the friction between the sheath and the wire, which induces non-linearity, backlash, and consequently loss of precision.

1.2.1 State of the art discussion

Driven by tide of *Health 4.0* change, Robotics for Medicine and Healthcare technology is permeating and revolutionizing more and more healthcare field. New clinical pathways have emerged, demonstrating massive efficacy compared with traditional practices. Among them, robot-augmented therapy is considered one of the most promising applications, enhancing the user's engagement and the quality of the physiotherapeutic treatment offered. However, analysing the state of the art depicts a scenario heavily demanding innovative solutions for impaired human hand. This deficiency is mainly attributable to the need to integrate appropriate haptic feedback to rehabilitative devices for the hand.

Kinaesthetics is one of the two branches of haptics and deals with the rendering of proprioceptive sensations. Various systems aimed at kinaesthetic stimulation have been proposed in the literature, and among them, exoskeletons occupy a place of honor.

As regards soft gloves and fully-wearable rigid exoskeletons offer great portability but can exert limited forces (usually less than 10 N per finger). Conversely, grounded exoskeletons exploit complex architectures to exert high forces, drastically jeopardizing their portability. RAS-based systems represent a good trade-off between portability and performance but the available solutions focus more on kinematic accuracy than on force rendering.

1.3 Contribution and thesis structure

The research activity during the Ph.D. period focused on the development of a new prototype exoskeleton for the hand (see Figure 1.1) as a tool for robot-augmented therapy. Such a HES shall be capable of reproducing kinaesthetic interaction within a serious game developed for physiotherapy rehabilitation, aiming to contribute to the enrichment of the extremely poor state of the art on the subject.

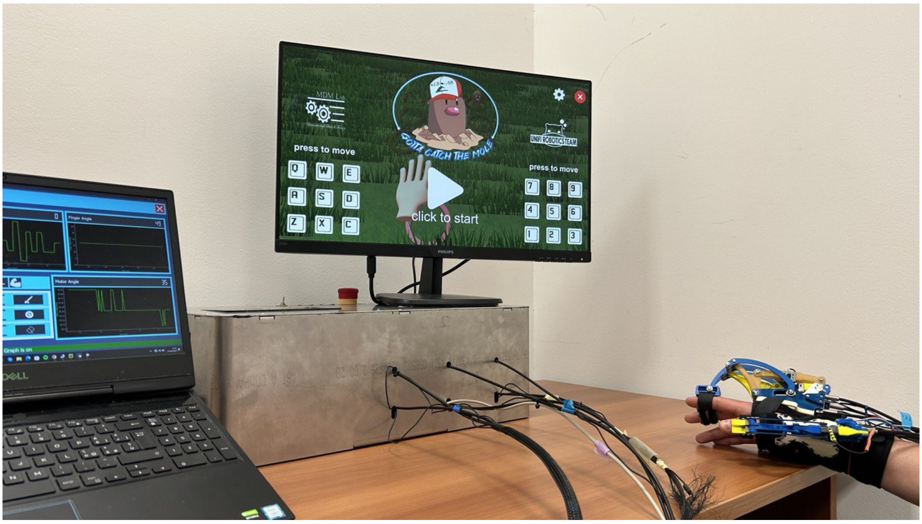
MDM Lab
GOTTA CATCH THE MOLE
UNIFI ROBOTICS TEAM
press to move
Q W E
A S D
Z X C
click to start
press to move
7 8 9
4 5 6
1 2 3
Finger Angle
Motor Angle
Graph is on

Figure 1.1: An overview of the HES presented during functioning via the custom-developed *Finger GUI* and *Catch the mole* application.

Particular attention was dedicated to studying mechatronic design and control strategies for kinaesthetic haptic exoskeletons.

The first phase of the research involved the analysis of the existing scientific literature and the state-of-the-art hand exoskeleton solutions (and their limitations) in identifying useful features and those that could be subject to improvement. This analysis suggested the need to develop a force-controlled device that provides complete freedom of movement at the wrist while burdening the user's limb as minimally as possible. In addition, the prototype must also satisfy the usual requirements for a rehabilitation device and, consequently, be capable of effectively rehabilitating a wide range of anthropometric measurements due to frequent user change.

During the-state-of-the-art analysis, the greatest-interest technical features were evaluated to set design goals to ensure high-level and competitive performance compared with existing technology. Specifically, a nominal force up to 15 N per finger was chosen as the benchmark for mechanical design. This threshold value generates a sustained grasping force in line with the maximum achievable by the fifth percentile of the healthy male population, according to data collected by NASA [61]. Moreover, mechanical reversibility was chosen as a priority feature among the main technical specifications, as the device must actively interact with the human body. A mechanically reversible device has several advantages: high efficiency and, therefore, low power losses in the drive chain; a simplified wearing phase that can be performed with the motors off; the possibility of detecting user interaction from any point of the mechanism using appropriate sensors (force/position); and safe emergency management, since in case of malfunction the user can always force the device once the motors are turned off by using the emergency button. This feature is strongly pursued in industry, and especially in healthcare field.

A remote actuation system with a Bowden cable-based transmission was identified as the ideal layout to achieve all the above-mentioned design constraints: a desired force delivery up to 15 N per finger, an independent actuation for each finger, a free moving into three spatial dimensions of the user's hand, and a limited exoskeleton's encumbrance and weight burdening the user's limb. In addition, adequate sensors have been implemented in the exoskeleton mechanism to enable force driving during interaction with a VR. In detail, the exoskeleton is designed to monitor the hand pose (i.e., finger positions and velocities) and send this information to the virtual environment to guide the movement of a virtual hand within it. In turn, the VR application, as the virtual hand interacts with it, calculates the interaction forces and sends them back to the system so that the exoskeleton can apply them to the real hand.

This thesis will deeply cover all the aspects of the mechatronic design process carried out to produce the actual prototype aiming to provide a useful reference in terms of design methodology. The thesis is organized as follows. Chapter 2 outlines the MDM lab know-how from which the current research activity started to design a clinically safe and reliable device. The Chapter 3 presents the hand exoskeleton part of the system in detail, describing the proposed solution from a mechanical perspective, highlighting the functionality of the design criteria adopted; the position of the sensors introduced within the kinematic chain; the kinematic and dynamic models of the proposed mechanism; the static-structural analysis performed; and the formulation of the HMI force filter, for a higher quality rendering of the HMI force. The overall architecture of the RAS is detailed in Chapter 4, disclosing the mechanical prospective, electronic hardware, and the local network communication adopted to pick up and process the force and position signals. The manuscript continues with Chapter 5 that presents the design of the software architecture, along with a dedicated Graphic User Interface (GUI), named *Finger GUI*, for real-time control and monitoring of the system, and a serious game, called *Catch the mole*, to stimulate and train the sensorimotor apparatus necessary to perform the kinaesthetic gesture of spherical closing grasping. Chapter 6 describes the experimental campaigns conducted on the prototype, designed to derive some crucial characteristics of the system to validate the design methodology applied to pursue the desired technical specifications, and assess the accuracy of the models proposed to improve VR interaction experience. Finally, Chapter 7 concludes the work.

Chapter 2

MDM Lab background

The two main scientific achievements of MDM lab in the research and development of assistive hand exoskeletons will be presented and described in this chapter to provide the reader with the necessary tools for a more informed and in-depth vision of the work undertaken. And as such, this thesis work made use of MDM lab results and from which the design of the new kinaesthetic prototype started. Section 2.1 will describe the analysis and synthesis kinematic of the 1-DoF finger exoskeleton capable of reproducing the complex finger kinematics without being forced to use an equally complex device, resulting in a successful mechanism in terms of functionality and manufacturability. Section 2.2 briefly reports the theory behind the kinematic optimization algorithm, discussed in more detail in [62]. The algorithm under consideration makes it possible to derive the geometric characteristics of the mechanical components presented in Section 2.1 as a function of specific anthropometric quantities so that the resulting optimized finger exoskeleton follows the natural finger trajectory at best.

2.1 Finger exoskeleton kinematic

The finger exoskeleton mechanism under consideration was first introduced in 2013 by MDM lab with the invention of the very first hand exoskeleton prototype, developed to move both the medial and distal phalanges simultaneously. That device highlighted an promising potential and was so successful that it remained the core of the development of all succeeding prototypes. Four devices were developed since then, as shown in Figure 2.1, each designed to meet different research needs, but all were essentially equipped with the same finger mechanism, which was subject to improvement during the evolutionary process. This process was oriented toward the single-phalanx approach that involves a single point of interaction between the mechanism and the corresponding finger situated in the middle of the medial phalanx. Ultimately, with this approach, a reduction in the number of components of the rigid kinematic chain was achieved, renouncing the distal phalanx actuation. The compromise is considered favorable in that this reduces cost, weight, and encumbrance without making spherical grasping less effective.

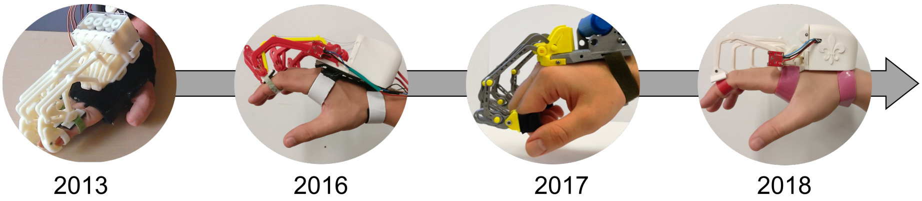

Figure 2.1: Hand exoskeleton susyems evolution in MDM lab since 2013.

The Figure 2.2 shows the components that make up the considered mechanism in detail. Essentially, it is a kinematic mechanism generated by the rotation of the AC link that, via an internal hinge located at point C, causes a rototranslation of the BCE link, whose point E represents the end-effector of the system, as well as the point of interaction with the medial phalanx of the user. The mechanism uses a third component called the finger frame that realizes a hinge constraint at point A and a combined slider-hinge constraint at point B.

It is important to point out that varying the key geometric characteristics of these three components, such as the length of the links, the length or inclination of the slider, and the relative distances between constraints, allows for infinite E-point trajectories. Thus, it is evident that the design of an exoskeleton that aims to replicate at the end-effector an imposed trajectory similar to that of human fingers cannot be exempted from the system kinematic analysis. For analytical simplicity, the system was modeled as a planar kinematic chain, and the BCE link was divided into two rigid links (BC-CE) and three congruent constraints that ensure rigid displacements between them added. Thus, the kinematic model of the system consists of the 3 links in total: AC, BC and CE links; for a total number of unconstrained DoFs of 9 (3 per component).

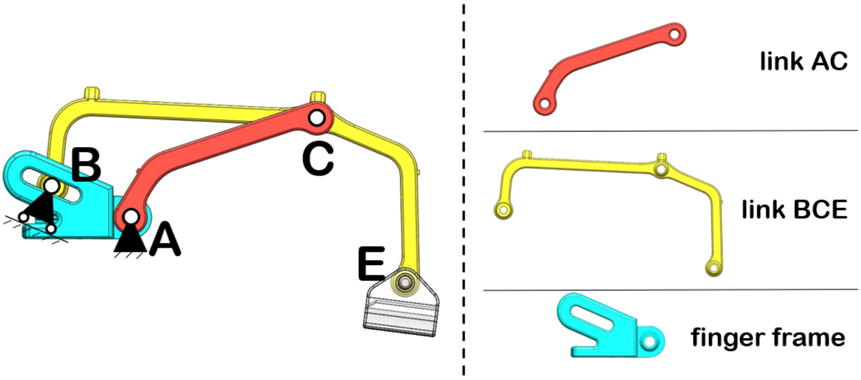

Figure 2.2: The main components that comprise the MDM kinematic architecture.

The first step in building the kinematic model includes the definition of appropriate reference systems. As shown in the Figure 2.3, a fixed global reference system was set at point A, and it will be referred with the 0 index. Three local reference systems, one for each component, are attached with the x-axis having a direction coincident with that passing through the start and end link points. Each origin of the i-th local frame, Gi (with $i = 1 : 3$), is positioned at the mid-length of the i-th link, so that l_i denotes half of such length. Three variables are defined in the global reference system for each of the i-th frame: q_{3i-2}, the x-coordinate of the i-th origin ${}^0Gi_x$; q_{3i-1}, the y-coordinate of the i-th origin ${}^0Gi_y$; and q_{3i}, the counterclockwise angle, θ_i, between the local abscissa axis x_i and the global abscissa axis x.

The vector $\{q\} \in \mathbf{R}^9$ that collects these variables is defined as the generalized coordinate vector of the system and written as follows:

$$\{q\} = \begin{bmatrix} q_1 & q_2 & q_3 & \dots & q_9 \end{bmatrix}^\top \tag{2.1}$$

Before proceeding to evaluate the constraint system, it is necessary to define the generic orientation matrix R_i^0 describing the orientation of the i-th frame with respect to the global frame. Being a planar problem and θ_i the angle between the two interested frame, the orientation matrix can be written by

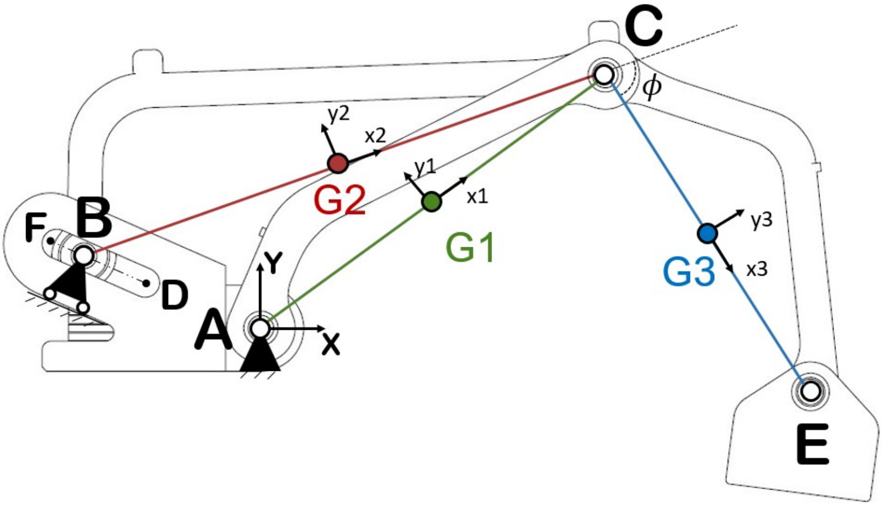

Figure 2.3: Lateral view of the finger mechanism and the corresponding reference systems used to kinematics analysis.

using generalized coordinates as follows:

$$R_i^0 = \begin{bmatrix} \cos q_{3i} & -\sin q_{3i} & 0 \\ \sin q_{3i} & \cos q_{3i} & 0 \\ 0 & 0 & 1 \end{bmatrix} \tag{2.2}$$

The next step in the kinematic analysis involves writing the constraint system containing the mathematical equations imposed by the external constraints that connect the generalized coordinates. The fixed hinge at point A locks two degrees of freedom by imposing that the coordinates of that point, seen as a point belonging to frame 1, integral with the AC link, constantly coincide with the origin of the global reference system. Thus such a constraint originates the following equations:

$$^0\{A\} = \begin{bmatrix} 0 \\ 0 \end{bmatrix} \tag{2.3}$$

The rotation matrix describing the orientation of the j-th frame with respect to the i-th (R_i^j)frame enables the generic vector $^i\{p\}$ to be expressed with respect to the different j-th reference system through the following property:

$$^{j}\{p\} = R_i^j \, ^{i}\{p\} \tag{2.4}$$

Applying the orientation matrix property described in the equation 2.4 to equation 2.3, the constrain equation of the fixed hinge A can be rewritten as:

$$R_1^0 \, ^{1}\{A\} = \begin{bmatrix} 0 \\ 0 \end{bmatrix} \tag{2.5}$$

The internal hinge at point C, which connects link AC with link BC, also constrains two degrees of freedom by imposing that the coordinates of point C from frame 1 coincide with the coordinates of the same point seen from frame 2. Writing this relationship with respect to the global reference system, the following constraint equations is obtained:

$$R_1^0 \, ^{1}\{C\} = R_2^0 \, ^{2}\{C\} \tag{2.6}$$

The same line of reasoning applies to the other internal hinge at point C that connects the BC link with the CE link, thus obtaining similar constraint equations:

$$R_2^0 \, ^{2}\{C\} = R_3^0 \, ^{3}\{C\} \tag{2.7}$$

Since the BC and CE links are integral, the relative rotation is also locked, which in the constraint equation is expressed by placing the angle between the frames 2 and 3 constant, as given in the following equation.

$$\phi = cost \tag{2.8}$$

Finally, slide B blocks only 1 degree of freedom by imposing that point B can translate only along a straight line. The sliding line was defined by the conjunction of points F and D, as shown in Figure 2.3. This condition mathematically can be expressed by imposing that the determinant of the 3 x 3 matrix having for rows the 3 vectors describing the position of the points F, D, and B with the third coordinate equal to 1, is equal to 0, as given in the equation 2.9.

$$\begin{vmatrix} ^{0}D_x & ^{0}D_y & 1 \\ ^{0}F_x & ^{0}F_y & 1 \\ ^{0}B_x & ^{0}B_y & 1 \end{vmatrix} = 0 \tag{2.9}$$

Applying the equation 2.2 to equations 2.5, 2.6, 2.7, 2.8, and 2.9 packing them together yields the constrain system comprised an overall of 8 equations, as shown in Equation 2.10.

$$\begin{cases} q_1 - l_1 \cos q_3 = 0 \\ q_2 - l_1 \sin q_3 = 0 \\ q_1 + l_1 \cos q_3 - q_4 - l_2 \cos q_6 = 0 \\ q_2 + l_1 \sin q_3 - q_5 - l_2 \sin q_6 = 0 \\ q_4 + l_2 \cos q_6 - q_7 + l_3 \cos q_9 = 0 \\ q_5 + l_2 \sin q_6 - q_8 + l_3 \sin q_9 = 0 \\ q_9 - q_6 - \phi = 0 \\ d\left(q_5 - l_2 \sin q_6\right) + f\left(q_4 - l_2 \cos q_6\right) + h = 0 \end{cases} \tag{2.10}$$

where $d = {}^0F_x - {}^0D_x$, $f = {}^0D_y - {}^0F_y$, and $h = {}^0D_x{}^0F_y - {}^0F_x{}^0D_y$.
The system reported in Equation 2.10 can also be written defining the constraint vector $\{\Psi\} \in \mathbf{R}^8$ such that:

$$\{\Psi\} = \{0\} \tag{2.11}$$

It is worth noting that the constrain system (Equation 2.11) is composed of 8 equations in 9 variables (the components of the vector $\{q\}$), and has for solutions only $\{q\}$ vectors that respect the assigned constraints. Therefore, solving the system is equivalent to the resolution of the finger exoskeleton kinematics. Since the mechanism has 9 generalized coordinates and 8 constrained equations, the system globally results in a single DoF. Therefore, it is possible to manipulate the equations to derive 8 out of the 9 $\{q\}$ vector variables as an explicit function of one. In the context of this research work, q_3, which describes the link AC rotation, has been used as the control variable to calculate the mechanism pose by explicitly rewriting the constrain system as follows:

$$\begin{cases} q_1 = l_1 \cos q_3 \\ q_2 = l_1 \sin q_3 \\ q_6 = 2 \arctan\left(\frac{-b+\sqrt{b^2-4ac}}{2a}\right) \\ q_4 = 2l_1 \cos q_3 - l_2 \cos q_6 \\ q_5 = 2l_1 \sin q_3 - l_2 \sin q_6 \\ q_9 = \phi + q_6 \\ q_7 = q_4 + 2l_2 \cos q_6 + l_3 \cos q_9 \\ q_8 = q_4 + 2l_2 \sin q_6 + l_3 \sin q_9 \end{cases} \tag{2.12}$$

where $a = h + 2fq_1 + 2dq_2 + 2fl_2$, $b = -4dl_2$, $c = h + 2fq_1 + 2dq_2 - 2fl_2$.

Once all geometric parameters have been determined, and collected in vector $S \in \mathbf{R}^8$ (Eq. 2.13), the resolution of the system 2.12 enables to calculate the state vector and therefore all interesting points of mechanism. At this point, the motion is completely described and the relative positions of any joints is given. Figure 2.4 shows the trajectories of the joints, providing a qualitative overview of the resulted kinematics when the finger is actuated.

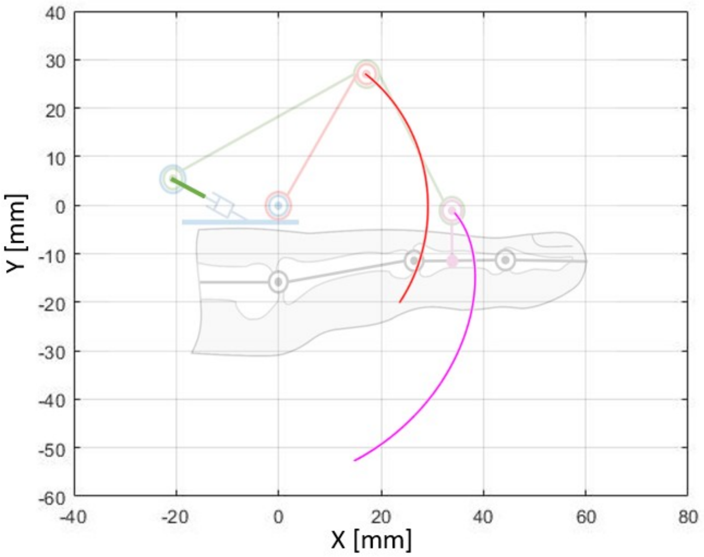

Figure 2.4: Joint trajectories of the 1-DOF finger mechanism.

$$\{S\} = \left[\begin{array}{cccccccc} l_1 & l_2 & l_3 & \phi & {}^0F_x & {}^0F_y & {}^0D_x & {}^0D_y \end{array} \right]^\top \tag{2.13}$$

2.2 Kinematics optimization algorithm

The kinematic chain of the MDM lab exoskeleton described in Section 2.1, like all rigid exoskeletons, allows to unequivocally determine the trajectory of the end-effector. Consequently, the choice of its geometric parameters is of crucial importance since once the exoskeleton is worn, the hand-device system becomes a closed kinematic chain, and the point of interaction is constrained to the dictated displacements by the rigid mechanism. If the imposed trajectory deviates from the natural one, the exoskeleton inevitably stresses the biological joints of the fingers. The soft tissues can absorb small deviations, but the larger the error, the more uncomfortable or even painful and inadequate for use the exoskeleton becomes. Therefore, the design philosophy of an exoskeleton that mounts this type of rigid kinematics is to determine a set of geometric parameters that can make the exoskeleton reproduce a trajectory similar to that reproduced by the user's finger. Thus, the MDM lab finger exoskeleton evolution naturally led to developing a specific strategy addressing the need to determine this set based on the user's anthropometric measurements. This strategy relies on solving a constrained optimization problem using the Nelder-Mead algorithm for solving nonlinear, nonconvex problems.

In this section, the optimization strategy will be reported briefly to motivate the origin of the geometric features taken as a reference for the design of the new kinaesthetic prototype.

The kinematic optimization algorithm originates with hand motion analysis to track the natural movement of the user's fingers performing a spherical grasping. This analysis was conducted at the Don Carlo Gnocchi Foundation Rehabilitation Center, Florence, Italy. Thirteen right-handed volunteer subjects (ten men and three women) with a mean age of 30 years were asked to grasp and release three times a cylindrical object with 50 mm in diameter, and appropriate markers applied.

The subjects seated in front of a table and the cylindrical objects were located by the subjects themselves in a comfortable position but within a set area, as reported in Figure 2.6, to optically track the whole gesture. The starting position (hand pose and body posture) was the same for all the participants. The hand was initially placed opened with the palm on the object with the the four long fingers completely extended and the thumb adducted. The shoulder was positioned with 0deg in abduction on the frontal plane and flexed with an angle of about 45deg in the sagittal plane (according to a comfortable posture for the subject). The elbow was slightly flexed in the sagittal plane in order to allow the subjects to keep the forearm on the table while they were grasping the cylindrical object. The wrist was in a neutral position (45degfor flexion and 0deg for radio-ulnar deviation).

The primary markers were placed on the MetaCarpoPhalangeal (MCP) joint, the Proximal InterPhalangeal (PIP) joint, the Distal InterPhalangeal (DIP) joint, and the Toe InterPhalangeal (TIP), as display in Figure 2.5. The marker on the MCP joint forms the system reference for each finger.

The BTS SMART-DX Suite MoCap system from BTS Bioengineering equipped with four infrared cameras (their configuration is shown in Figure 2.6) provided the marker tracking. This machine can automatically record three-dimensional

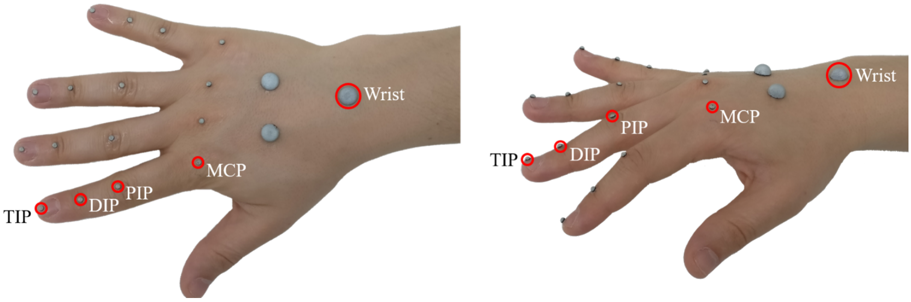
Wrist
MCP
PIP
DIP
TIP
Wrist
MCP
PIP
DIP
TIP

Figure 2.5: Marker position protocol.

trajectories by stereographic methods of passive, reactive markers with an acquisition frequency of 100 Hz. The BTS Smart Analyzer software package was used to reconstruct the marker positions.

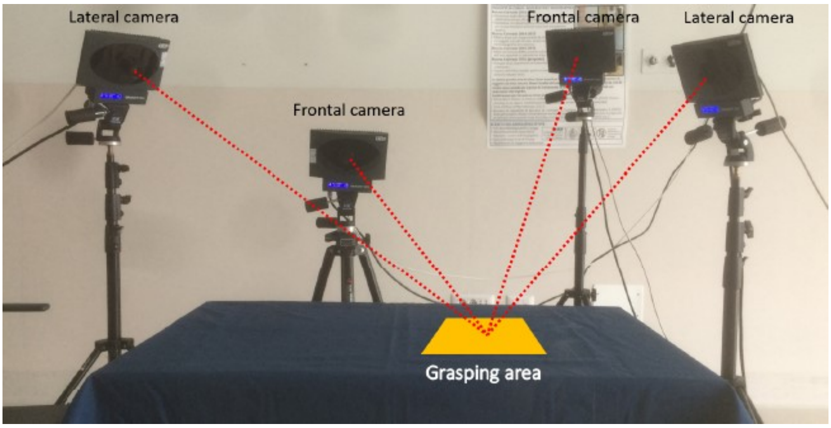
Lateral camera
Frontal camera
Frontal camera
Lateral camera
Grasping area

Figure 2.6: motion analysis camera setup.

Post-processing studies of the collected data provided the ability to associate as a function of anthropometric quantities, such as the distance between the MCP, DIP, and DIP joints, the trajectory of the midpoint of the distal phalanx on which the exoskeleton will be optimized.

Defining ρ^* as the value of the modulus of the radius vector of the reference trajectory acquired by post-processing of motion capture analysis and sampled with $k+1$ steps of the angle describing it in polar coordinates (β). The k-th polar error between the reference trajectory of the finger, i.e., the one reconstructed by means of the mocap system, and the actual one of the exoskeleton (ρ), shown in Figure 2.7, can be defined as follows:

$$e_k(\beta_k, S) = |\rho(\beta_k, S) - \rho^*(\beta_k, S)| \tag{2.14}$$

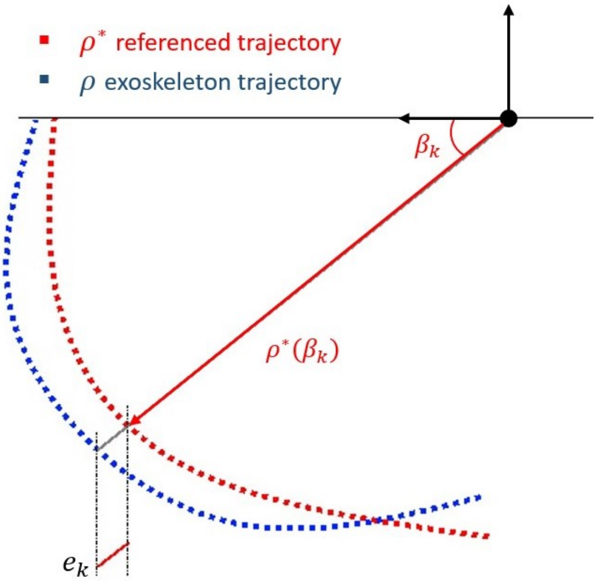

Figure 2.7: Graphical representation of the error between computed and reference trajectories.

The ρ trajectory is the result of the kinematic system, described by the equation 2.12, no longer dependent only on the variable q_3, but also on the geometric parameters contained in the vector $\{S\}$. By solving such a system as a constrained optimization problem, using Equation 2.15 as objective function, it is possible to search among the infinite solutions for the one that minimizes the polar error with the reference trajectory, respecting the imposed constraints.

$$\min_{\mathbf{S}} f(\mathbf{S}) = \min_{\mathbf{S}} \left(\max_{k} |e_k(S)| + \gamma \sum_{k=0}^{K} \frac{|e_k(S)|}{K+1} \right) \tag{2.15}$$

The mean error can be weighted within the objective function concerning the maximum error by the γ scaling coefficient. In this study, it was set to 1, weighting the maximum and average error equally. Constraints were added to the free variables of the problem, which aim to keep the final size of the device limited, discarding solutions that lead to nonfunctional or even impossible (from a physical point of view) exoskeletons.

Exploiting this numerical algorithm led to a new automatic procedure for mechanism optimization. The main advantages of which can be summarized as follows:

- the input data are some anthropometric measurement of the user hand.
- the data obtained automatically leads to a ready-to-use device using parametric Computer Aid Design (CAD) and Computer Aid Engineering (CAE) software for the manufacturing process.
- the resulting exoskeleton is customized to the user's hand.

The reliability of this optimization procedure was evaluated in 2019 through a special experimental campaign involving the resulting optimized exoskeletons by testing the accuracy with which they can reproduce physiological finger gestures. Using the BTS SMART-DX Suite MoCap system from BTS Bioengineering, the end-effector trajectories of the optimized exoskeletons were measured. After comparing them with the target ones, a maximum error committed during the range of motion between 0.9 and 8.80 mm was calculated (the mean value among all subjects was 3.16 mm, and the standard deviation was 1.47 mm); more than satisfactory results for rigid kinematic chain exoskeletons that ensure usability in close contact with human hands.

Chapter 3

Hand Exoskeleton design

The HES prototype presented, as already introduced in Subsection 1.3, employs a Bowden-cable-based RAS, resulting as the most suitable configuration for achieving the design goals targeted following a meticulous study of the-state-of-the-art of the current kinaesthetic HES applied to robot-augmented therapy. This type of layout allows all the heavy components required for the actuation and control of the device to be placed on the ground and keep the complexity of the mechanical architecture of the wearable part minimal.

In this Chapter, the wearable part, comprising the exoskeleton mechanism, will be presented and deeply discussed. In Section 3.1 the proposed mechanical solution will be addressed, introducing the characteristic modular design. Each technical solution will be analyzed and justified. Section 3.2 discloses the investigation performed over three volunteer subjects to identify a real-based direction of the HMI interaction force during a grasping gesture. This Chapter continues with the extensive dissertation of the mathematical background in Sections 3.3 and 3.4; in the former, the kinematic model introduced in the Chapter 2 will be adapted to new mechanism, and in the latter, a dynamic model will be introduced and discussed. By means of the dynamic model and the HMI force direction a custom algorithm to evaluate the HMI force module has been developed and will be described in Section 3.6. Finally, Section 3.5 shows the simulations for the structural verification conducted in Solidworks simulation environment.

3.1 Modular design

From a mechanical point of view, the design efforts were focused on developing a device equipped with the necessary sensors for a proper force and position control, exerting up to 15 N per finger both in opening and closing. Furthermore, to get as close as possible to a version that meets the usual requirements of a real rehabilitation scenario, the HES was designed to be safe, reliable, and capable of effectively rehabilitating patients with different anthropometric measurements and needs.

The proposed solution for the wearable exoskeleton part, shown in Figure 3.1, embodies a novel modular design that resulted in a joint patent [63] between University of Florence and MOV'IT srl. Three main types of modules can be distinguished: the Base Platform (BP), the Finger Module (FM), and the Interface Module (IM).

The BP is meant to work in tight contact with the user and be dressed using a special glove.

The FM, based on the MDM lab mechanism (Section 2.1), guides the flexion and extension movement of the corresponding finger by interacting on the intermediate phalanx.

The IM houses the end of Bowden cables and an ad-hoc designed and patented capstan to transmit motion from the motors housed in the RAS to the FM.

These three modules incorporate magnetic couplings that enable quick and easy assembly and disassembly, providing the connections between each FM and the BP and between each FM and the corresponding IM. Hereafter, they will be referred to as FM-BP and FM-IM couplings. The hand exoskeleton can thus be modified easily and quickly without needing tools.

The modular design strategy combined with the quick couplings was adopted to address the problem of frequent user change with different anthropometric measurements and unknown needs.

The FM, mounting the MDM mechanism combined with the kinematic optimization process (Chapter 2) is a guarantee of safety and reliability in working closely with human fingers, following numerous experimental campaigns and hours of validation. On the other hand, being a rigid kinematics parameterized on anthropometric measurements of a specific user, such a mechanism inevitably has a peculiar, not generalizable size. This feature is significantly at odds with the demand for HES to be adaptive to several patients with distinct, unknown a priori hand morphologies. Thus, assuming that an adequate number of FMs optimized on different sizes are available, taking advantage of the modularity of

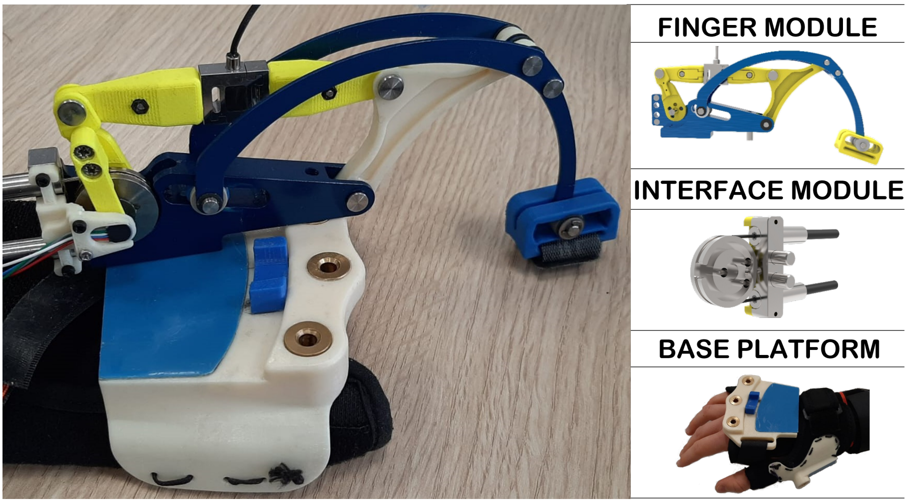

Figure 3.1: The proposed solution based on modular design.

the system easily assembled without the use of any tools, it is possible to decide on the number of fingers to be rehabilitated and, more importantly, to choose the appropriate FMs according to the specific size of the user. In this way, the device makes up for the poor adaptability of the rigid kinematic system with an easy and quick set-up according to the individual user's measurements and needs.

The prototype was designed to implement four fingers controlled independently, considering driving the ring and little finger simultaneously, a choice due to lateral space constraints. The actual test-case implementation can mount up to three FMs, three IMs, and two BPs by providing for the actuation of only three fingers: thumb, index, and middle ones, representing the minimum set of fingers to perform both power and precision grasps. The total weight of this set-up is around 400 g, resulting in an average weight acceptable to sustain during functioning.

3.1.1 The Base Platform

As visible in Figure 3.2, two types of BP modules have been designed, one for the thumb and one for the long fingers; the latter can mount up to three FMs.

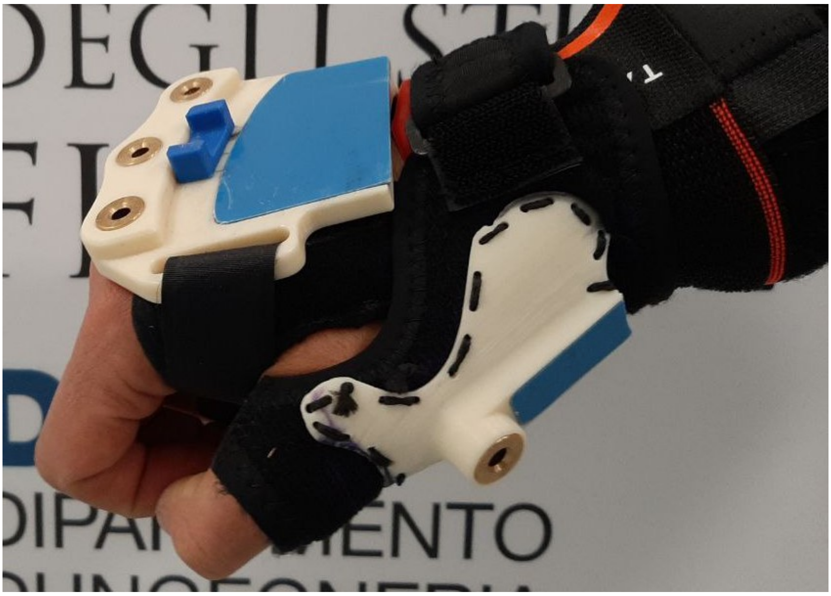

Figure 3.2: The BP module for the thumb is on the left, the BP for the long finger is on the right.

In general, both of BP types are composed of a support structure made of Acrylonitrile Butadiene Styrene (ABS) and sewn onto a special glove; this element, which interfaces with the user, is therefore responsible for the ergonomics and absorption of the reaction forces of the exoskeleton. It is made of 3D-printed hard plastic, limiting the device's weight on the distal limb with a complex lower-surface geometry to match the anatomy of the back of the hand as much as possible.

This module is also equipped with ferromagnetic metal sheet and flanged bushings to realize the BP-FM quick coupling, as depicted in Figure 3.3. The bottom surface of the FM is equipped with magnetic disks to maintain contact with the sheet metal and a pin to be inserted into the hole of a flanged bushing. This configuration creates a simple passive hinge for the ab/adduction gesture by reducing the constriction of the planar motion of the fingers, allowing the mechanism to self-align with the biological joints, preventing the exoskeleton from being uncomfortable or even causing injury or pain to the user during operation. A specific low-friction technical polymer tape is applied to the metal sheet, facilitating the passive ab/adduction movement to preserve the feeling of mobility as much as possible.

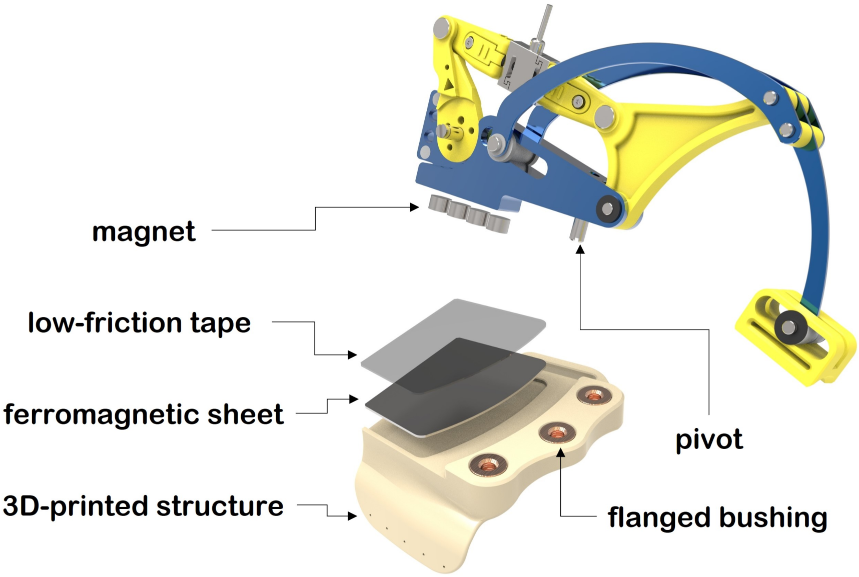

Figure 3.3: Main components for FM-BP coupling.

3.1.2 The Interface Module

The IM is responsible for connecting the FM to the actuation system. This module (visible in Figure 3.4) is composed of a custom capstan, specially designed to transmit the rotation by pulling the inner Bowden cables, and a block system to absorb the push of the sheaths. Both are equipped with pins and magnets that, combined with the respective holes and magnets located in the FM, realize the FM-IM coupling. This coupling allows the exoskeleton to be switched from an unactuated to an actuated configuration and vice versa, allowing for a fast user-size-based setup. During the actuated configuration, the sheath-block system is integral to the frame of the exoskeleton, while the capstan rotates together with the FM mechanism.

The block system stops the sheaths with a shape coupling using a groove machined on the sheath-ends, made of steel, by screwing the magnetic-encoder bracket, on which the housing of RM08 (RENISHAW Co.) is also derived. This type of sensor counts the number of ticks based on the changes in the magnetic field induced by the relative rotation between the sensor and a magnet placed on the capstan 0.5 mm away.

The capstan is actuated by passing a single cable through a particular path trilled on the capstan itself, which is serrated by a headless screw. In turn, when IM-FM coupling is performed, the capstan transmits torque to the FM kinematics through three steel pins while also ensuring relative centering. In addition, the three pins are positioned in such a way as to realize a clear coupling direction to avoid any assembly errors of the IM-FM coupling.

For the sake of resistance and precision reasons required, the capstan and the block system were made of AISI 316 steel, taking advantage of its stainless and non-magnetic properties, which are very advantageous in this context.

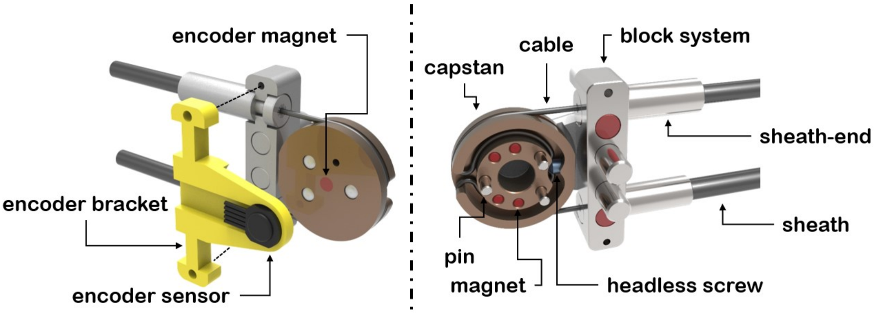

Figure 3.4: An overview of the IM.

3.1.3 The Finger Module

The FM is the result of the development process undertaken by the MDM lab since 2014, embodying the know-how in rigid exoskeleton design introduced in Chapter 2. Referring to Figure 3.5, which shows the kinematics of the FM, it is possible to identify the links: AC, BC, and CE, characteristic of typical MDM kinematics and result of the kinematic optimization algorithm on anthropometric parameters. In contrast to the classical architecture presented in Section 2.1, the FM kinematics have three additional links: ZN, NH, and HA, which form a four-bar linkage. The rear crank (ZN) is connected through the dedicated quick coupling (FM-IM coupling) to the IM capstan, which uses three pins to transfer the rotation. In turn, the front crank (HA), made integral with the AC link, drives the exoskeleton kinematic mechanism for finger actuation. In this context, the HA and AC links were merged into a single 3D-printed component.

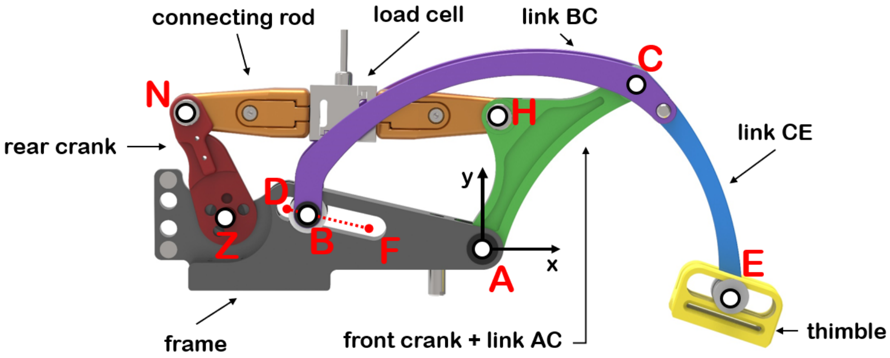

Figure 3.5: FM kinematic chain.

As shown in Figure 3.6, the kinematic chain of the four-bar linkage was designed to ensure mechanical end stops, realized by the block system in opening and the frame in closing. Limiting the rotation of the rear crank (ZN) such that point E, referring to the global reference system centered at A, has a range of motion starting from an ordinate of -17 mm, at the maximum opening and reaching a zero abscissa at ultimate closing. The ordinate of -17 mm ensures the straight extension of the finger once the exoskeleton is worn. The mechanical end stops introduction provides intrinsic safety, avoiding unpleasant consequences due to any failure in the device control: once the end stops are reached, the motor's energy is unloaded no longer to the user's limb but to the exoskeleton mechanism itself.

The addition of the four-bar-linkage-based transmission implied an increase in the number of components, a consequent rise in manufacturing and management costs, and a significant increase in kinematic complexity by introducing a variable torque transmission ratio between the front crank and AC link as a function of the finger pose. However, the chosen layout still results in the most convenient overall configuration by allowing the IM housing to be placed at the rear of the module, maintaining a contained lateral encumbrance, and

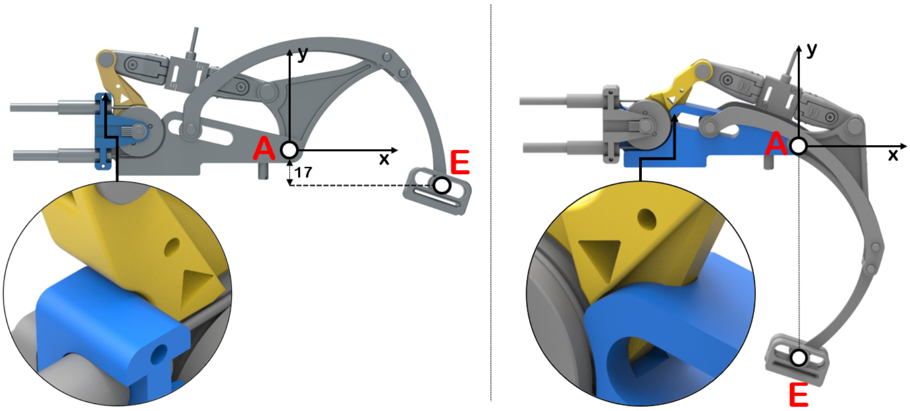

Figure 3.6: To the left is shown the maximum opening configuration,and to the right the maximum closing configuration.

sufficiently restraining the complexity of the geometry of the remaining components. In addition, the connecting rod turns out to be the ideal component for inserting the load cell into the kinematic chain, being a component subject only to axial tension during operation. The load cell model mounted on board is FSSM-500N from Forsentek co. Thanks to its S-shape, it allows external axial loads to be transformed into flexural stress to measure up to 500N of axial force in just 20x20x6 mm. The components that connect to the load cell to form the connecting rod of the four-bar linkage were designed so that the connecting rod results in a straight shape to transmit a purely axial stress state to the cell allowing for the cleanest possible reading. Because of the complicated form required to achieve this goal, these components were 3D printed.

To ensure precise and reliable operation of the mechanism, key components, such as the frame, sliders, pivots, and BC and CE links, were fabricated by classical manufacturing techniques that allow the achievement of very tight dimensional and geometric tolerances with excellent surface finishes, avoiding backlash or jamming events. In particular, the frame, the component with the most complex geometry, was made through a milling process that required a 5-axis numerically controlled machine. The links, with definitely simpler geometry, result from a laser cutting process on 2 mm sheets and subsequent boring in the holes where a specific tolerance is required. The components in question were made of 2014-T6 aluminum alloy and anodized in electric blue color.

The slider was made in Polyether Ether Ketone (PEEK) by a two-axis milling machine and commercial low-friction technopolymer bushings (Igus Co.) were inserted into the revolute joints to minimize friction for the relative rubbing motion. Figure 3.7 reports an exploded view of the FM for a better and clearer reader understanding.

An essential addition to the prototypes previously developed by MDM lab is the custom thimble with which the exoskeleton interacts on the medial phalanx. Through a pivot-slider coupling, this thimble adds a passive DoF to the system that absorbs a certain amount of the error committed between the trajectory imposed by the rigid kinematics and the natural trajectory, making the exoskeleton almost transparent to the user's fingers in performing their natural trajectory. The amount of absorbable error depends on the stroke of the slider, and its inclusion in the drive chain allows the device's usability with a wider range of anthropometric dimensions, allowing a limited number of sizes to cover a sufficiently large spectrum of patients.

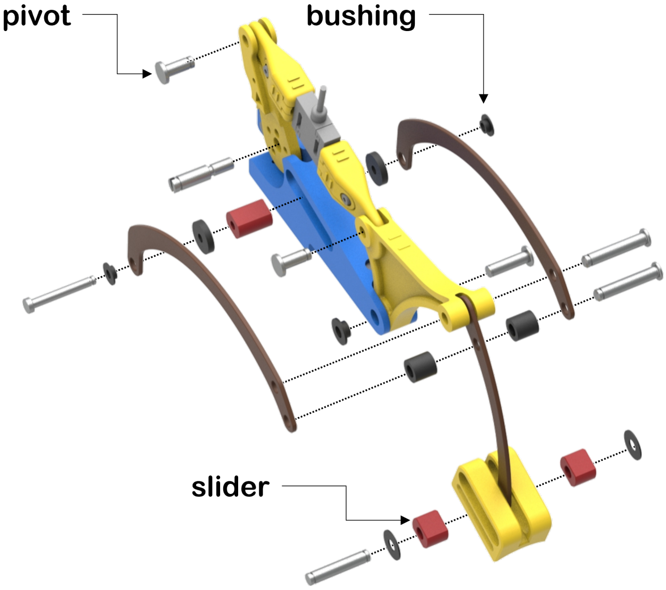

Figure 3.7: The exploded view of the FM.

For the realization of the prototype test-bench, three finger modules were made taking as reference the measured anthropometric dimensions of a thumb, an index finger and a middle finger, concerning to Figure 2.5 and shown in Table 3.1.

anthropometric measure	**index**	**middle**	**thumb**
MCP-PIP distance	43	48	32
PIP-DIP distance	25	30	27
mean finger diameter	19	19	20

Table 3.1: The anthropometric reference measures in mm for the test bench prototype.

Using the kinematic optimization algorithm, introduced in Section 2.2, the positions of the joints of interest, referred to a global reference system located at point A, according to Figure 3.5, were derived and reported in Table 3.2.

	index		**middle**		**thumb**	
point	**x**	**y**	**x**	**y**	**x**	**y**
A	0	0	0	0	0	0
C	33	47	37	47	50	33
E	60	-6	67	-7	53	-10
F	-32	6	-35	7	-23	12
D	-49	10	-54	11	-34	19

Table 3.2: The optimized geometric dimensions of the FMs for the test bench prototype referred to the global reference system in A and reported in mm.

3.2 Detection of HMI force orientation

As pointed out in the previous subsection, thanks to the special thimble, a passive degree of freedom is added to the system through a pivot-slider coupling. With this solution, the component of the force tangential to the phalanx exerted by the exoskeleton at point E, which would stress the human finger joints in an undesirable way, causes the slider to slide. As a result, due to the introduced thimble, interaction occurs only along the perpendicular direction to the phalanx; that is, the ideal one. While this has enormous advantages in terms of comfort and safety, it also makes it impossible to know the direction and intensity of the force the device exerts on the user from the kinematics of the device alone. The orientation of the phalanx is a characteristic that depends on the anatomical parameters of the specific user. Under this analysis, measuring the interaction force orientation when the hand is coupled to the exoskeleton is mandatory to effectively quantify the exoskeleton-user interaction force as a function of the mechanism pose. Therefore, three healthy candidates were involved in a preliminary study upon signing an informed consent form and asked to wear the FM index finger and perform at least five times index finger flexion. The direction of the interaction force was then reconstructed by sampling the trajectory with a 5° interval on crank Range of Motion (RoM), both by direct measurement with a digital goniometer and by using the open-source software Kinovea to compare the results obtained, as shown in Figure 3.8.

The measurement process via goniometer requires stopping the motor at each sampling step so that the operator can take the goniometer measurement and monitor the crank angle through the encoder. This evaluation allows using an accurate instrument; however, human error can potentially affect the process.

On the other hand, the measurement based on Kinovea image processing software involves an initial stage of preparation of the scene and subject to be imaged. The camera must be positioned so that the optical axis coincides with the vertical-gravitational direction while the scene runs parallel to the focal plane. A line of known length is placed on the scene for calibration of the Kinovea post-processing system. This test campaign is less prone to human error, but the measurements obtained by post-processing are certainly less accurate than the direct measurement made by the digital goniometer.

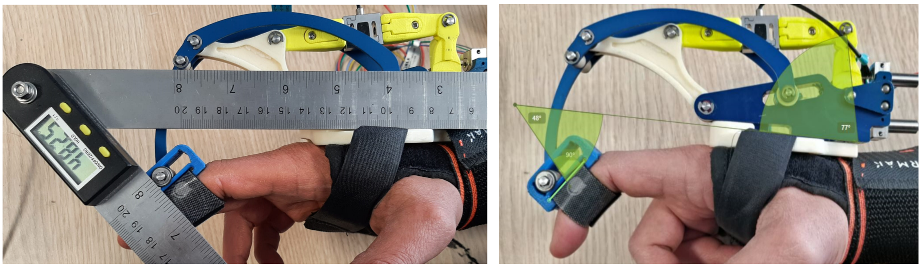

Figure 3.8: Procedure to measure the orientation of the interaction force by digital goniometer on the left, and by exploiting the software Kinovea on the right.

Data collection was carried out with respect to the global reference system positioned in A, measuring the directions concerning the x-axis. Accordingly, the crank angle during the RoM ranges from 110° to 45°, which corresponds to the maximum opening and closing of the mechanism, respectively.

Figure 3.9 compares the directions of the interaction forces obtained with the two procedures. The digital goniometer and Kinovea show a tendency for the HMI interaction force to align with the horizontal direction, approaching 0°, during the closing gesture. The wide variability recorded among the observed subjects shows a significant anthropometric measurement dependence. Finally, it is worth noting that the two sampling methods yielded similar results, differing by up to 5°.

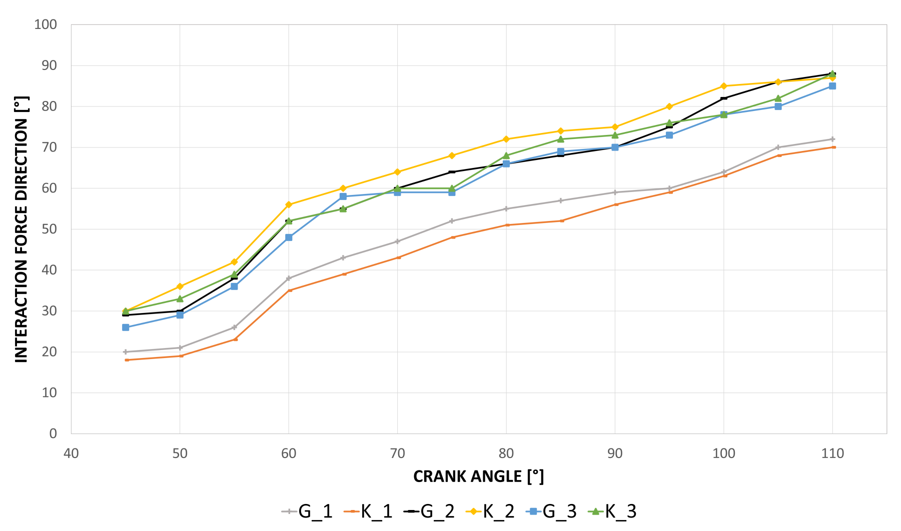

Figure 3.9: Directions of the interaction force as a function of the crank angle. The G_i plot shows the measurements of the i-th subject performed with the digital goniometer, while the K_i plot shows the measures of i-th subject extrapolated with Kinovea software. The reported angle values are expressed in deg.

3.3 FM kinematic model

As anticipated in Subsection 3.1.3, the four-bar linkage's implementation greatly complicated the system's kinematics. The significant consequences result in the change of the controlled joint from A to Z and a torque-transmission ratio from the rear crank to the AC link that is not constant but a function of the mechanism pose. During the design, these modifications have forced the expansion of the kinematic model introduced in Section 2.1, adding the new components comprising the four-bar linkage.

The system describing the kinematics of the new FM mechanism can be derived by the same methodology exposed and described in Section 2.1, adding the ZN, NH, and HA links to the discussion. A local reference system is added for each link, with the Gi-th origin positioned at half of its length described by the li-th parameter; as shown in the Figure 3.10.

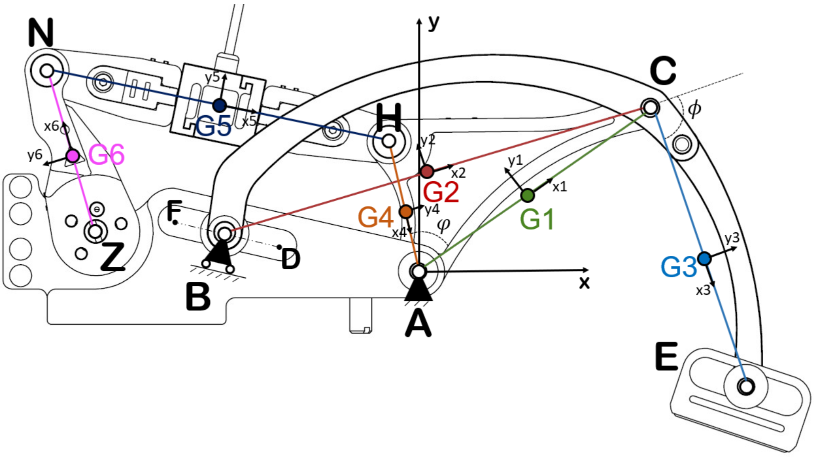

Figure 3.10: Lateral view of the FM mechanism and the corresponding kinematic chain.

Reminding that the vector of state variables $\{q\}$ has the q_{3i-2} component equal to Gi_x, the q_{3i-1} to Gi_y, and the q_{3i} equal to the counterclockwise angle θ_i describing the orientation of the x-axis of the i-th frame with respect to the reference one positioned in A, the state vector of the system increases from 9 to 18 components, as does the total number of DoFs.

The external constraints connecting these new generalized coordinates are a fixed hinge in Z (Equation 3.1), an internal hinge in N (Equation 3.2), an internal hinge in H (Equation 3.3), an internal hinge in A (Equation 3.4), and a constant angle between the HA link and the AC link (Equation 3.5). They give rise to a total of 9 scalar constraint equations.

$$R_6^0\ {}^6\{Z\} = \begin{bmatrix} {}^0Z_x \\ {}^0Z_y \end{bmatrix} \tag{3.1}$$

$$R_6^0\ {}^6\{N\} = R_5^0\ {}^5\{N\} \tag{3.2}$$

$$R_5^0\ {}^5\{H\} = R_4^0\ {}^4\{H\} \tag{3.3}$$

$$R_4^0\ {}^4\{A\} = R_1^0\ {}^1\{A\} \tag{3.4}$$

$$\varphi = cost \tag{3.5}$$

By rewriting Equations 3.1, 3.2, 3.3, 3.4, and 3.5 as a function of the state variables contained in the vector $\{q\}$, the new constrain system can be obtained as follows:

$$\begin{cases} q_1 - l_1 \cos q_3 = 0 \\ q_2 - l_1 \sin q_3 = 0 \\ q_1 + l_1 \cos q_3 - q_4 - l_2 \cos q_6 = 0 \\ q_2 + l_1 \sin q_3 - q_5 - l_2 \sin q_6 = 0 \\ d\,(q_5 - l_2 \sin q_6) + f\,(q_4 - l_2 \cos q_6) + h = 0 \\ q_4 + l_2 \cos q_6 - q_7 + l_3 \cos q_9 = 0 \\ q_5 + l_2 \sin q_6 - q_8 + l_3 \sin q_9 = 0 \\ q_9 - q_6 - \phi = 0 \\ q_{10} + l_4 \cos q_{12} = 0 \\ q_{11} + l_4 \sin q_{12} = 0 \\ q_{10} - l_4 \cos q_{12} - q_{13} - l_5 \cos q_{15} = 0 \\ q_{11} - l_4 \sin_{12} - q_{14} - l_5 \sin q_{15} = 0 \\ q_{13} - l_5 \cos q_{15} - q_{16} - l_6 \cos q_{18} = 0 \\ q_{14} - l_5 \sin q_{15} - q_{17} - l_6 \sin q_{18} = 0 \\ q_{16} - l_6 \cos q_{18} - Zx = 0 \\ q_{17} - l_6 \sin q_{18} - Zy = 0 \\ q_3 - q_{12} - \varphi = 0 \end{cases} \tag{3.6}$$

The constrain vector $\{\Psi\} \in \mathbf{R}^{17}$ of the system can be obtained by applying the definition expressed by Equation 2.10 to the constrain system reported in Equation 3.6.

All the observations for the kinematic system described in Section 2.1 can be similarly made for the new extended kinematic system. In particular, since globally, the system maintains a single DoF, it is possible to manipulate the nine equations so that the 18 variables result as a function of one. In this context, as the Z-joint is sensorized via the magnetic encoder, it was decided to use the variable q_{18} as the control variable. By explicitly rewriting of the constrain equation can be derived the system that describes the kinematic behavior of the system and it is reported in Equation 3.7. It is worth noting that, known q_{18} thanks to the measurements provided by the encoder, the solution of this system of equations yields instant-by-instant knowledge of the state vector of the system and, consequently, all points of the exoskeleton mechanism.

$$\begin{cases} q_{12} = 2\arctan\left(\frac{-g+\sqrt{g^2-4em}}{2e}\right) \\ q_{16} = Z_x + l_6\cos q_{18} \\ q_{17} = Z_y + l_6\sin q_{18} \\ q_{15} = \arctan\left(\frac{l_6\sin q_{18}+l_4\sin q_{12}+Z_y/2}{l_6\cos q_{18}+l_4\cos q_{12}+Z_x/2}\right) \\ q_{13} = -l_5\cos q_{15} - 2l_4\cos q_{12} \\ q_{14} = -l_5\sin q_{15} - 2l_4\sin q_{12} \\ q_{10} = -l_4\cos q_{12} \\ q_{11} = -l_4\sin q_{12} \\ q_3 = q_{12} - \varphi; \\ q_6 = 2\arctan\left(\frac{-b+\sqrt{b^2-4ac}}{2a}\right) \\ q_4 = 2l_1\cos q_3 - l_2\cos q_6 \\ q_5 = 2l_1\sin q_3 - l_2\sin q_6 \\ q_9 = \phi + q_6 \\ q_7 = q_4 + 2l_2\cos q_6 + l_3\cos q_9 \\ q_8 = q_4 + 2l_2\sin q_6 + l_3\sin q_9 \end{cases} \tag{3.7}$$

Where $e = l_4^2 - l_5^2 + \left(l_6\cos q_{18} + \frac{Z_x}{2}\right)^2 + \left(l_6\sin q_{18} + \frac{Z_y}{2}\right)^2 - 2l_4\left(l_6\cos q_{18} + \frac{Z_y}{2}\right)$, $m = l_4^2 - l_5^2 + \left(l_6\cos q_{18} + \frac{Z_x}{2}\right)^2 + \left(l_6\sin q_{18} + \frac{Z_y}{2}\right)^2 + 2l_4\left(l_6\cos q_{18} + \frac{Z_y}{2}\right)$, and $g = 4l_4\left(l_6\cos q_{18} + \frac{Z_y}{2}\right)$.

3.4 FM dynamic Model

Since the prototype under consideration was developed to render the force of human-virtual reality interaction and to be controlled accordingly, an analysis of the dynamic system was necessary to write the force exerted at the end-effector as a function of the one measured by the load cell. In addition, dynamic modeling of the mechanism is a fundamental computational tool for the design and fine-tuning of the device, as it allows the sizing of custom components, the selection of commercial ones, and the calibration of the load cells.

The dynamic model was constructed by the Lagrange-multipliers method applied to the dynamic Lagrange equation written for multibody systems subjected to kinematic constraints [64]. The success of this method in computational dynamics lies in it provides a precise procedure for writing the dynamic model regardless of kinematic complexity; moreover, it can be easily implemented on computational software and solved numerically.

The general form of the Lagrange equation comprising Lagrange multipliers for a constrained-multibody system is described in Equation 3.8.

$$[M]\{\ddot{q}\} + \left[\frac{\partial \Psi}{\partial \mathrm{q}}\right]^{\top} \{\lambda\} = \{\widetilde{F}\} - [C]\{\dot{q}\} - \left\{\frac{\partial V}{\partial q}\right\}^{\top} \tag{3.8}$$

where $[M]\{\ddot{q}\} \in \mathbf{R}^{n\times n}$ is the term indicating the inertial forces; $[\frac{\partial \Psi}{\partial \mathrm{q}}] \in \mathbb{R}^{nc\times n}$ is the Jacobian matrix of the constraint vector $\{\Psi\}$; $\{\lambda\} \in \mathbb{R}^{nc}$ is the vector that collect the Lagrangian multipliers; $\{\widetilde{F}\} \in \mathbb{R}^{n}$ is the generalized force vector; $[C]\{\dot{q}\}$ collects viscous and damping terms; V is the potential energy function of the system; $\{q\} \in \mathbb{R}^{n}$ is the generalized coordinate vector; n and nc are, respectively, the number of total DoFs and constraint equations of the system. Due to the low magnitude of the weights and velocities involved, the contributions of potential energy $\{\frac{\partial V}{\partial q}\}$, inertial forces $[M]\{\ddot{q}\}$, and the damping forces $[C]\{\dot{q}\}$ have been neglected as they are remarkably smaller than the external forces. Therefore, only the vector of generalized forces $\{\widetilde{F}\}$ has been evaluated:

$$\tilde{F} = \begin{bmatrix} \tilde{F}_1 & \dots & \tilde{F}_n \end{bmatrix}^{\top} = \begin{bmatrix} \frac{\partial w}{\partial q_1} & \cdots & \frac{\partial w}{\partial q_n} \end{bmatrix}^{\top} \tag{3.9}$$

where ∂w represents the virtual work that can be calculated as:

$$\partial w = \sum_{i=0}^{n} \Big(\begin{bmatrix} \partial x_{Pi} & \partial y_{Pi} \end{bmatrix} \begin{bmatrix} Fx_{Pi} & Fy_{Pi} \end{bmatrix}^{\top} + \partial \vartheta_{Pi} T_{Pi} \Big) \tag{3.10}$$

where Pi is the application point of the i-th external force; ∂x_{Pi} and ∂y_{Pi} represent the virtual displacements of Pi relative to the global reference system; Fx_{Pi} and Fy_{Pi} are the components of the external force vector applied on Pi

relative to the global reference system; T_{Pi} represents the torque applied on Pi; $\partial\vartheta_{Pi}$ is the virtual angular displacement relative to torque.

In the presented case, the system of external forces includes the torque exerted by the exoskeleton capstan on the rear crank about joint Z (indicated henceforth with T_Z), and the force at joint E (with components Fx_E and Fy_E) resulting from the interaction of the user's finger with the thimble. The generalized force vector can then be derived by applying Equation 3.10 to the external forces system under consideration and substituting it into Equation 3.9, thus obtaining a vector of 18 components, mostly null elements except for four of them:

$$\begin{cases} \tilde{F}_7 = Fx_E \\ \tilde{F}_8 = Fy_E \\ \tilde{F}_9 = Fy_E l_3 \cos q_9 - Fx_E l_3 \sin q_9 \\ \tilde{F}_{18} = T_Z \end{cases} \tag{3.11}$$

For the purposes of this work, the external forces Fx_E and Fy_E are considered known, so in Equation 3.8, the unknown variables are the 17 Lagrange multipliers contained in $\{\lambda\}$ and the torque T_Z. Indeed, the components of the constraint vector $\{\psi\}$, which depend only on the generalized coordinates collected in $\{q\}$, are known by the resolution of the kinematics and the angle encoder measurement (q_{18}). Manipulating Equation 3.8, a 18-dimension linear system is obtained as follows:

$$\left[\left[\frac{\partial \Psi}{\partial \mathrm{q}}\right]^{\top} | \left\{ \begin{array}{c} 0 \\ \vdots \\ -1 \end{array} \right\} \right] \left\{ \begin{array}{c} \lambda \\ T_Z \end{array} \right\} = \{Q\} \tag{3.12}$$

where $Q \in \mathbb{R}^{18}$ is derived from the generalized force vector $\{\tilde{F}\}$ by imposing $\tilde{F}_{18} = 0$ once moved T_z to the left side of the equation.

Once calculated the λ variables from Equation 3.12, the reaction forces $\{\tilde{R}\}$ can be expressed as a function of the Lagrangian multipliers.

In general, the reaction force vector arising from the k-th and $k+1$-th constrain equations can be derived with respect to a v-th reference system centered on the point of application of the constraint, which will be referred to by example as P, as follows:

$$\left\{\begin{array}{c} {}^{v}\tilde{P}_x \\ {}^{v}\tilde{P}_y \\ \tilde{T}_P \end{array}\right\} = \left[\begin{array}{cc} -\left[R_v^i\right]^\top \left[R_i^0\right]^\top & \left\{\begin{array}{c} 0 \\ 0 \end{array}\right\} \\ {}^{i}\{P\}^\top [V]\left[R_i^0\right]^\top & -1 \end{array}\right] \left[\begin{array}{cc} \frac{\partial\Psi_k}{\partial q_{3i-2}} & \frac{\partial\Psi_{k+1}}{\partial q_{3i-2}} \\ \frac{\partial\Psi_k}{\partial q_{3i-1}} & \frac{\partial\Psi_{k+1}}{\partial q_{3i-1}} \\ \frac{\partial\Psi_k}{\partial q_{3i}} & \frac{\partial\Psi_{k+1}}{\partial q_{3i}} \end{array}\right] \left\{\begin{array}{c} \lambda_k \\ \lambda_{k+1} \end{array}\right\} \tag{3.13}$$

where R_v^i is the rotation matrix expressing the orientation of the v-th frame with respect to the i-th reference system, $[V]$ is the matrix $\left[\begin{array}{cc} 0 & 1 \\ -1 & 0 \end{array}\right]$, ${}^{v}\tilde{P}_x$ and ${}^{v}\tilde{P}_y$ are the reaction force components a directed along the x-axis and y-axis of the v-th reference system with P as application point, and $\tilde{T}_P$ is the constrain torque applied about the z-axis of the v-th frame.

Specifically, applying Equation 3.13 and referring to reference systems shown in Figure 3.11, the equations that describe the reaction force at the joint H (Equation 3.14), C (Equation 3.15), Z(Equation 3.16) A , and B (Equation 3.19) can be derived.

The reaction force at point A is given by the sum of the two contributions from the AC link (Equation 3.17) and the front crank HA (Equation 3.18).

The constraining forces derived from constraining Equations 2.7, 2.8, 3.4, and 3.5 describing the continuity of the HA link with the AC link and the FC link with CD link are actually internal forces, the resolution of which is of no particular interest.

$$\left\{\begin{array}{c} {}^{h}\tilde{H}_x \\ {}^{h}\tilde{H}_y \\ \tilde{T}_H \end{array}\right\} = \left\{\begin{array}{c} \lambda_{11}\cos q_{15} + \lambda_{12}\sin q_{15} \\ -\lambda_{11}\sin q_{15} + \lambda_{12}\cos q_{15} \\ 0 \end{array}\right\} \tag{3.14}$$

$$\left\{\begin{array}{c} {}^{c}\tilde{C}_x \\ {}^{c}\tilde{C}_y \\ \tilde{T}_c \end{array}\right\} = \left\{\begin{array}{c} -\lambda_3\cos q_3 - \lambda_4\sin q_3 \\ \lambda_3\sin q_3 - \lambda_4\cos q_3 \\ 0 \end{array}\right\} \tag{3.15}$$

$$\left\{\begin{array}{c} {}^{z}\tilde{Z}_x \\ {}^{z}\tilde{Z}_y \\ \tilde{T}_Z \end{array}\right\} = \left\{\begin{array}{c} -\lambda_{15}\cos q_{18} - \lambda_{16}\sin q_{18} \\ \lambda_{15}\sin q_{18} - \lambda_{16}\cos q_{18} \\ 0 \end{array}\right\} \tag{3.16}$$

$$\left\{\begin{array}{c} {}^{a1}\tilde{A}_x \\ {}^{a1}\tilde{A}_y \\ \tilde{T}_A \end{array}\right\} = \left\{\begin{array}{c} -\lambda_1\cos q_3 - \lambda_2\sin q_3 \\ \lambda_1\sin q_3 - \lambda_2\cos q_3 \\ 0 \end{array}\right\} \tag{3.17}$$

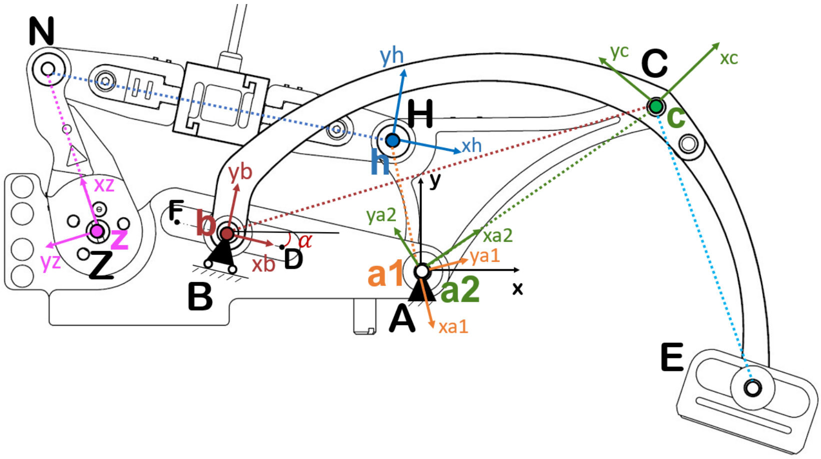

Figure 3.11: The local reference systems, h, c, a, z, and b, with respect to which the reaction forces applied to the H point, C point, A point, Z point, and B point were calculated.

$$\left\{\begin{array}{c} {}^{a2}\tilde{A}_x \\ {}^{a2}\tilde{A}_y \\ \tilde{T}_A \end{array}\right\} = \left\{\begin{array}{c} -\lambda_{10}\cos q_{12} - \lambda_{11}\sin q_{12} \\ \lambda_{10}\sin q_{12} - \lambda_{11}\cos q_{12} \\ 0 \end{array}\right\} \tag{3.18}$$

$$\left\{\begin{array}{c} {}^{b}\tilde{B}_x \\ {}^{b}\tilde{B}_y \\ \tilde{T}_B \end{array}\right\} = \left\{\begin{array}{c} 0 \\ f\lambda_5\sin(q_6+\alpha) - d\lambda_5\cos(q_6+\alpha) \\ 0 \end{array}\right\} \tag{3.19}$$

where α is the angle that describes the orientation of the sliding direction FD with respect to x-axis of the global reference system.

3.4.1 Forces analysis of the FM-IM coupling

This subsection is dedicated to defining and formalizing the forces that the FM exchanges with the IM, referring to the diagram illustrated in the Figure 3.12.

As already introduced in Subsection 3.1.2 devoted to the introduction of the IM, the rear crank transmits torque T_z to the capstan employing three pins placed in m_1, m_2, and m_3 holes. Through the combined action of the headless

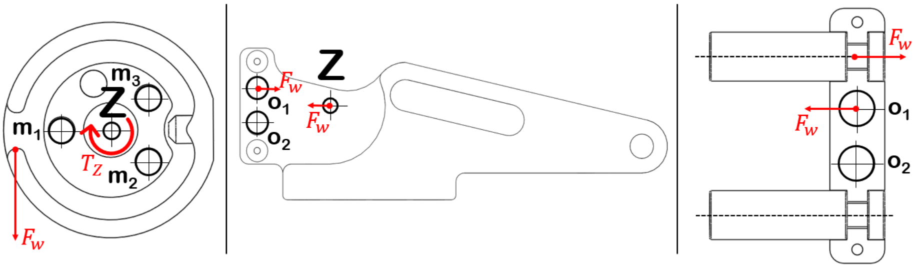
m3
Z
m1
T_Z
m2
F_w
Z
F_w
o1
F_w
o2
F_w
F_w
o1
o2

Figure 3.12: The scheme of forces due to the interaction between the IM and the FM.

screw and groove, the capstan pulls one branch of the cable while the other remains unloaded. The contact area of the cable with the capstan is shown in the Figure 3.13, and this area can be schematized as the point of application of the Bowden Cable tensile force F_w, which can be calculated by the balance of moments as follows:

$$F_w = 2\frac{T_Z}{d} \tag{3.20}$$

where $d = 22mm$ is the diameter of the IM capstan.

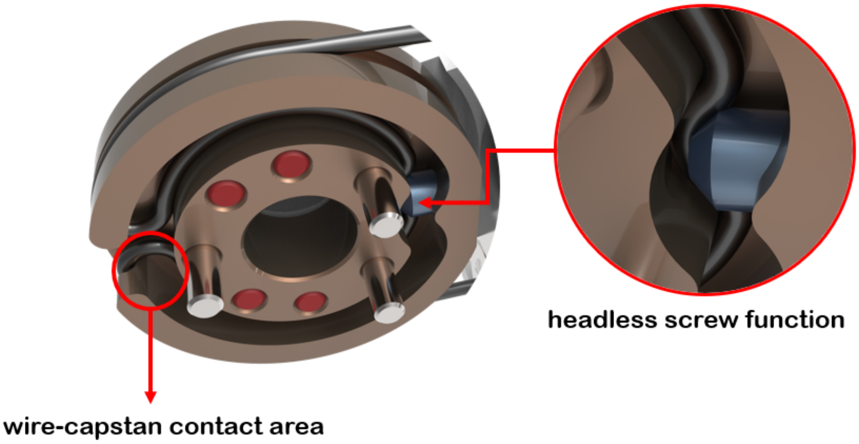
headless screw function
wire-capstan contact area

Figure 3.13: The wire-capstan contact during the functioning.

This force via the pivot in Z point, passing through the rear crank (Figure 3.12), loads the frame of the FM. Because of the friction at the cable-sheath interface, the Bowden cable system transmits a force to the sheath with an equal intensity and opposite direction to the inner cable's tension force. Then, the force F_w is transmitted in the opposite direction to the blocking system thorough the shape coupling of the terminals with the appropriate groove. The block system, in turn, via the pins in O points, transmits it back to the frame. Thus, the FM-IM interaction results in an area of the frame locally compressed by a Force equal to the tension exerted on the wires.

In light of this analysis, for the sake of completeness, the complete load system acting on the rear crank is shown in the Figure 3.14. Where to the forces already discussed in the previous section ($\tilde{N}$, $\tilde{Z}$ and T_Z) colored in blue are added the forces applied to the m-holes, colored in red. The latter ones counteract the relative translation between the rear crank and the IM capstan, which, in general, can be considered to have a modulus equal to one-third of the cable tensioning force.

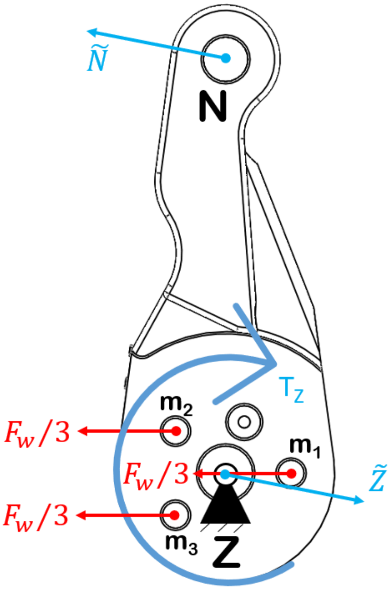

Figure 3.14: The complete rear crank set of loads.

3.5 Structural analysis

This section presents the structural analysis performed in the CAD-CAE environment to certify the system's suitability to withstand the forces required by the application under consideration. Specifically, simulations related to stress (3.5.1) and stiffness (3.5.2) analysis conducted using the finite element method are reported in this paper. However, although they will not be mentioned, multiple such studies have also been conducted during the design and sizing process helping in the choice of materials, manufacturing processes, and the adoption of specific technical solutions over others.

3.5.1 Stress analysis

For solving structural finite element analyses, for each system component, four different aspects must be considered and defined: geometry, material, constraint conditions, and loading system. The geometry was mainly driven by the kinematic optimizer, as reported in Table 3.2, and the need to keep the dimensions of the mechanism as small and compact as possible, taking into account the actual technological constraints, and mechanical strength issues.

The material of each component was selected according to the complexity of the geometry, the precision limits required for proper operation, and the structural properties required. Table 3.3 reports the selected materials for the components involved in the structural analysis, which belong to FM and IM modules along with the main mechanical properties such as yield stress and young module.

Component	**Material**	**Yield Stress**	**Young Module**
link BC	2014-T4	280	72
link CE	2014-T4	280	72
frame	peraluman 5754	130	72
rear crank	ABS	31	1.5
front crank	ABS	31	1.5
connecting rod	ABS	31	1.5
capstan	AISI 316	200	200
block system	AISI 316	200	200

Table 3.3: The selected materials for each component with the relative yield stress in MPa and Young Module in GPa.

In the stress analysis is mandatory evaluate the worst case for each component. Using the dynamic model, described in Section 3.4, it was possible calculate the loads acting on each single component and determine the worst load set. Specifically, for this work, Equation 3.12 was solved for each force profile displayed in Figure 3.9 with the modulus of the maximum operating force (15 N). By applying Equations 3.14, 3.17, 3.18, 3.19, 3.16, 3.15, and 3.20 the constraining forces that stress the components of interest during functioning were derived. Figures 3.15 and 3.16 show the highest magnitude of the constrained reactions in A, C, H, B, and the torque applied in Z, as the back crank angle (q_{18}) varies.

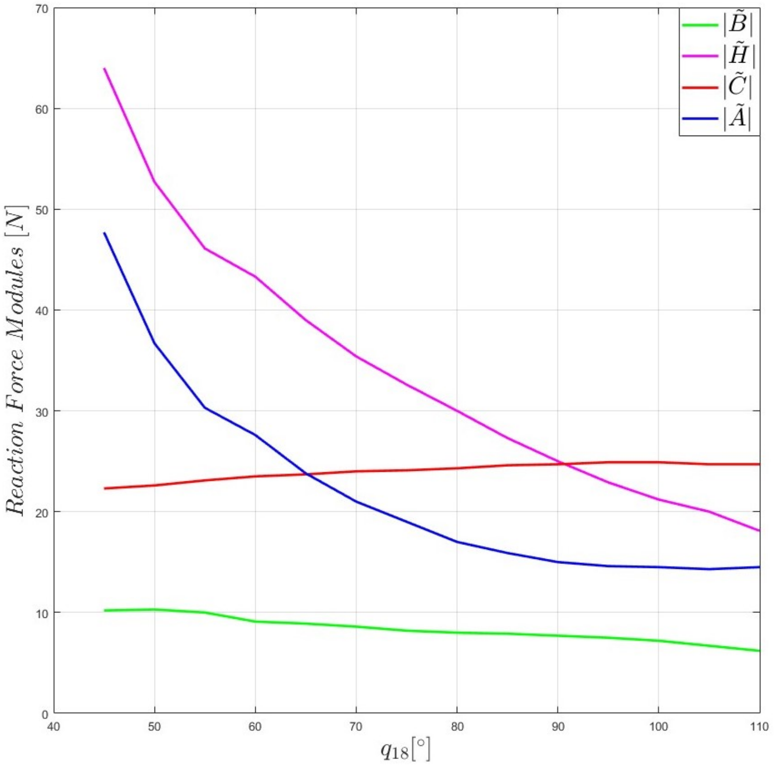

Figure 3.15: The force values of interest for structural analysis as the crank angle changes (q_{18}).

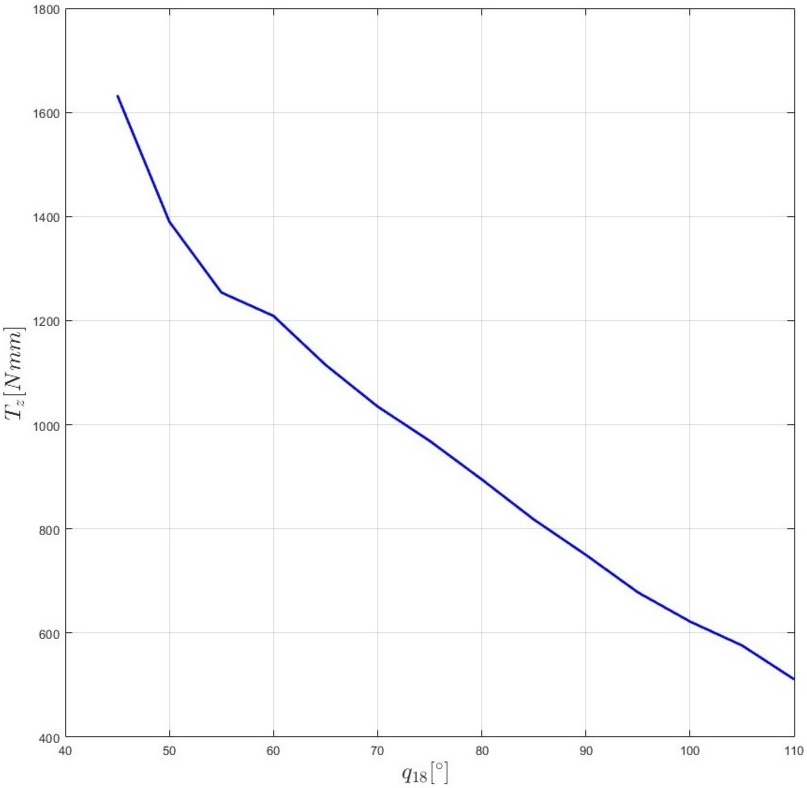

Figure 3.16: The values of the static torque module required in Z (T_Z) as the crank angle changes (q_{18}).

In the Solidworks Simulations environment, component-by-component structural analyses were conducted performing worst-case scenario for each component. The load and constraint configurations taken into account are shown in Figure 3.17. Constraints were imposed so as to obtain isostatic configurations by recreating as faithfully as possible the constraint conditions imposed by the kinematic chain.

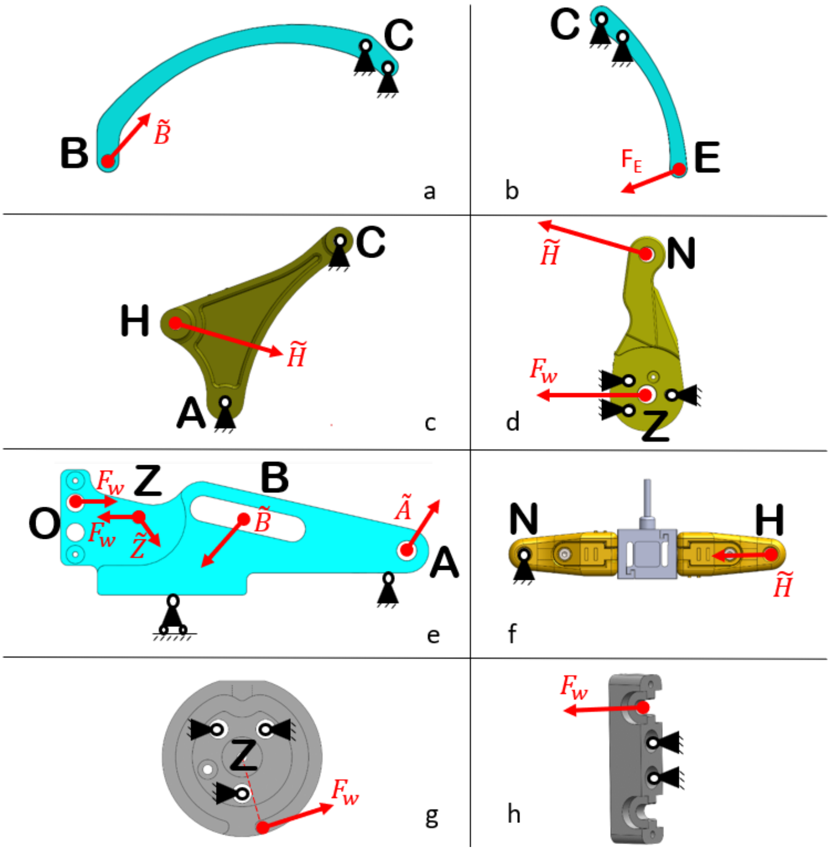
C
B
$\tilde{B}$
a
C
F_E
E
b
C
H
$\tilde{H}$
A
c
$\tilde{H}$
N
F_w
Z
d
F_w
Z
B
O
F_w
$\tilde{Z}$
$\tilde{B}$
$\tilde{A}$
A
e
N
H
$\tilde{H}$
f
Z
F_w
g
F_w
h

Figure 3.17: The load and constrain set applied as boundary condition to fem analysis for the von Mises stress detection.

The von Mises stress patterns are shown in Figure 3.18, while the maximum values obtained from the solutions of the performed analyses are collected in the Table 3.4 along with the resulting safety factors related to the yield stress of the selected materials. The lowest safety factor is around 1.5; from a mechanical resistance point of view, the components of the system can be considered well-dimensioned since, under the worst operating conditions, they work far from the yield condition.

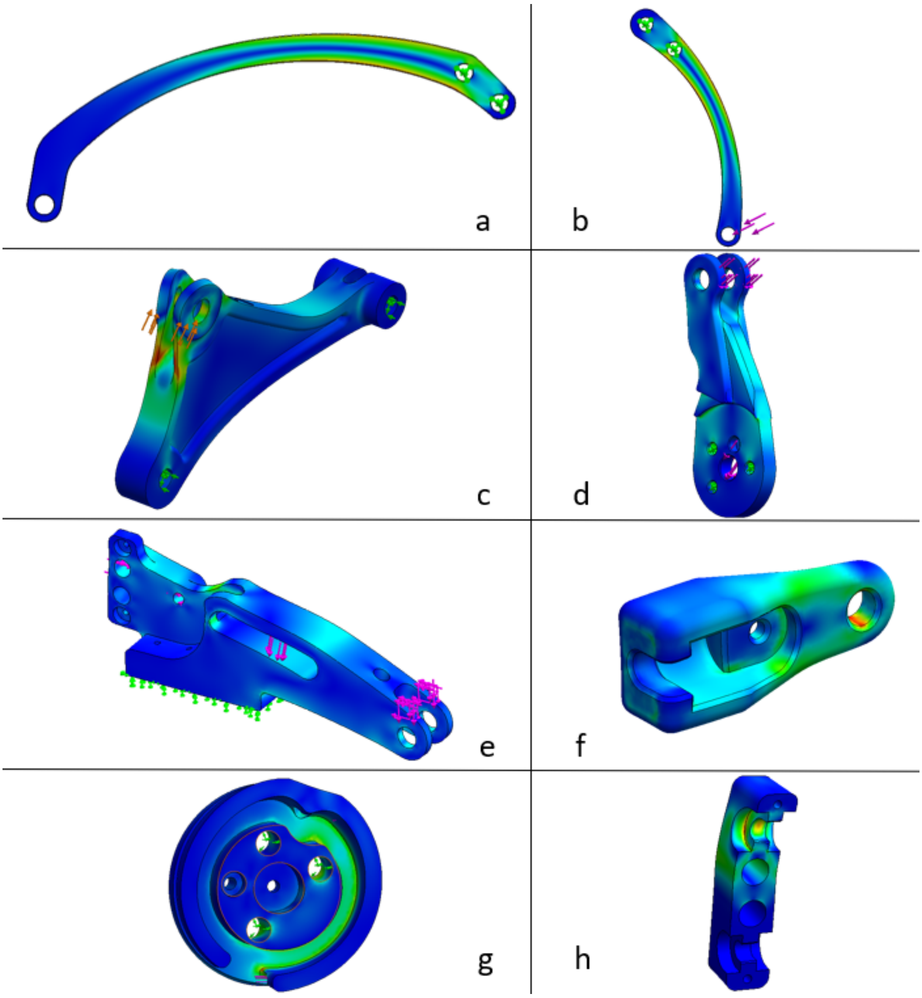

Figure 3.18: The von Mises stress diagram resulting from fem analysis, with stresses at increasing magnitude from elements colored in blue to those in red.

Component	Von Mises stress	Yield stress	Safety factor
link BC	25	280	11.5
link CE	85	280	3.2
front crank	7	31	4.4
rear crank	20	31	1.6
frame	15	130	8.7
capstan	120	200	1.7
block system	60	200	3.3

Table 3.4: The maximum von Mises stress (MPa) resulting from fem analysis, the Yield stress (MPa) of the corresponding material, and safety factor.

3.5.2 Stiffness analysis

The stiffness analysis was conducted by using the same geometries and materials employed and described in the stress analysis described in 3.5.1.

The objective of this type of study is to assess the behavior of the assembled mechanism under load by evaluating the displacement of the end-effector (ΔE). This can be simulated by blocking the rotation of the rear crank and applying the force to evaluate at the end-effector. An example of load and constrain system is shown in Figure 3.19.

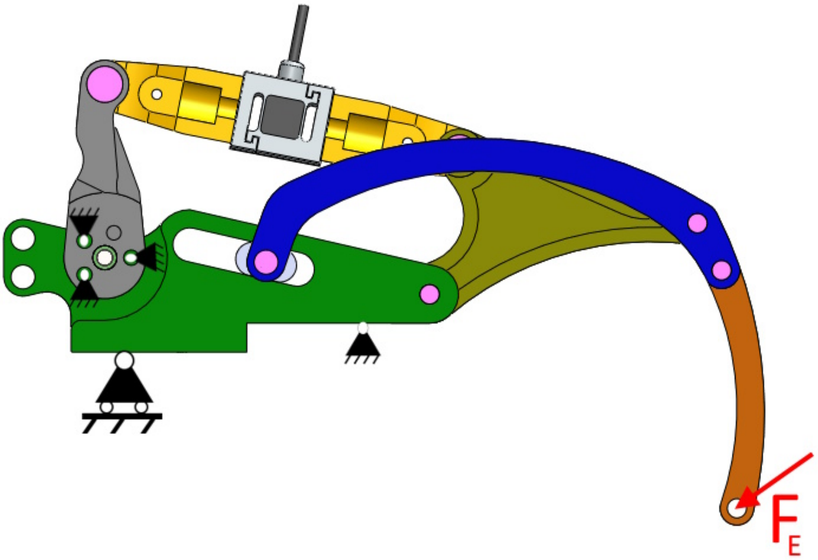

Figure 3.19: The load and constrain set applied as boundary condition to fem analysis for the stiffness analysis.

Figure 3.20 shown the displacements of the E point resulting from static analysis conducted in Solidworks Simultaion environment. Each result has been obtained considering a force with module of 15 N, the maximum operating value, and a direction according to the force profiles displayed in Figure 3.9.

The results show that the deflection of the mechanism is minimum at the maximum opening of the hand and increases until the full closure. In numeri-

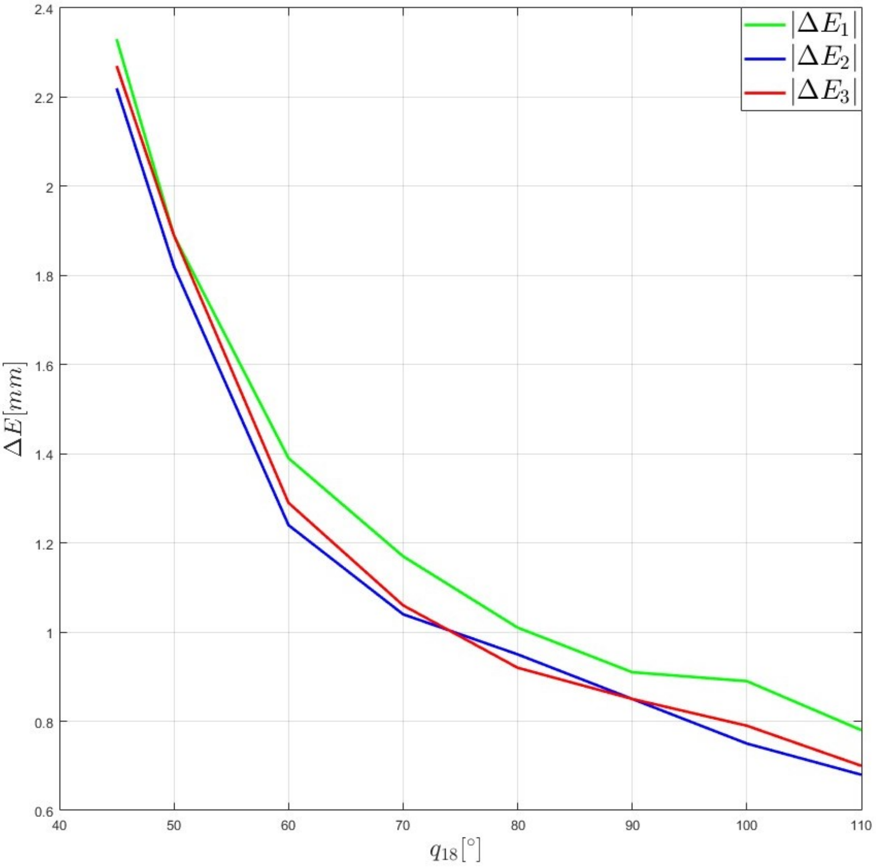

Figure 3.20: ΔE_1, ΔE_2, and ΔE_3 are the displacements of the E point under the application of force profiles of subject 1, subject 2, and subject 3 respectively shown in Figure 3.9.

cal terms, the deflection at the end-effector in the range of motion considered assumes values between 0.7 and 2.3 mm, acceptable values for the operative functioning of the device attesting to the validity of the choice of materials.

3.6 HMI-force filter

It is worth noting that Equation 3.14 provides the analytical formulation of the force measured by the load cell when a known force F_E is applied to the mechanism end-effector in a specific mechanism pose q_{18} (please note that q_{15} is a function of q_{18}, see Equation 3.7). Unfortunately, F_E does not appear directly in that formula, but it depends on the Lagrange multipliers (solution of Equation 3.12), and therefore Equation 3.14 doesn't state an explicit relation. Nevertheless, it is also important to note that the system, not including friction and viscous forces, is linear to the modulus of the external loads; therefore, it is possible to express the relation between the H reaction and the modulus of F_E as follows:

$$|F_E| = K(q_{18})\tilde{H_x} \tag{3.21}$$

Where $K(q_{18})$ is an unknown function of the rear crank angle that expresses proportionality between the two forces of interest.

Knowing the HMI force orientation as a function of q_{18}, the force profile obtained in section 3.2 for the subject 1 (Figure 3.9) was taken as a reference in this context, and by solving Equation 3.21, with the unitary modulus of F_E, it was possible to derive the value that K takes for the sampling angles; collected in Table 3.5.

K(45°)	0.23
K(50°)	0.28
K(55°)	0.32
K(60°)	0.34
K(65°)	0.38
K(70°)	0.42
K(75°)	0.45
K(80°)	0.5
K(85°)	0.55
K(90°)	0.59
K(95°)	0.65
K(100°)	0.7
K(105°)	0.75
K(110°)	0.82

Table 3.5: The coefficients of the Equation 3.22 calculated for the subject 1.

Through a best-fitting approximation operation, the function $K(q_{18})$ was approximated by a third-order polynomial function (Figure 3.21), described by the following equation, with a, b, c, and d coefficients reported in Table 3.6.

$$K = aq_{18}^3 + bq_{18}^2 + cq_{18} + d \tag{3.22}$$

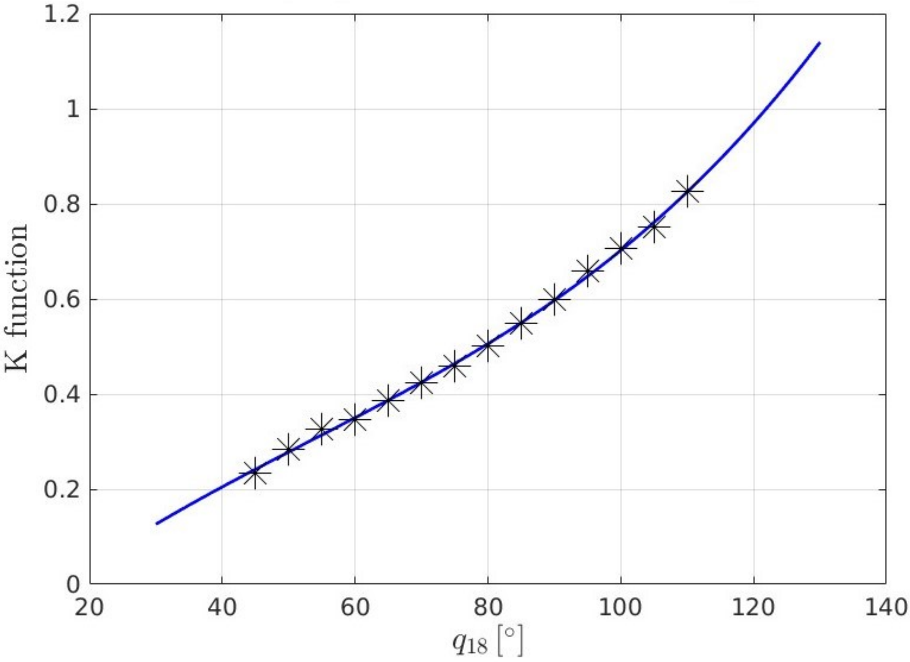

Figure 3.21: the best fitting polynomial of the K points collected in the Table 3.5.

a	b	c	d
$6.3\cdot10^{-7}$	$-1\cdot10^{-4}$	$1.2\cdot10^{-2}$	-0.2

Table 3.6: The coefficients of Equation 3.22 calculated for the Subject 1.

Combining Equations 3.21 and 3.22 yields Equation 3.23, which throughout the text will be referred to as the HMI-force filter. This algorithm, using the load cell and encoder measures ($\tilde{H}_x$ and q_{18}), estimates the HMI force on the thimble (F_E); an indispensable reference value to be fed to the control algorithms aimed at rendering the kinaesthetic interaction.

$$|F_E| = (aq_{18}^3 + bq_{18}^2 + cq_{18} + d)\tilde{H}_x \tag{3.23}$$

3.6.1 Analytical evaluation of the HMI-force filter

The error committed by HMI-force filter with the polynomial approximation was analytically evaluated for F_E ranging from 0 to 15 N, which is the expected operating range for the device. For each F_E force, Equation 3.12 was solved and the constraining force $\tilde{H}$ was calculated through Equation 3.14. Using the HMI-force filter (Equation 3.23), the estimated $|F_E|$ were subsequently calculated. Figures 3.22 and 3.23 show, respectively, for each $|F_E|$ value the average (e_a) and maximum (e_{max}) absolute error committed during the range of motion. The average percentage ($e_{\%}$) error results constant as the $|F_E|$ varies and is 3.4%. The results show a satisfactory estimation of the F_E modulus through the use of the HMI-force filter, having obtained errors of low magnitude. The maximum error, especially for the most intense forces, is around 0.2 N, which determines the maximum resolution to which one can aspire for reference force control by using the introduced HMI-force filter.

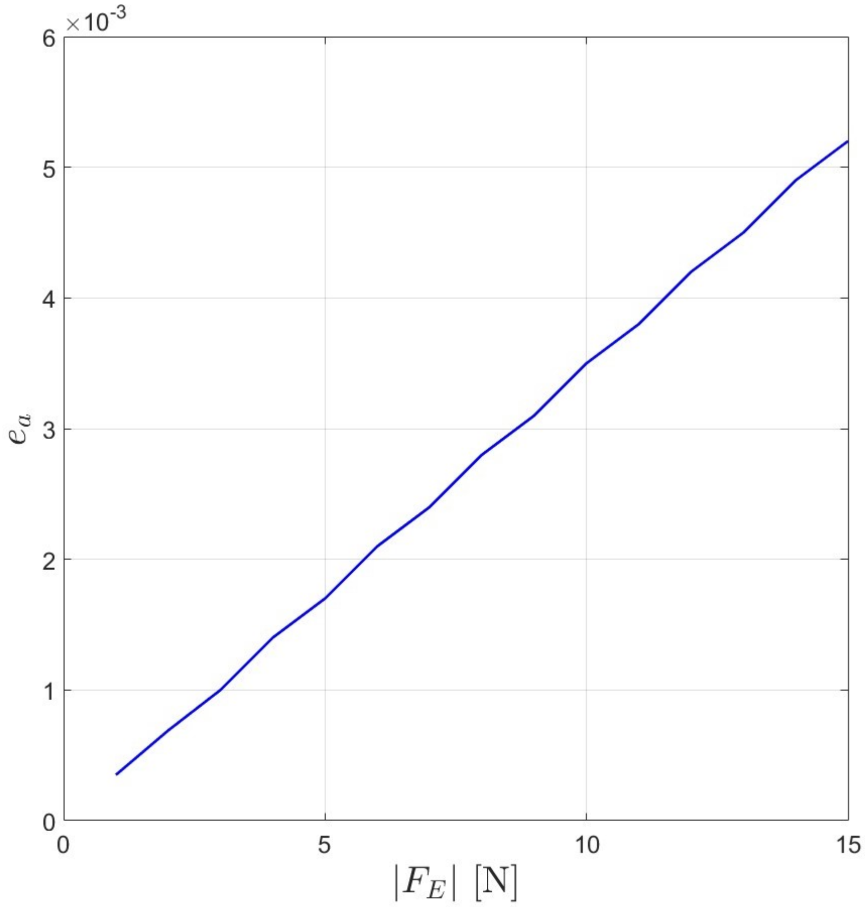

Figure 3.22: the average values of absolute error (e_a) committed to estimate the module of the end-effector force ($|F_E|$) by HMI-force filter as the force intensity changes.

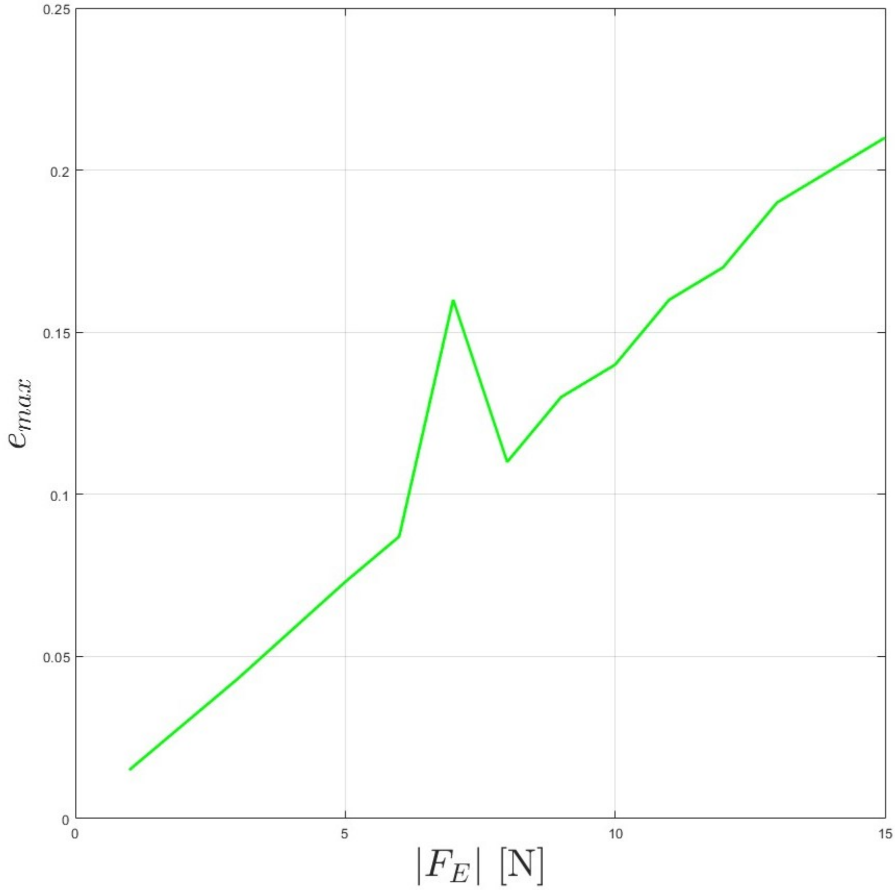

Figure 3.23: the max values of absolute errors (e_{max}) committed to estimate the module of the end-effector force ($|F_E|$) by HMI-force filter as the force intensity changes.

Chapter 4

RAS design

This chapter introduces the actuation system designed to meet the technical specifications established in the first phase of the state-of-the-art study and benchmarking. An initial version has been completed, and its mechatronics architecture will be explained and introduced in Section 4.1. This version was developed with a minimal mechanical design resulting in an open structure that allows for rapid adjustments and improvements, a helpful feature for the first stage of testing and pilot experimentation. A mechanical layout has been proposed and described in Section 4.2, with a closed case and a clearly visible safety button on the top of the device. Finally, Section 4.3 presents the microcontroller firmware for measuring the signals of interest from the sensors mounted on board the FM.

4.1 RAS mechatronics design

As mentioned previously, each finger mechanism is designed to be driven independently. Consequently, the development of the RAS produced a modular mechatronic architecture consisting of three identical Remote Actuation Modules (RAMs), each of which controls a specific finger.

The design of the RAM was approached to drive each finger independently, to ensure a maximum force of 15 N at the end-effector and a high reversibility of the system; a strongly desirable feature for devices that actively interact with the human body. Indeed, a mechanically reversible device has many advantages: high efficiency and, therefore, contained power losses in the transmission

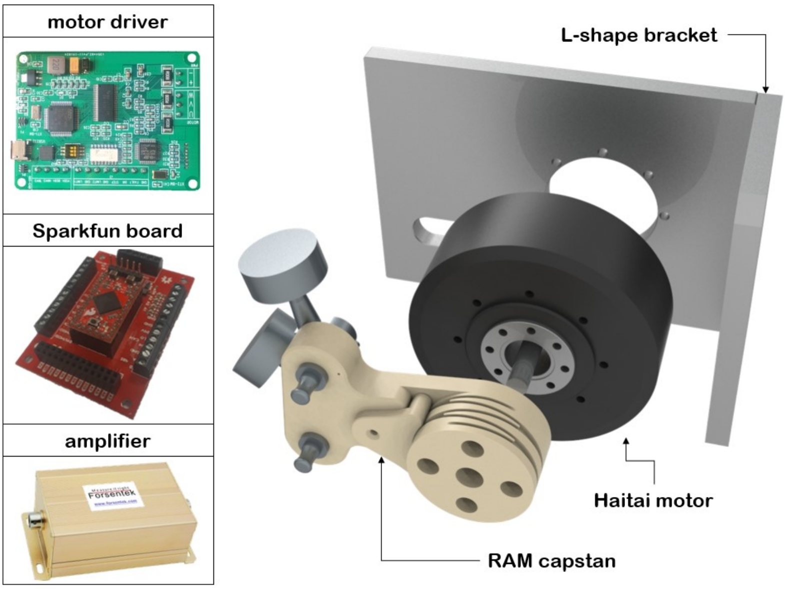

Figure 4.1: Components constituting RAM.

chain; a simplified wearing phase that can be performed with the motors off; the possibility to detect the user's interaction from any point of the mechanism by force sensors; a safe emergency-handling as the device can be always forced by the user in case of malfunctioning.

The scheme adopted involves a brushless rotary in-runner electric motor (the HT1225 from *Haitai Mechanical and Electrical Equipment Co.*), capable of providing sufficiently high torque at a low number of revolutions without any reduction stages in direct drive mode. The latter is an essential feature in terms of reversibility. The motor model employed is equipped with a current sensor and an absolute encoder to monitor both its output torque and angular position.

As shown in Figure 4.2, the motor's output is connected to a custom capstan designed specifically to wrap the cable around a spiral groove. Two pegs per RAM housed on the custom capstan perform the cables' tensioning. This solution allows the RAM capstan to work by friction, redistributing the tensions around the entire circumference of the capstan. The diameter of the RAM capstan has been made four times larger than the IM one to realize a multiplier for the direct drive and a reducer for backward motion, aiming to further amplify the backdrivability of the system.

The module frame comprises two aluminum plates connected to form a L-shaped bracket intended to house the motor and block the Bowden cable sheaths. In addition, the 13mm-thick aluminum plates help the cooling of the motors by thermal conduction.

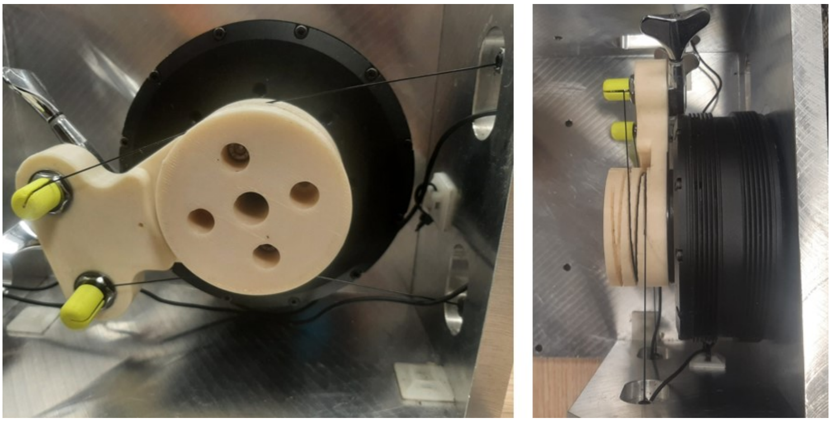

Figure 4.2: lateral and top view of the RAM capstan.

The electronic hardware required, as shown in Figure 4.1, for the functioning of each RAM includes a Sparkfun development board (AST-CAN485 by *SparkFun Electronics*), the motor driver (the model HTPTZ by *Haitai Mechanical and Electrical Equipment Co.*) and a signal amplifier (model FSC 5-24 V by *Forsentek Co.*) for the load cell embedded in the exoskeleton mechanism.

The Sparkfun development board handles mid-level control via the ATmega32U4 microcontroller with a 16MHz processor. Specifically, it samples and processes the analog signals from the load cell, through the amplifier, and from the exoskeleton encoder.

The motor driver (the HTPTZ model from *Haitai Mechanical and Electrical Equipment Co.*) contains firmware to drive the Haitai motor, developed by the same company, equipped with built-in Proportional Integral Derivative (PID) controller to perform speed control of the motor. A proprietary communication protocol allows the monitoring of various parameters, including current consumption, supply voltage, Revolutions Per Minute (RPM), and absolute position.

The electrical/electronic scheme of each RAM requires a constant voltage supply line of 24 V, which is then distributed to power the motor, the motor driver, the load cell amplifier, which in turn powers the load cell mounted on the exoskeleton mechanism, and the Sparkfun development board, which in turn powers the encoder mounted on IM capstan.

As shown in Figure 4.3, the complete RAS is obtained by mechanically and electrically connecting all RAMs to a base plate, which housed the electronic hardware, independent of the number of RAMs necessary for system operation. Such as the input AC-DC transformer (HRPG-1000-24 from *Mean Well*), the onboard computer (Raspberry Pi 4), the external communications connectors, the power button, the emergency button, and some custom electronic boards for voltage distribution and button management.

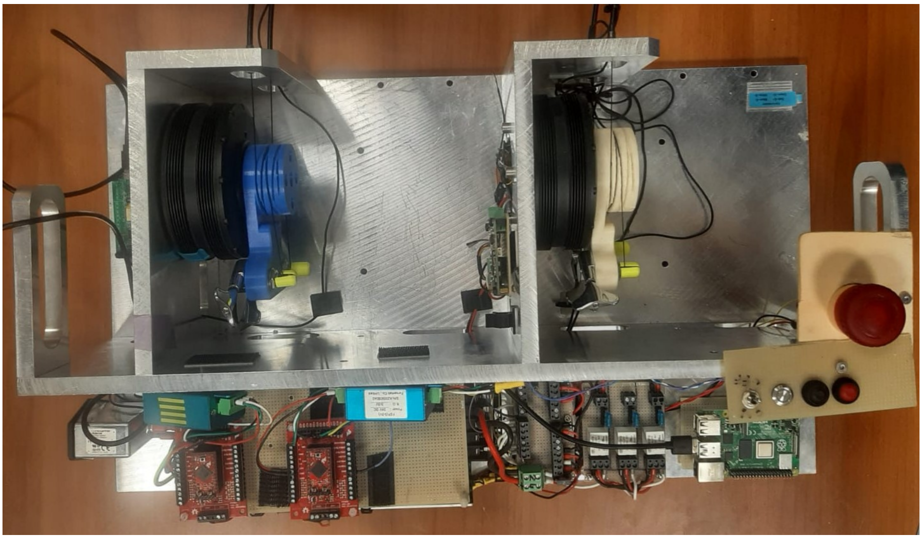

Figure 4.3: A RAS overview including two RAM mounted.

Figure 4.4 broadly summarizes the overall schematic of the RAS and reports the type of communication employed between the processing units, considering only one connected RAM. In detail, the Sparkfun board sends load cell and exoskeleton encoder measures to the Raspberry Pi 4 via I2C communication, which is even communicated with the motor driver via Universal Serial Bus (USB) to send all parameters related to the motor status and receive the speed command at each control iteration. At the current stage of device development, the onboard computer plays the function of a communication interface between the driver and Sparkfun with a main external computer via USB or Ethernet, on which the main framework containing the high-level control runs. This issue will be deeply addressed and explained in Chapter 5.

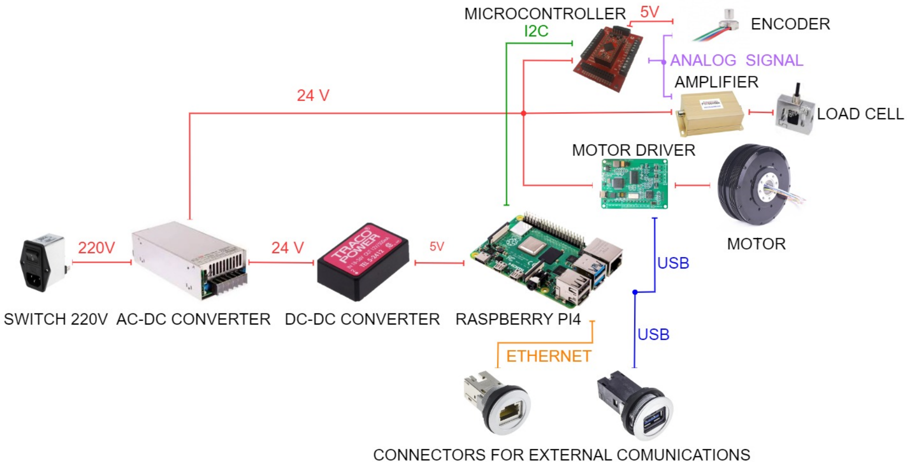
MICROCONTROLLER
5V
I2C
ENCODER
ANALOG SIGNAL
AMPLIFIER
24 V
LOAD CELL
MOTOR DRIVER
MOTOR
220V
24 V
5V
USB
USB
SWITCH 220V
AC-DC CONVERTER
DC-DC CONVERTER
RASPBERRY PI4
ETHERNET
CONNECTORS FOR EXTERNAL COMUNICATIONS

Figure 4.4: An overview of the system electric/electronic scheme. Red lines symbolize power cables, blue lines symbolize USB cables, green lines symbolize I2C cables, orange lines symbolize Ethernet cables, and purple lines represent analog cables.

4.2 The final RAS mechanical layout

The overall structure of the RAS presented in Section 4.1 corresponds to the layout chosen for the opening phase of development, deliberately left minimal since the device presented was intended as an evolving test bench in search of the ideal configuration. Logically, such a layout is unsuitable for field operation, so a final closed version was also developed in anticipation of future clinical trials.

As shown in the Figure **??**, this version includes a case consisting of the assembly of appropriately bent, two mm-thick stainless steel sheets.

The case sizing was designed to accommodate three RAMs along with the functional electronics presented in Section 4.1. Besides, it is also thought to house a Raspberry monitor housed on the top sheet and two fans to ensure properly forced air circulation for cooling the electronics. The resulting overall dimensions and overall weight are given in Table 4.1.

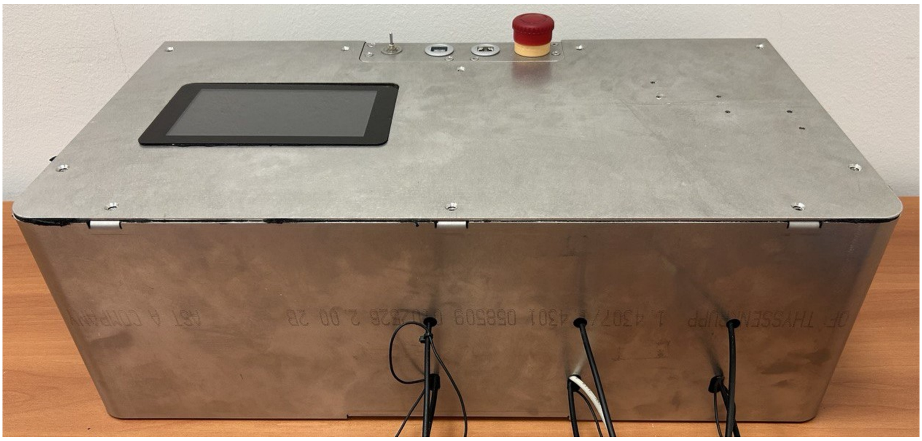

Figure 4.5: frontal view of the final RAS layout.

width (mm)	606
height (mm)	216
depth (mm)	304
mass (kg)	22

Table 4.1: The encumbrance and mass characteristic of the final RAS layout.

4.3 The microcontroller firmware

This Section introduces the algorithms implemented on the ATmega32U4 microcontroller embedded with the Sparkfun development board. As already introduced in Section 4.1, this board has the task of reading analog signals from the sensors mounted on the exoskeleton mechanism: the encoder and the load cell amplifier. As regards the encoder, sampling is done through the methods of the Encoder class available from the Arduino library, which measures the current angle value by comparing two quadrature signals produced by the encoder sensor via two interrupt pins of the development board. The read method of the Encoder class returns a value of type long that corresponds to the angle in ticks that measures the relative rotation between the sensor and magnet since the device was turned on. Knowing the resolution of the encoder employed, 4096, and the number of degrees in one revolution, 360, it is possible to obtain the measure of the current angle in degrees (q_{18}) by the following equation:

$$q_{18} = tick_{current} \frac{360}{4096} \tag{4.1}$$

where $tick_{current}$ is the current measure of the angle in ticks provided by the read method of the Encoder class.

The load cell signal is read from the analog pin A_0 coming from the signal amplifier appropriately calibrated by adjusting the span and zero parameters.

The span enables adjustment of the weight to which the amplifier output saturates at 5V, corresponding to the maximum read voltage of an analog pin on the Sparkfun board.

The zero allows adjustment of the minimum voltage to which the no-load configuration corresponds. In this work, the zero was set to produce a voltage of 2.5 V, which is half of the maximum value that an analog pin can measure so that both pull and compression can be measured.

The span was tuned to the minimum value allowed by the particular amplifier model chosen, 25.5 kg (249 N), to maximize, as much as possible, the resolution of the load cell measurement. The microcontroller chosen in the analog measurement quantizes voltages from 0 to 5 V on a scale of 0 to 1023. Thus, the minimum measurable signal magnitude coincides with the span value divided by 1024; consequently, the lower the span, the higher the resolution of the measurement. In this context, the minimum measurable force results in 0.25 N. At the same time, this span value generates a full scale of measurable tensile and compressive forces of 124.5 N. Threshold values that allow the maximum operating tensile and compressive forces to be widely measured. In fact, from the analysis performed in Section 3.5, 64.2 N (6.56 kg) was found to be the maximum value of the force acting on the connecting rod under the worst working condition.

Chapter 5

HES software

This chapter discusses the software implementation and control architecture. Section 5.1 describes the software architecture of the exoskeleton and the programming logic pursued, introducing the Finger class used to instantiate programming objects with the methods necessary for controlling and managing physical finger exoskeletons.

The control laws currently implemented as methods of the Finger class allow the system to track constant references of motor speed, crank angle, or end-effector force. Motor speed tracking is handled by the PID controller built into the motor driver, while a digital PID controller, whose algorithm will be described in Section 5.2, is implemented to track the two other input signals.

Section 5.3 presents and describes the system GUI, primarily implemented with the goal of real-time control and monitoring of the device.

Finally, Section 5.4 presents the application developed in Unity environment as a robot-assisted physiotherapy rehabilitation tool and kinaesthetic haptics application case.

5.1 Software architecture

The software architecture of the exoskeleton was developed to be run on an external computer, referred to as the main computer from now on, and communicated with the onboard computer, Raspberry Pi 4, via serial USB communication sockets.

Taking advantage of the modular architecture of the system, based on RAM, and FM modules, object-oriented programming was pursued, so once an appropriate custom Finger class is defined, it is possible to create a generic finger exoskeleton software model to generate, by its instances, the actual programming objects representing the physical finger exoskeletons. For each physical finger, the programming strategy involves generating a Python module called FingerRunfile to be processed independently on a dedicated thread, containing a Finger object along with necessary instructions to control and oversee the management of a single exoskeleton finger.

The Finger object becomes representative of a true finger exoskeleton when the parameters required for initializing the various communication sockets, i.e., USB and User Datagram Protocol (UDP) port identifier, boudrate, etc., are defined. In this work, the required communication parameters come from a proper file located in the same directory of the module FingerRunfile produced by GUI, as will be described in Section 5.3.

The core of the software architecture lies in the Finger class written in Python 3 language. That custom class has a mainloop() method, called cyclically within the FingerRunfile module, at a frequency of 300 Hz. This method sequentially calls the instructions necessary for the initialization process at startup, collecting and sending status parameters, receiving external commands, and sending the reference speed for the finger to the Raspberry Pi 4.

The initialization process consists of identifying the exoskeleton's end stops, shown in Subsection 3.1.3, to have a reference of the RoM that is operable at the software level. This procedure is also essential for zeroing the relative encoder mounted on the IM. In detail: at starting up, the exoskeleton is closed with constant speed, monitoring the torque provided by the motor; when this exceeds 3 Nm, it means that the rear crank has reached the closing end-stop. The corresponding value of the IM's relative encoder is saved as reference, subtracting it from all further measurements coming from the microcontroller. Subsequently, the FM is opened with constant speed until it reaches the opening end-stop, at which it stops and stores the current position. These two values are then used as upper and lower bound of the admissible RoM for the finger exoskeleton.

Status parameters, coming from Raspberry Pi 4, are collected via the local communication network of the device discussed in Section 4.1, e.g., motor torque, motor current, motor rpm, crank angle, and load cell measurements. The latter signal, discussed in Section 4.3, is processed through a moving average filter over 30 samples, and at initialization, or following a specific command from the GUI, software calibration is performed to compensate the eventual offset, i.e., the current average value is subtracted from all subsequent samplings.

The Finger class was also programmed with a method that executes the

HMI-force filter algorithm, deeply discussed in Section 3.6, to reconstruct the force at the end-effector. This value, along with the other state variables, is packed into a single variable with a dictionary structure and sent to the GUI via a UDP socket communication channel by means of a local network port.

The UDP communication between local ports was necessary because the GUI application was designed to be run on a dedicated thread on the main computer that runs in parallel with the thread dedicated to the FingerRunfile module on which the mainloop() method of the Finger object is cycled. This strategy brings multiple advantages both at the security level, because any crashes or anomalies arising from the GUI are less likely to trigger anomalous and dangerous device behaviors, and at the functional level since it is possible to manage the GUI and the exoskeleton at different frequencies. The FingerRunfile module that performs the control and processing methods of the acquired signals is run at a high frequency (300 Hz), while the *Finger GUI*, which was meant for interaction and visualization purposes, is updated at significantly lower frequencies (50 Hz).

Through another UDP socket, a Finger object can receive incoming commands from the GUI. Currently implemented commands establish the tracking of a constant input in position, velocity, or force. Following a specific command, specific instructions are executed within the FingerRunfile module, i.e., the method containing the digital PID controller, described in Section 5.2, which processes instantaneous speed steps to move the motor. These speed references are delivered to the motor driver by means of the onboard computer. Thus, within the control logic implemented, the Raspberry Pi 4 at a certain frequency (300 Hz) is responsible for collecting the device status parameters, packing and sending them to the main computer, and then receiving from the FingerRunfile the speed references to be delivered to the motor driver.

Figure 5.1 shows a summary diagram of the communication flow existing in the system and managed by the software architecture. The green lines represent the flow of data, starting from the sensors and ending in the GUI after being processed by the FingerRunfile module. The red line, on the other hand, represents the command line that following a direct request from the GUI is transformed into a command speed to be delivered to the motor after being properly processed by the FingerRunfile module.

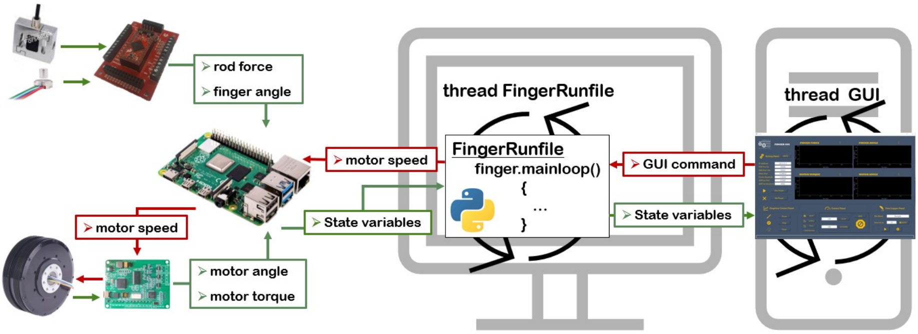
rod force
finger angle
thread FingerRunfile
thread GUI
motor speed
FingerRunfile
finger.mainloop()
{
...
}
GUI command
State variables
State variables
motor speed
motor angle
motor torque

Figure 5.1: Summary diagram of the communication flow existing in the system and managed by the software architecture.

5.2 Digital PID algorithm

The ideal PID controller is a Single Input Single Output (SISO) system that uses only the scalar deviation error $e(t)$ as input, producing a scalar control signal $u(t)$ as output, obtained by a law proportional to $e(t)$, its derivative, and its integral. This definition is expressed through Equation 5.1.

$$u(t) = K_p e(t) + K_i \int_0^t e(\tau) d\tau + K_d \frac{de(t)}{dt} \tag{5.1}$$

Where the first addend is called the proportional action, the second the integral action, and the third the derivative action. The gain values K_p, K_i, and K_d constitute the parameters that can be changed to adjust the behavior of the PID controller and represent its degrees of freedom during device configuration. Usually, in industrial settings, the preceding parameters can be manipulated only indirectly by setting as many equivalent parameters more representative of the effects of configuration on device behavior. The parameters directly accessible in real devices, also called industrial parameters, are the proportional gain (K_p), which determines the minimum amplification to be applied on the deviation error to generate an effective control signal; the integral time constant or reset constant (T_i), determines the useful operating band at low frequencies; and the derivative time constant (T_d), identifies the useful operating band at high frequencies.

Equations 5.2, and 5.3 give the definitions of T_i and T_d, respectively.

$$T_i = \frac{K_p}{K_i} \tag{5.2}$$

$$T_d = \frac{K_d}{K_p} \tag{5.3}$$

The control law of the ideal PID is linear and time-continuous with concentrated parameters. Mathematically, therefore, it can be written as a transfer function in the Laplace domain in the following form:

$$C(s) = K_p \left(\frac{T_i T_d s^2 + T_i s + 1}{T_i s} \right) \tag{5.4}$$

The ideal PID controller, however, is a non-causal system; processing its output at present requires knowledge of its future input. Therefore, an actual PID controller is constructed from a causal realization of the ideal control law; the device processes its strategy through a law that approximates the non-causal one concerning some optimal criterion. The element responsible for the loss of causality in the ideal PID is the derivative action, characterized by a transfer function with a degree of the numerator greater than that of the denominator.

The approach to the causality problem is to find a causal law that can approximate the derivative action with due accuracy. The simplest solution is to correct the derivative action by bringing the degree difference between the denominator and numerator of its transfer function to a non-negative value. The easiest way to achieve this is to add a simple pole in the derivative action, resulting in the following transfer function:

$$\hat{C}(s) = K_p \left(1 + \frac{1}{T_i s} + \frac{T_d s}{1 + \frac{T_d}{N} s} \right) \tag{5.5}$$

Where N is a positive real number and $s = -N/T_d$ turns out to be the additional pole. Usually a value between 5 and 30 is assumed for N.

In this context, a value of N equal to 5 was considered. For the implementation of the digital PID controller, it is necessary to discretize the formulation of the transfer function of the continuous-time controller, reported in Equation 5.5, using the forward Euler method for the discretization of the integral action and backward Euler for the discretization of the derivative action. The resulting algorithm to calculate the digital PID controller output at the k instant (u_k) is described by Equation 5.6.

$$
\begin{aligned}
u_k = \frac{T_N+1}{T_N}u_{k-1} - \frac{1}{T_N}u_{k-2} + K_p\frac{T_N+N}{T_N}e_k + \\
+\frac{K_p}{T_N}\left(T_N\frac{T_c-T_i}{T_i}-2N+1\right)e_{k-1} + \frac{K_p}{T_N}\left(1+N-\frac{T_c}{T_i}\right)e_{k-2}
\end{aligned}
\tag{5.6}
$$

After a heuristic tuning process, the digital PID parameters were selected to perform convergent step input tracking. Figures 5.2 and 5.3 report the system's performance in trajectory tracking in position and force, respectively, qualitatively judged satisfactory for the application under consideration considering the current level of device development.

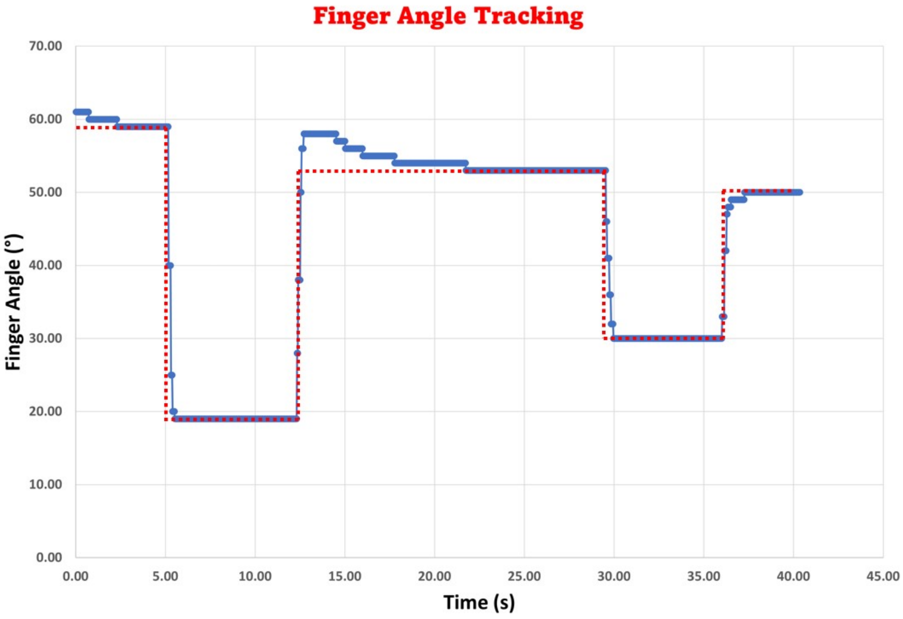

Figure 5.2: The blue line represents the encoder measurement, while the red line represents the reference value to be tracked.

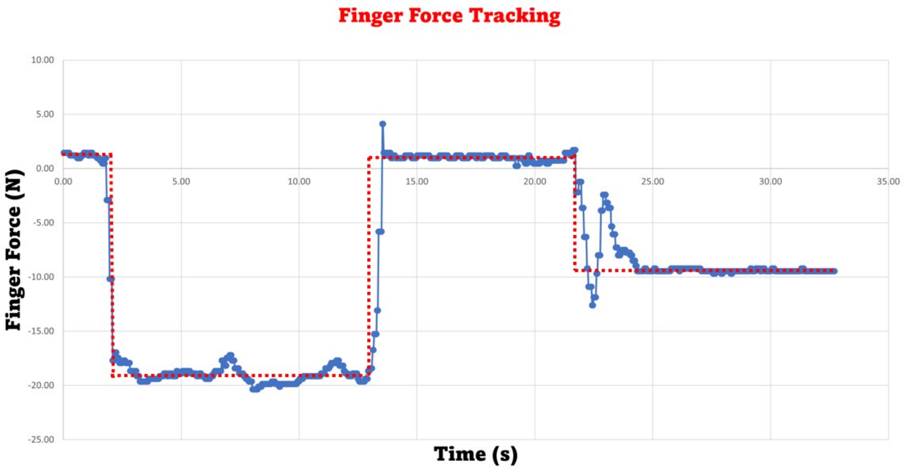

Figure 5.3: The blue line represents the HMI-force value, while the red line represents the reference value to be tracked.

5.3 Finger GUI

In the era of Industry 4.0, it is an established practice to interact with robotic devices by providing routine commands and display data using graphical applications that give immediate visual feedback. The interface by which the user interacts with the machine by controlling conventional graphical objects via keyboard and mouse, replacing human-machine communication based on command lines. Thus, it is a visual representation that includes icons, sliders, text boxes, and buttons. Commands are given through a pointing device (such as a mouse) on a high-resolution image screen by clicking on specific buttons to execute the corresponding instructions. A GUI thus combines the graphical aspect with event-programmed functions.

The GUI of the device under consideration was developed on Qt framework through the use of PyQt5 libraries in Python language and was finalized for single finger handling, hence named *Finger GUI*, as a workbench for the development and testing phase. However, it represents a more than reliable base for future implementation for the simultaneous handling of multiple fingers. The structure of the *Finger GUI* is a single window application with a purpose-oriented layout, dividing the window area into panels with specific purposes.

As shown in Figure 5.4, the following can be distinguished: the setting panel, the control panel, the panel for saving and exporting data, and the panel for managing plotted graphs in the dedicated graphics area. Finally, there is a dedicated text box in the lower area of the window to deliver messages to the user following specific events, such as certifying the correct execution of the sent command or reporting the detection of a specific error.

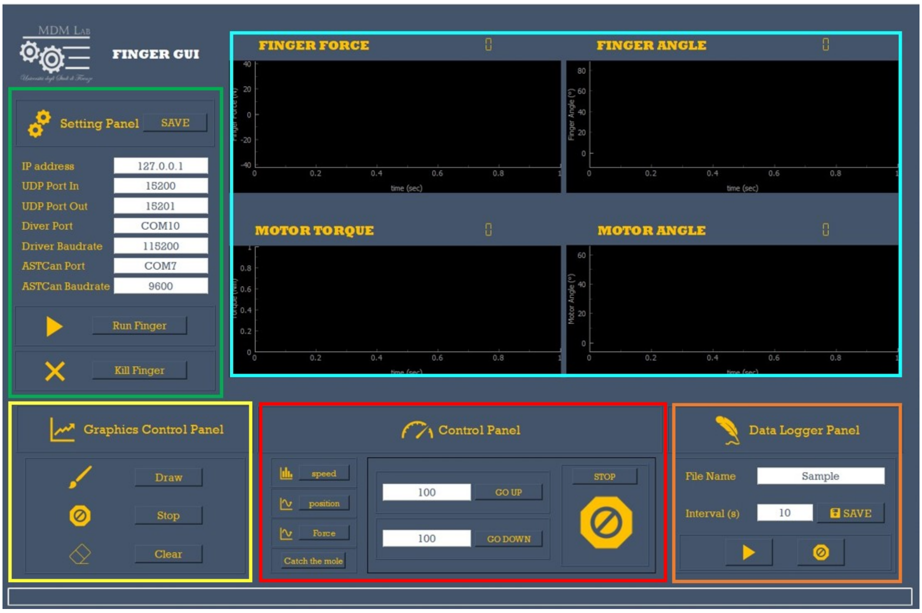
MDM Lab
FINGER GUI
Setting Panel
SAVE
Run Finger
Kill Finger
FINGER FORCE
FINGER ANGLE
MOTOR TORQUE
MOTOR ANGLE
time (sec)
Finger Force (N)
Finger Angle (°)
Torque (Nm)
Motor Angle (°)
Graphics Control Panel
Draw
Stop
Clear
Control Panel
speed
position
Force
Catch the mole
GO UP
GO DOWN
STOP
Data Logger Panel
SAVE

IP address 127.0.0.1
UDP Port In 15200
UDP Port Out 15201
Diver Port COM10
Driver Baudrate 115200
ASTCan Port COM7
ASTCan Baudrate 9600

100
100

File Name Sample
Interval (s) 10

Figure 5.4: An overview of the *Finger GUI* with colored frames highlighting the various panels. Specifically: the setting panel, in green; the control panel, in red; the data logger panel, in orange; the graphics area, in blue; the graph control panel, in yellow; and the text box, in white.

The Setting panel allows via text boxes to enter all those parameters necessary for communication with the onboard computer, Raspberry Pi 4, and UDP ports identification, i.e., name of the serial USB port, boudrate value of the socket USB communication, UDP port number, and Internet Protocol (IP) address. After pressing the save button on this panel, the application generates a parameter sheet containing the setup data, saved within the folder where the GUI application executable is allocated and made available for the FingerRunfile method. After that, the Run Finger button can be used to execute the instructions to run the FingerRunfile module on a dedicated thread in parallel to separate the system GUI from the module that manages the exoskeleton. Finally, the Kill Finger button allows the thread that processes the FingerRunfile module to be terminated, an operation necessary to close the application.

The Control panel was implemented by means of a stacked widget that allows the contents of a certain portion of the panel area to be changed by clicking the specific buttons: speed, position, force, and *Catch the mole*, located on the left side of the panel. As their assigned names suggest, the speed, position, and force buttons pop up all the necessary widgets (buttons and text boxes) to make the exoskeleton truck speed, position, or force step references, respectively (Figure 5.5). The reference speed is directly passed to the driver, which guarantees the tracking via its built-in PID, while the trajectory tracking of the steps in position or force is handled by the digital PID controller implemented in the Finger class and discussed extensively in Section 5.2. As shown in Figure 5.5, the ability to set and modify PID parameters via dedicated text boxes has also been included, a useful feature for the first testing and tuning phase, but to be removed in the eventual release intended for the end user. The *Catch the mole* button pops up the widgets necessary for initializing and starting the *Catch the mole* application executable, containing the specially developed serious game in Unity environment as an example of an operation that will be more thoroughly presented in Section 5.4. By programming an appropriate flag, the application executable can only be launched after the FingerRunfile module has been started so that proper communication between the parts is established via a dedicated UDP port.

The Graphics Control Panel contains buttons designed to manage the display of some system status variables in the form of Cartesian graphs in the apposite dedicated areas, with the sampling times on the x-axis and the values of the status variables on the y-axis. The state variables that can be displayed are exoskeleton angle, end-effector force, motor torque, and motor angle, which are considered in the experimentation, assessment, and tuning process to be of greater interest and usefulness than the others.

The data logger panel allows state variables to be saved into a .csv format file generated within the folder containing the application executable for possible post-processing analysis of the collected data.

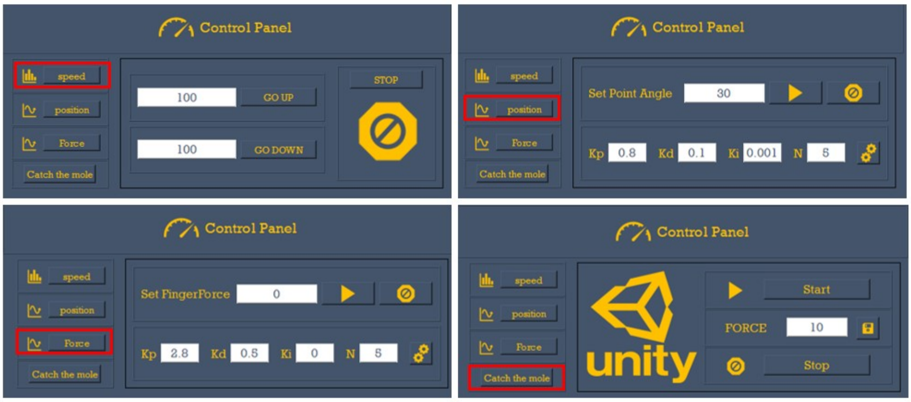

100 GO UP

100 GO DOWN

Set Point Angle 30

Kp 0.8 Kd 0.1 Ki 0.001 N 5

Set FingerForce 0

Kp 2.8 Kd 0.5 Ki 0 N 5

FORCE 10

Figure 5.5: An overview of the four pages of the Control panel. Each layout results from pressing the button highlighted with the red frame.

5.4 Catch the mole application

In the course of this thesis work, a serious interactive game was fully implemented as a test bench for developing and validating the proposed HES. The application *Catch the mole* was developed to stimulate and train the sensorimotor apparatus necessary to perform the kinaesthetic gesture of spherical closing grasp. As introduced in Section 5.3, the executable of this application is made to run on the main computer, and it can be launched from the *Finger GUI* only if the FingerRunfile module is already active so that the UDP communication socket between the local network ports is established correctly at application startup. In addition, the digital PID, managed by the FingerRunfile module, is activated at startup with zero reference force.

The game in question consists of a digital reinterpretation of mole-catching with a hand-shape avatar. The IM encoder's signal controls the avatar's pose, recreating within the application a digital version of the user's hand that replicates the fingers' actual flexion/extension movements. Trivially, the game aims to have the user catch the most number of moles in a given time interval.

In addition to sending the crank-angle values, a UDP socket is employed by the *Catch the mole* application to report to the GUI, via an appropriate flag, if the avatar is in capture mode. This mode is triggered when the three fingers: index, thumb, and middle finger, all make contact with the mole, and when this occurs, the *Finger GUI* receives a signal to change the reference force from 0 to the capture value.

The applicable capture forces generate fingers opening with constant intensity from 0.5 to 15 N. This value is introduced by the appropriate text box of the GUI control panel before running the application so that the user's hand closure can be trained with preset levels of force.

The game scene is set in a meadow portion where ten disks can be distinguished: nine brown and one red. The brown ones represent the areas where the digital mole can appear and be reachable by the avatar by pressing specific keys on the keyboard. The red disk awards points to the user when the player drops the captured mole into it.

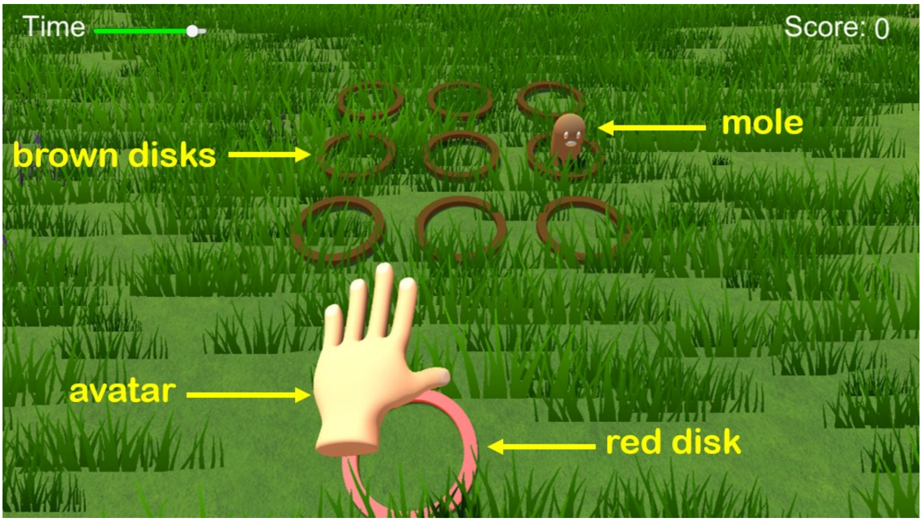

Figure 5.6: Opening scene of the *Catch the mole* application.

At the start of the game, as shown in Figure 5.6: the avatar is placed on top of the red disk, the countdown is started, and a digital mole is randomly generated in one of nine predetermined locations. After the avatar has reached the position where the mole has appeared, the user can proceed to capture it by closing the hand. Once the capture mode is triggered, in a predetermined amount of time, depending on the chosen training intensity, the avatar automatically travels from the capture zone to the red disk, dragging the digital mole with it. The exoskeleton attempts to force the fingers as long as the three fingers remain in contact with the mole. The moment one of them ceases the contact with the mole, the reference force returns to zero, and the digital mole falls toward the ground simulating the action of gravity, and then disappears and reappears randomly in one of nine predetermined areas. Thus, the user gets the point only if he or she can fight the action of the exoskeleton until the avatar stands over the red disk with the mole and then drops it inside it. The catching mole procedure is depicted in Figure 5.7. User involvement is induced by the stimulus of making the most points, triggering the goal of improving with each run.

It is important to remark that during the gaming session, the status parameters, indicative of the user's efforts, are directly visible in real-time from the *Finger GUI* and can be exported into .csv file, as previously discussed in the dedicated Section 5.3. Feature of great interest to the clinical operator who has the opportunity to evaluate the rehabilitation session through actual empirical data.

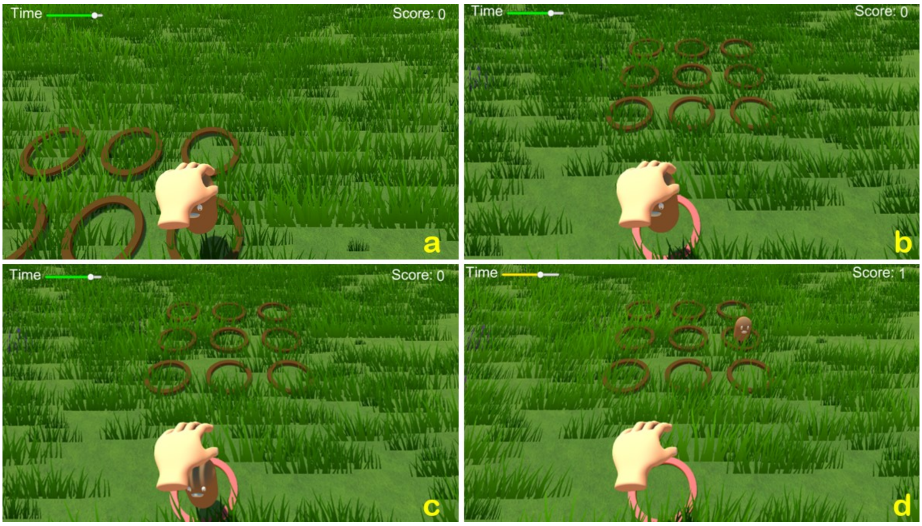

Figure 5.7: A progressive sequence of the digital mole capture procedure. Subfigure a depicts the initial phase of the capture, b the reaching of the red disk of the avatar with the captured mole, c the release of the mole within the red disk, and d the point assignment and respawning of the mole to a new location.

Chapter 6

Test and evaluation

This Chapter presents and discusses the results obtained during the testing phase aimed at evaluating and characterizing the proposed HES.

An assessment of the quick-magnetic couplings was carried out to quantify the time required for the device setup; it will be described in Section 6.1.

The Chapter continues with Section 6.2, which presents a custom bracket to adjust the orientation of the FM concerning the gravity direction. This component resulted fundamental to accomplishing the experimental campaigns for the detection of the minimum backdrive force, which will be described in Section 6.3, and for the validation of the dynamic model and HMI-force filter, addressed respectively in Sections 6.4 and 6.5.

6.1 Assessment of the quick-magnetic couplings

The presented HES, as described in Section 3.1, presents a modular design based on quick-magnetic couplings between the different modules. The primary functionality of such couplings is to provide a fast assembling/disassembling of the device without requiring any tools. This characteristic is crucial to allow for a quick and easy HES setup according to different hand sizes, as wearing the whole system at once can be extremely hard.

A chronometric analysis has been performed to quantify this feature involving five untrained healthy individuals who have been instructed to complete the FM-BP and FM-IM couplings. In addition, to give a minimal statistical value to the test, each trial has been performed five times by each subject.

The Figure 6.1 displays the mean duration required for each attempt to complete FM-IM coupling, and FM-BP coupling.

This analysis showed a mean time, obtained by averaging the mean values for each individual, of approximately 19.1 seconds for FM-IM, and 4.5 seconds for FM-BP. Combining these two results, it arises that a time of about 25 seconds per FM is required to setup the device every time a different-sized hand is involved. Since the maximum number of employable FMs is four, the maximum time required to prepare the HES is roughly 100 seconds.

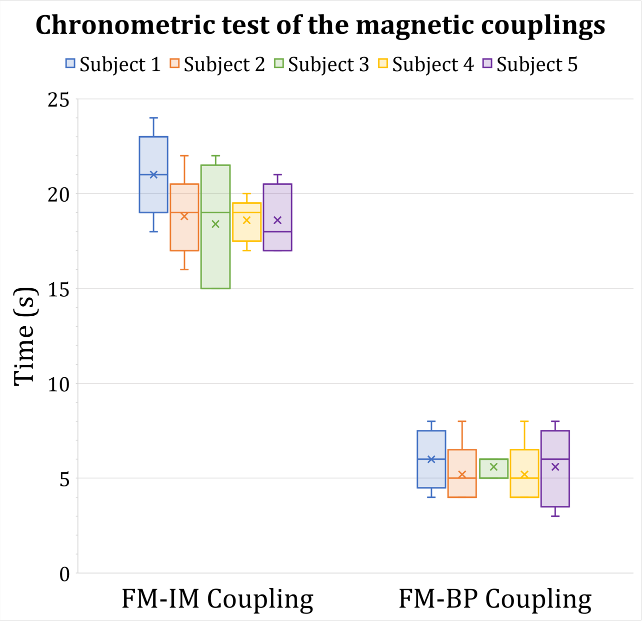

Figure 6.1: The mean time (s) required by the five different subjects for the completion of FM-IM and FM-BP couplings.

6.1.1 Discussion of the modular design results

The modular design based on customized magnetic couplings has arisen as a convenient way to rapidly setup the device according to different hand sizes. The assessment of the quick-magnetic couplings has been introduced in the test campaigns as the proposed system is the only rigid exoskeleton in the state-of-the-art that addresses the size change issue. Actually, a large number of exoskeletons, especially assistive ones, usually manage to circumvent this issue by being tailored for a single user. However when it comes to devices more similar to training platforms where the users may be multiple in a very short range of time, this kind of problem is poorly addressed; especially for rigid exoskeletons. In fact, the *Glorea Sinfonia* soft glove [45] provides the only state-of-the-art example. The results obtained in Section 6.1 demonstrate the value of the proposed modular design as the average interval to set the system up is around 100 seconds, considering the four-FM configuration.

6.2 Adjustable bracket

The experimental tests conducted on the device, which will be described in the following Sections, demanded the possibility of applying a force with a known modulus and direction to the end-effector. To meet this need, a custom bracket with a variable and graduated orientation basement was made so that the FM could be rotated until the desired force to the end-effector results globally directed along the vertical direction. As shown in the Figure 6.2.

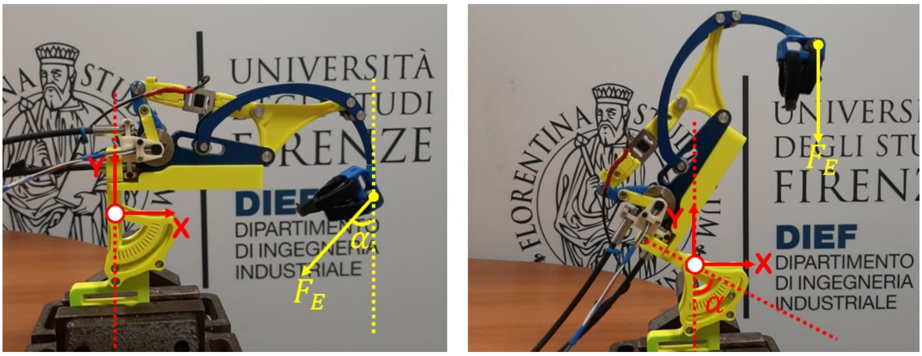

Figure 6.2: The custom bracket equipped with a adjustable orientation basement.

6.3 Minimum backdrive force

One of the key features of the system under consideration, as outlined in the Section 1.3, is the backdrivebility. This characteristic can be interpreted as the minimum value of retrograde force (referred henceforth as backdrivebility force) to allow proper off-motor operation when required. A small experimental campaign has been conducted to quantify this force as a function of the pose of the finger.
For each sampled crank angle, the FM was oriented by the adjustable-orientation-base bracket (Figure 6.2) so that the direction of the gravitational force coincides with the direction of the interaction. The HMI-force direction taken as a reference for performing the experimental test is that performed by the Subject 1, according to the results reported in Section 3.2.
The backdrive force has been identified by increasing the force at the end-effector through the gradual application of weights until spontaneous motion occurred. The tests have been carried out with a cable tensioning value between 2-3 kg; a reference value for the operational functioning, empirically evaluated as a compromise between response speed and stiffness of the transmission chain.
Figure 6.3 shows that the backdrive force ranges from a minimum of 0.5 N to a maximum of 3.5 N.

6.3.1 Discussion of the system backdrivebility results

The entire transmission chain has been developed to preserve backdrive motion, an essential characteristic to reduce the time and effort required during the wearing phase and guarantee safe use. Such feature, also provides a reasonable safety margin if the device is used for medical applications (e.g., in case of muscle spasms).

Dedicated tests, described in Section 6.3, have allowed for the characterization of the backdrive force with motors off as a function of the FM pose. The results underlines that, even in the worst of the operating configurations, the backdrive force does not exceed 3.5 N; which is about 5.4% of the ultimate force ($\simeq 65$ N) that the fifth percentile of the healthy male population can exert during a momentary hold grip[1] [61].

---

[1] As "hold grip" is intended the hand action where the four long are fingers pushing the grasped object against the palm.

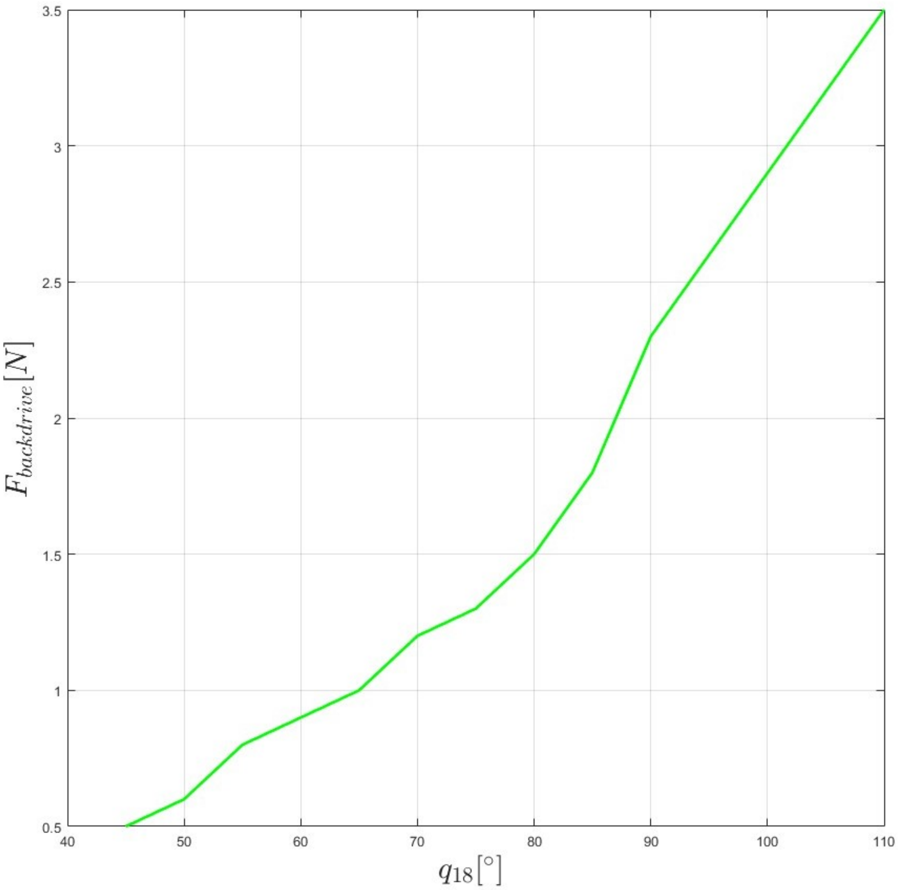

Figure 6.3: The measured backdrive force in N, as a function of crank angle (q_{18}) in deg, with a Bowden cable pretension between 2-3 Kg.

6.4 Dynamic model validation

Dedicated experimental tests were performed on a FM to validate the dynamic model described in Section 3.4, on which the HMI-force filter, described in Section 3.6, is based.

The protocol of the trial involved sampling the measurements provided by the load cell and encoder as the pose of the mechanism varies under the action of a known force at the end-effector.

With the goal of generating known downward-directed forces, the FM mounted on the adjustable-orientation-base bracket has been clamped in a vice and oriented so that the gravitational direction coincided with the y-axis of the global reference system, as reported in the Figure 6.2. The HMI-force direction taken as a reference for performing the experimental test is that performed by the Subject 1, according to the results reported in Section 3.2.

Weights of 1.5, 1.2, 1, 0.8, 0.6, 0.4, and 0.2 kilograms have been imposed at the end-effector. Sampling approximately every 10 degrees, at least eight different configurations were evaluated for each weight.

The sampled range of motion of the crank angle (q_{18}), considering the conventions described in Section 3.4, ranges from 110° up to 45°. Where $q_{18} = 110°$ and $q_{18} = 45°$ corresponds, respectively, to the complete opening and closing of the finger.

The collected data ($\hat{H}$), reported in Figure **??** and shown in Figure 6.4, have then been compared to those calculated by Equation 3.14 ($\tilde{H}$), introduced in the Section 6.4. Afterward, the percent error ($e_{\%}$) has been calculated for each of the load condition, using Equation 6.1, and collected in Table 6.1.

$$e_{\%} = \frac{\tilde{H} - \hat{H}}{\tilde{H}} \cdot 100 \tag{6.1}$$

q_{18}	$e_{\%}^{0.2}$	$e_{\%}^{0.4}$	$e_{\%}^{0.6}$	$e_{\%}^{0.8}$	$e_{\%}^{1}$	$e_{\%}^{1.2}$	$e_{\%}^{1.5}$
110	3.0	3.1	11.8	3.2	2.9	2.8	9.8
100	9.5	2.4	12.2	10.8	14.5	14.5	13.2
90	7.5	7.6	13.8	13.2	10.7	15.7	12.3
80	9.0	9.8	14.2	12.7	7.2	13.7	13.4
70	4.3	9.3	15.0	14.3	9.4	11.2	8.9
60	4.2	10.8	13.7	13.0	10.1	9.6	9.7
50	4.8	9.1	7.8	10.3	8.9	9.5	11.7
45	1.2	6.2	8.8	9.0	7.2	9.5	10.8

Table 6.1: Percentage error ($e_{\%}$) committed by the dynamic model. The number in superscript indicates the corresponding load in kilogram applied.

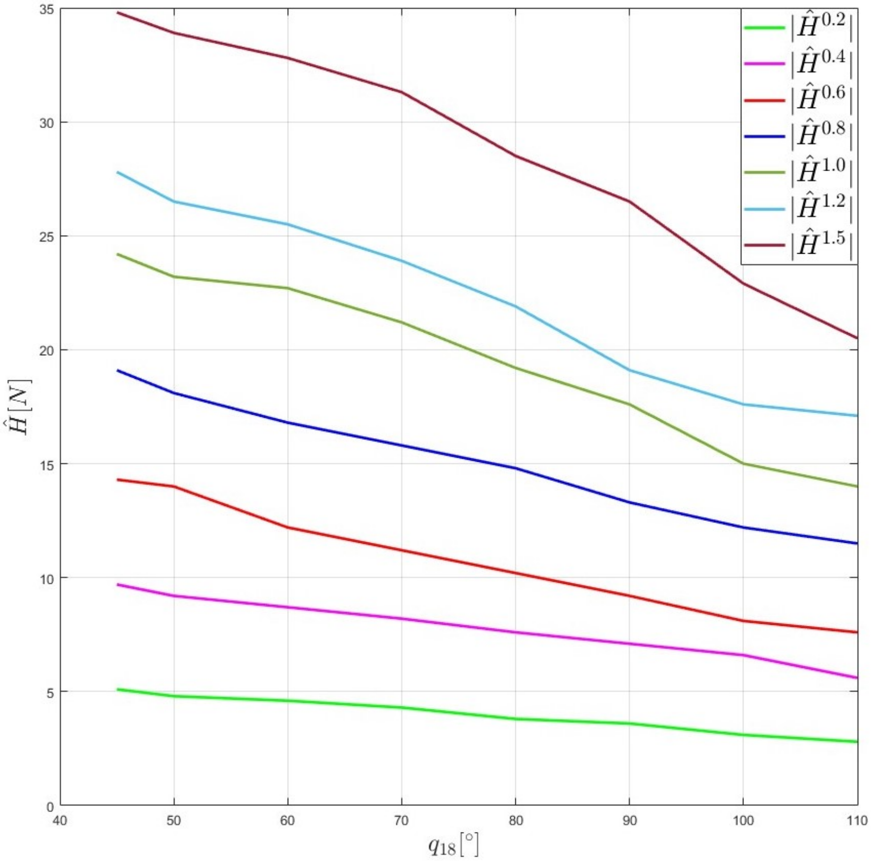

Figure 6.4: Force measured at joint H by the load cell ($\hat{H}$). The number in superscript indicates the corresponding load in kilogram applied.

6.4.1 Discussion of the dynamic model results

The results exhibited good performance of the dynamic model in H-reaction force reconstruction. All the tests performed a satisfying reproduction of the expected force profile, as visible in the Figure 6.5, with a percentage error between 1.2 and 15%. The discrepancy between the expected and empirically measured outcomes highlights, nonetheless, an important limitation of the model: the lack of friction effects modeling for the mechanical joints. For this reason, the measured force is always lower than the theoretical one, and there is a non-linearity within the system that leads to unpredictability of the percentage error magnitude committed in the measurement. Indeed, the results do not show a marked dependence of the error on the load magnitude or the mechanism pose. As a result, a potential evolution of the proposed work should involve modeling and introducing friction force at the joints aiming to further improve the accuracy of the HMI force reconstruction.

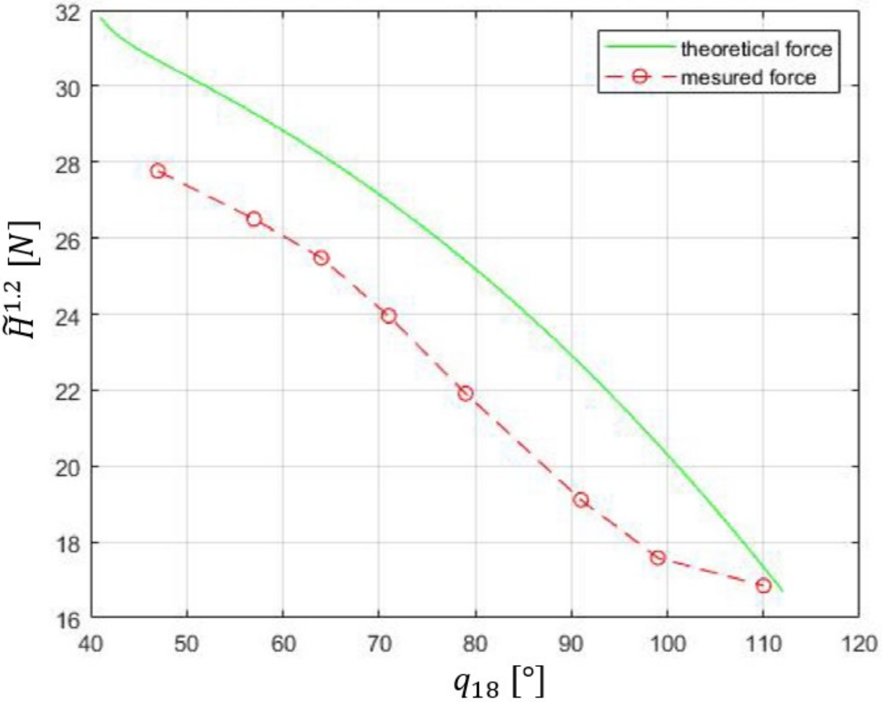

Figure 6.5: The dashed red line is the H-reaction profile measured; the green one, is the H-reaction calculated by the dynamic model.

6.5 HMI-force filter evaluation

Finally, experimental tests were carried out to evaluate the device accuracy in estimating the interaction force using the HMI-force filter, knowing that a portion of the error committed depends on the error in the dynamic model, estimated in previous Section, and a portion, instead, depends on the mathematical error inherent in the polynomial approximation, discussed in Subsection 3.6.1.

This test campaign uses the results from the experimental investigation presented for the dynamic model validation, introduced in Section 6.4, applying the HMI-force filter to the signal measured by the load cell to estimate the modulus of the weight force applied at the end-effector. Eight different configurations were evaluated for seven different weights from 0.2 to 1.5 kg. The results obtained are shown in Figure 6.6.

Table 6.2, on the other hand, shows the relative errors committed for each assessment, calculated by Equation 6.2

$$e_{\%} = \frac{mg - \hat{F_E}}{mg} \cdot 100 \tag{6.2}$$

where m is the weight of the sample applied at the end-effector, and g is the gravitational constant.

q_{18}	$e_{\%}^{0.2}$	$e_{\%}^{0.4}$	$e_{\%}^{0.6}$	$e_{\%}^{0.8}$	$e_{\%}^{1}$	$e_{\%}^{1.2}$	$e_{\%}^{1.5}$
110	2.6	1.6	11.7	0.3	3.1	0.7	5.1
100	6.1	-1.0	18.1	7.8	9.6	11.0	7.7
90	3.1	3.4	17.3	10.7	5.7	14.1	5.0
80	7.3	6.3	16.9	9.9	6.8	10.8	7.4
70	3.5	7.1	16.1	11.6	5.3	10.5	6.5
60	4.5	8.7	15.4	13.0	6.2	11.6	9.3
50	8.3	11.2	10.7	13.8	11.8	15.5	13.8
45	7.2	10.8	13.1	13.3	12.4	15.5	15.7

Table 6.2: Percentage error ($e_{\%}$) committed by HMI-force filter as the crank angle (q_{18}) and load applied change. The number in superscript indicates for each column the corresponding load in kilogram applied to the end-effector.

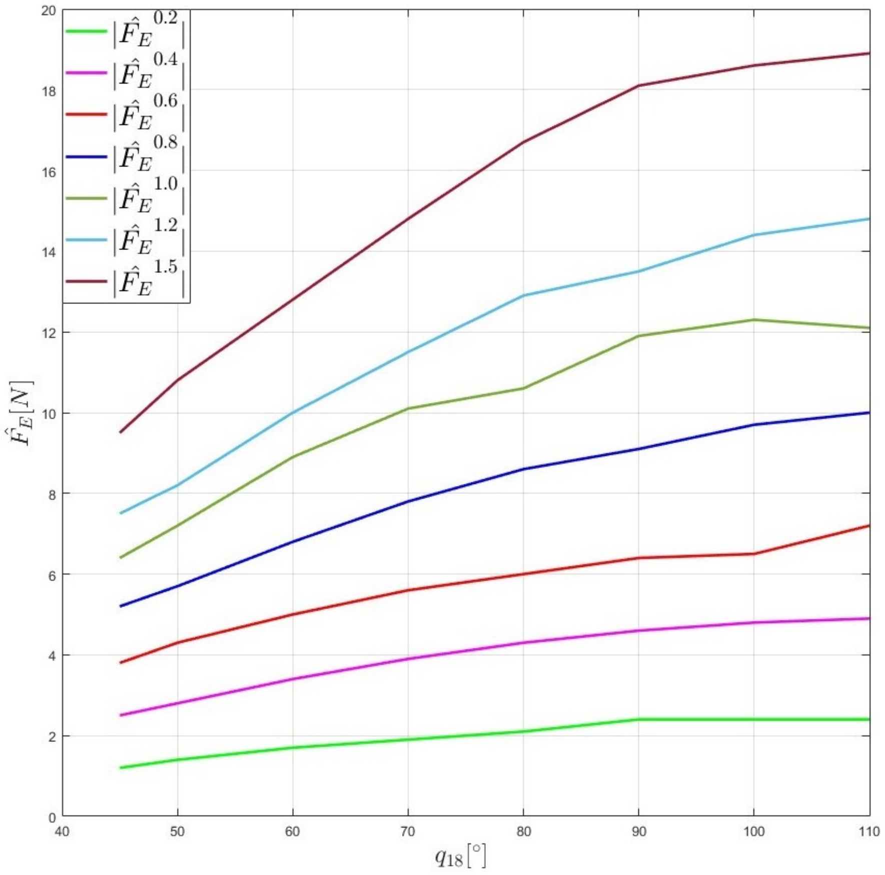

Figure 6.6: The module of the interface Force estimated by HMI-filter ($\hat{F_E}$) in Newton. The number in superscript indicates the corresponding load in kilogram applied to the end-effector.

6.5.1 Discussion of the HMI-force filter assessment

The experimental campaign conducted showed that the maximum percentage error committed by the HMI-filter is around 18%, which is in line with the error committed by the dynamic model. In light of this, it arises that the share of the error committed by the filter because of the dynamic model has a greater weight than the error due to the construction of polynomial approximation. Presumably, with the use of more accurate dynamic models, the degree of accuracy of the HMI-force filter can also be significantly improved. Nevertheless, the results obtained can be considered more than satisfactory for the presented application.

6.6 Test case assessment

A pilot study was conducted on a healthy user to evaluate the usability and ability of the presented device in replicating the force tracking required during the performance of the Catch the mole serious game. Figure 6.7 shows a recording of the interaction force of a finger during the performance of two catches in the Catch the Mole application. The green line represents the interaction force measured by the exoskeleton, while the red line represents the reference force from 0 N, when no interaction with the mole is recorded in the application, to 8 N during the capture mode. The blue horizontal lines identify the average interaction force calculated during contact and the deviations from the reference, denoted by Δe, which indicate the accuracy with which the device replicates the desired force. Also reported are the device reaction time intervals Δt, calculated as the difference between the instant of contact initiation or cessation and when the device achieves the desired interaction force. With the goal of deriving values of Δe and Δt, with a minimum statistical significance, 30 captures were evaluated, obtaining normal distributions of these parameters with mean value and standard deviation reported in Table 6.3. The results obtained can be considered more than satisfactory for a rehabilitation application, being a kinaesthetic application with not excessively stringent demands for accuracy and responsiveness.

Parameter	**Average value**	**Standard deviation**
Δe	0.7 N	0.3 N
Δt	0.5 s	0.4 s

Table 6.3: the average value and the standard deviation of Δe and Δt parameters. Δe indicates the error from the reference value, Δt the exoskeleton reaction time.

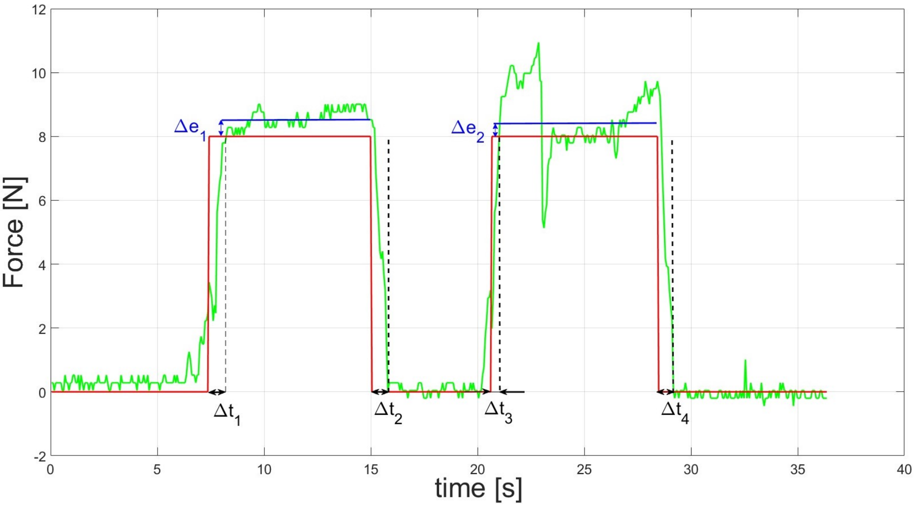

Figure 6.7: Interaction force tracking during two captures in the Catch the Mole application. The green lines shows the force measured by the exoskeleton, while the red line indicates the reference signal.

6.7 Pilot test at Don Carlo Gnocchi Foundation

A general assessment of the presented device was carried out at the Don Carlo Gnocchi Foundation Rehabilitation Centre by physiotherapists (Figure 6.8) via a pilot test conducted on the operators themselves.

Physiotherapists were asked to wear the exoskeleton with the actuation system off to evaluate the donning phase, wearability, and feasibility of use with real patients. After that, the operators were made to try the system in combination with the serious game *Catch the Mole*, completing at least 15 minutes of augmented rehabilitation session.

The impressions collected after the pilot test on the wearability and usability of the device were strongly positive, mainly due to the freedom of movement left to the wrist and the introduction of a thumb mechanism that allows a smooth and natural movement of the thumb. The device under review allows the opponent movement of the thumb with all long fingers allowing the user to perform a variety of precision grips. However, operators pointed out the need to manage Bowden cable sheaths, which with their weight and stiffness can encumber the user. The device during operation with serious game received excellent feedback both in terms of engagement in the rehabilitation session and at the performance level. Physiotherapists were remarkably impressed both with the transparency of the system during non-interaction in the serious game and with the high level of force achievable by the device during the capture phase.

The generally positive outcome of this pilot test was the final step toward field testing. The organization of such a campaign is, at the time of writing this text, the subject of work of the MDM Lab.

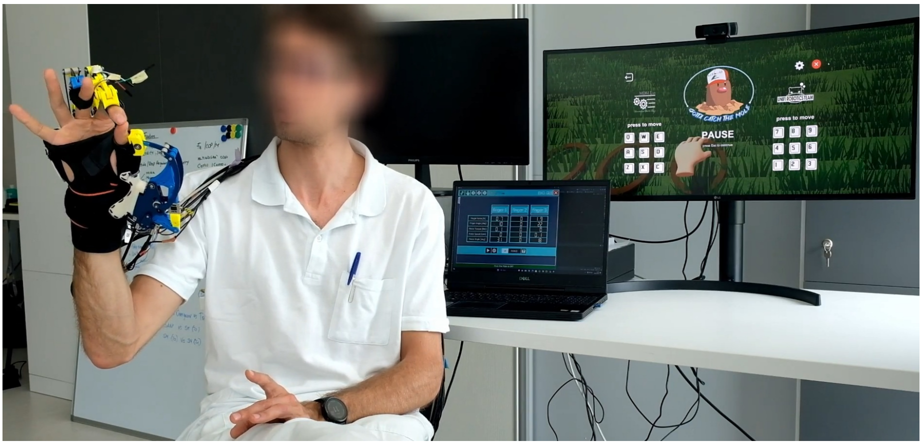

Figure 6.8: Pilot test at Don Carlo Gnocchi Foundation Rehabilitation Center.

Chapter 7

Conclusions

This work collects part of the research activities on wearable robotics carried out at the Mechatronics and Dynamic Modeling Laboratory of the Department of Industrial Engineering of the University of Florence from 2019 to 2022. What is reported in these pages focused, in particular, on the development of a novel kinaesthetic hand exoskeleton prototype for grasping and manipulation rehabilitation, augmented with force stimuli coming from serious games or virtual reality. Such Ph.D. research aims to address the need to develop innovative devices in the robot-augmented therapy field to improve rehabilitation outcomes.

The work undertaken benefited from the know-how in designing and producing rigid exoskeletons gained by MDM lab since 2013, employing the MDM kinematics along with the kinematic optimization algorithm in developing the new prototype, presented and discussed in Chapter 2. These two crucial achievements represented solid foundations in the design phase to realize a clinically safe and reliable device for working in close contact with human hands. Via a careful study of the latest technologies in the state of the art of exoskeleton haptic systems, disclosed in depth in Chapter 1, the technical specifications and desired features were selected to design a device with unique potential and characteristics. This research led toward a solution featuring a novel modular-design-based hand exoskeleton, outlined in Chapter 3, and a remote actuation system based on Bowden-cable transmission, detailed in Chapter 4. The choice fell on this type of layout to realize a device capable of exerting a considerable HMI force per finger (up to 15 N) while maintaining the perceived weight contained (lower 400 g). Further design criteria include the preservation of backdrivable movement and the implementation of quick couplings to provide a safer device and address the change-user-size issue.

The FM mechanism was equipped with appropriate sensors to measure force and pose by load cell and encoder sensors, respectively, pursuing the goal of realizing a kinaesthetic device. The force measurement is necessary to control the device as a reference signal, and the encoder measures are essential to reconstruct the hand pose within virtual reality. Due to functional and feasibility reasons, the load cell was integrated within the rod, as a consequence, it only provides an indirect measure of the interaction force. A special HMI-force filter was developed using the system's kinematic and dynamic models to improve the rendering of the interaction force from virtual reality.

In this work, the issues arising from the non-linearities introduced by the Bowden cables have been tackled by placing sensors (i.e., magnetic encoders and load cells) directly on the wearable part. Nevertheless, it is mandatory to point out that if, on one side, the choice of integrating sensors directly on the wearable part of the system allows to neglect (at least in first instance) the non-linearities of Bowden cables, on the other side, it leads to an increase in both the number and complexity of components, making manufacturability much more complicated. Successfully embedding sensors within the RAS using appropriate control strategies to estimate or predict and, then, counteract Bowden cable behavior is an interesting research challenge with enormous potential that could significantly improve this study.

The tests conducted on the prototype, described in Chapter 6, were designed to extrapolate some crucial features of the system, i.e., assessment of rapid coupling performance, and detection of the minimum backdrivability force. Also, others essential characteristics, i.e., the HMI reconstruction accuracy and the quality of the dynamic model, have been deeply investigated to validate the entire design process and lay the basis for future developments. Finally, as disclosed in Chapter 5, the efforts were mainly focused on the design of the software architecture of the device to impose the desired control strategy based on force feedback, along with the extrapolation and saving of sensitive data. A dedicated GUI for handling a single finger, as a workbench for the development and testing phase, was developed for real-time control and monitoring of the system to make the system usable to a clinical operator, not necessarily with a technical background. Lastly, a serious game was developed in UNITY environment to stimulate and train the sensorimotor apparatus necessary to perform the kinaesthetic gesture of spherical closing grasping by executing a special serious game designed to enhance user involvement.

Although the presented study is at a preliminary stage, the first results showed promising outcomes about the feasibility and usability of the HES proposed. With its high level of deliverable force, high wearability, and quick and easy reconfiguration process, the presented prototype has the potential to enrich the state of the art of kinaesthetic hand devices and represents an interesting application in wearable robotics field.

Natural continuations of the research activity carried out thus far will be to implement the simultaneous handling of multiple fingers, evaluate the device's effectiveness in practice via dedicated clinical trial, and develop a control strategy to render HMI-force profile instead of only step signal.

List of publications

International journals:

1. **Bartalucci, L.**, Secciani, N., Brogi, C., Topini, A., Della Valle, A., Ridolfi, A., and Allotta, B. (2023). An original mechatronic design of a kinaesthetic hand exoskeleton for virtual reality-based applications. *Mechatronics*, 90, 102947
2. Topini, A., Sansom, W., Secciani, N., **Bartalucci, L.**, Ridolfi, A., and Allotta, B. (2022). Variable admittance control of a hand exoskeleton for virtual reality-based rehabilitation tasks. *Frontiers in neurorobotics*, 15, 188

International conferences:

1. **Bartalucci, L.**, Secciani, N., Gelli, J., Valle, A. D., Ridolfi, A., and Allotta, B. (2021). Rehabilitative hand exoskeleton system: a new modular mechanical design for a remote actuated device. *In Advances in Italian Mechanism Science: Proceedings of the 3rd International Conference of IFToMM Italy 3 (pp. 128-136).* Springer International Publishing
2. **Bartalucci, L.**, Cavuoti, C., Secciani, N., Gelli, J., Della Valle, A., Allotta, B., and Ridolfi, A. (2021, October). 3D-Printing-Oriented Mechanical Redesign of a Hand Exoskeleton System for Rehabilitative Tasks. *In 2021 6th International Conference on Biomedical Imaging, Signal Processing (pp. 51-57)*
3. **Bartalucci, L.**, Bianchi, M., Meli, E., Ridolfi, A., Rindi, A., and Secciani, N. (2022). A Topology-Optimization-Based Design Methodology for Wearable Robots: Implementation and Application. *In Wearable Robotics: Challenges and Trends: Proceedings of the 5th International Symposium on Wearable Robotics, WeRob2020, and of WearRAcon Europe 2020, October 13–16, 2020 (pp. 493-497).* Springer International Publishing
4. Brogi, C., Secciani, N., **Bartalucci, L.**, Pagliai, M., Allotta, B., Ridolfi, A., and Rindi, A. (2022, June). Wearable Exoskeletons for Hand Assistance: Concept and Design of a Thumb Module with Hybrid Architecture. *In ROMANSY 24-Robot Design, Dynamics and Control: Proceedings of the 24th CISM IFToMM Symposium (pp. 70-78).* Cham: Springer International Publishing

5. Fredducci, C., Liverani, G., Bucci, A., Gelli, J., **Bartalucci, L.**, Ruscio, F. and Ridolfi, A. (2022, August). Mechatronic Design of an Underwater Multisensor System for Optical Data Acquisition. *In Advances in Italian Mechanism Science: Proceedings of the 4th International Conference of IFToMM Italy (pp. 787-794)*

Patent:

1. Scoglio A., Cappiello G., Mazzoleni S., Ridolfi A., Allotta B., Gelli J., **Bartalucci, L.**, Bianchi M., Secciani N., and Della Valle A. Modular exoskeleton system. International publication number WO2021/152523A1

References

[1] G. L. Tortorella, F. S. Fogliatto, A. Mac Cawley Vergara, R. Vassolo, and R. Sawhney, “Healthcare 4.0: trends, challenges and research directions,” *Production Planning & Control*, vol. 31, no. 15, pp. 1245–1260, 2020.

[2] A. C. B. Monteiro, R. P. França, V. V. Estrela, Y. Iano, A. Khelassi, and N. Razmjooy, “Health 4.0: applications, management, technologies and review,” *Medical Technologies Journal*, vol. 2, no. 4, pp. 262–276, 2018.

[3] G. Yang, Z. Pang, M. J. Deen, M. Dong, Y.-T. Zhang, N. Lovell, and A. M. Rahmani, “Homecare robotic systems for healthcare 4.0: visions and enabling technologies,” *IEEE journal of biomedical and health informatics*, vol. 24, no. 9, pp. 2535–2549, 2020.

[4] R. A. R. C. Gopura, K. Kiguchi, and D. S. V. Bandara, “A brief review on upper extremity robotic exoskeleton systems,” in *2011 6th International Conference on Industrial and Information Systems*, pp. 346–351, Aug 2011.

[5] Z. Lovrenovic and M. Doumit, “Review and analysis of recent development of lower extremity exoskeletons for walking assist,” in *2016 IEEE EMBS International Student Conference (ISC)*, pp. 1–4, May 2016.

[6] C. Toledo, L. Leija, R. Munoz, A. Vera, and A. Ramirez, “Upper limb prostheses for amputations above elbow: A review,” in *2009 Pan American Health Care Exchanges*, pp. 104–108, March 2009.

[7] J. D. Weiland and M. S. Humayun, “Retinal prosthesis,” *IEEE Transactions on Biomedical Engineering*, vol. 61, pp. 1412–1424, May 2014.

[8] G. P. Mylonas, V. Vitiello, T. P. Cundy, A. Darzi, and G. Yang, “Cyclops: A versatile robotic tool for bimanual single-access and natural-orifice en-

doscopic surgery," in *2014 IEEE International Conference on Robotics and Automation (ICRA)*, pp. 2436–2442, May 2014.

[9] G. J. Kim *et al.*, "A swot analysis of the field of virtual reality rehabilitation and therapy," *Presence*, vol. 14, no. 2, pp. 119–146, 2005.

[10] H. Sveistrup, "Motor rehabilitation using virtual reality," *Journal of neuroengineering and rehabilitation*, vol. 1, no. 1, pp. 1–8, 2004.

[11] K. S. Gurusamy, R. Aggarwal, L. Palanivelu, and B. R. Davidson, "Virtual reality training for surgical trainees in laparoscopic surgery," *Cochrane database of systematic reviews*, no. 1, 2009.

[12] E. Van Wyk and R. De Villiers, "Virtual reality training applications for the mining industry," in *Proceedings of the 6th international conference on computer graphics, virtual reality, visualisation and interaction in Africa*, pp. 53–63, 2009.

[13] K.-C. Siu, B. J. Best, J. W. Kim, D. Oleynikov, and F. E. Ritter, "Adaptive virtual reality training to optimize military medical skills acquisition and retention," *Military medicine*, vol. 181, no. suppl_5, pp. 214–220, 2016.

[14] G. Chryssolouris, D. Mavrikios, M. Pappas, E. Xanthakis, and K. Smparounis, "A web and virtual reality-based platform for collaborative product review and customisation," in *Collaborative design and planning for digital manufacturing*, pp. 137–152, Springer, 2009.

[15] R. Stark, S. Kind, and S. Neumeyer, "Innovations in digital modelling for next generation manufacturing system design," *CIRP annals*, vol. 66, no. 1, pp. 169–172, 2017.

[16] M. Macchini, M. Lortkipanidze, F. Schiano, and D. Floreano, "The impact of virtual reality and viewpoints in body motion based drone teleoperation," *arXiv preprint arXiv:2102.00226*, 2021.

[17] J. Cui, S. Tosunoglu, R. Roberts, C. Moore, and D. W. Repperger, "A review of teleoperation system control," in *Proceedings of the Florida Conference on Recent Advances in Robotics*, pp. 1–12, Florida Atlantic University Boca Raton, FL, 2003.

[18] T. Zhou, Q. Zhu, and J. Du, "Intuitive robot teleoperation for civil engineering operations with virtual reality and deep learning scene reconstruction," *Advanced Engineering Informatics*, vol. 46, p. 101170, 2020.

[19] L. A. Nguyen, M. Bualat, L. J. Edwards, L. Flueckiger, C. Neveu, K. Schwehr, M. D. Wagner, and E. Zbinden, "Virtual reality interfaces for visualization and control of remote vehicles," *Autonomous Robots*, vol. 11, no. 1, pp. 59–68, 2001.

[20] T. Fong, C. Thorpe, and C. Baur, "Multi-robot remote driving with collaborative control," *IEEE Transactions on Industrial Electronics*, vol. 50, no. 4, pp. 699–704, 2003.

[21] B. Hannaford and A. M. Okamura, *Haptics*, pp. 1063–1084. Cham: Springer International Publishing, 2016.

[22] V. Z. Pérez Ariza and M. Santís-Chaves, "Haptic interfaces: kinesthetic vs. tactile systems," *Revista EIA*, no. 26, pp. 13–29, 2016.

[23] R. Traylor and H. Z. Tan, "Development of a wearable haptic display for situation awareness in altered-gravity environment: Some initial findings," in *Proceedings 10th Symposium on Haptic Interfaces for Virtual Environment and Teleoperator Systems. HAPTICS 2002*, pp. 159–164, IEEE, 2002.

[24] J. Lieberman and C. Breazeal, "Tikl: Development of a wearable vibrotactile feedback suit for improved human motor learning," *IEEE Transactions on Robotics*, vol. 23, no. 5, pp. 919–926, 2007.

[25] H. Kim, C. Seo, J. Lee, J. Ryu, S.-b. Yu, and S. Lee, "Vibrotactile display for driving safety information," in *2006 IEEE Intelligent Transportation Systems Conference*, pp. 573–577, IEEE, 2006.

[26] G.-H. Yang, K.-U. Kyung, M. A. Srinivasan, and D.-S. Kwon, "Quantitative tactile display device with pin-array type tactile feedback and thermal feedback," in *Proceedings 2006 IEEE International Conference on Robotics and Automation, 2006. ICRA 2006.*, pp. 3917–3922, IEEE, 2006.

[27] T.-H. Yang, S.-Y. Kim, C. H. Kim, D.-S. Kwon, and W. J. Book, "Development of a miniature pin-array tactile module using elastic and electromagnetic force for mobile devices," in *World Haptics 2009-Third Joint EuroHaptics conference and Symposium on Haptic Interfaces for Virtual Environment and Teleoperator Systems*, pp. 13–17, IEEE, 2009.

[28] I. Sarakoglou, N. Garcia-Hernandez, N. G. Tsagarakis, and D. G. Caldwell, "A high performance tactile feedback display and its integration in teleoperation," *IEEE Transactions on Haptics*, vol. 5, no. 3, pp. 252–263, 2012.

[29] G. Frediani and F. Carpi, “Tactile display of softness on fingertip,” *Scientific reports*, vol. 10, no. 1, pp. 1–10, 2020.

[30] D. Prattichizzo, F. Chinello, C. Pacchierotti, and M. Malvezzi, “Towards wearability in fingertip haptics: a 3-dof wearable device for cutaneous force feedback,” *IEEE Transactions on Haptics*, vol. 6, no. 4, pp. 506–516, 2013.

[31] A. G. Perez, D. Lobo, F. Chinello, G. Cirio, M. Malvezzi, J. San Martín, D. Prattichizzo, and M. A. Otaduy, “Soft finger tactile rendering for wearable haptics,” in *2015 IEEE World Haptics Conference (WHC)*, pp. 327–332, IEEE, 2015.

[32] C. A. Avizzano, M. Satler, G. Cappiello, A. Scoglio, E. Ruffaldi, and M. Bergamasco, “Motore: A mobile haptic interface for neuro-rehabilitation,” in *2011 RO-MAN*, pp. 383–388, 2011.

[33] P. Lam, D. Hebert, J. Boger, H. Lacheray, D. Gardner, J. Apkarian, and A. Mihailidis, “A haptic-robotic platform for upper-limb reaching stroke therapy: Preliminary design and evaluation results,” *Journal of NeuroEngineering and Rehabilitation*, vol. 5, no. 1, pp. 1–13, 2008.

[34] I. Choi, E. W. Hawkes, D. L. Christensen, C. J. Ploch, and S. Follmer, “Wolverine: A wearable haptic interface for grasping in virtual reality,” in *2016 IEEE/RSJ International Conference on Intelligent Robots and Systems (IROS)*, pp. 986–993, 2016.

[35] I. Choi, H. Culbertson, M. R. Miller, A. Olwal, and S. Follmer, “Grabity: A wearable haptic interface for simulating weight and grasping in virtual reality,” in *Proceedings of the 30th Annual ACM Symposium on User Interface Software and Technology*, pp. 119–130, 2017.

[36] J. C. Perry, J. Rosen, and S. Burns, “Upper-limb powered exoskeleton design,” *IEEE/ASME transactions on mechatronics*, vol. 12, no. 4, pp. 408–417, 2007.

[37] C. Carignan, J. Tang, and S. Roderick, “Development of an exoskeleton haptic interface for virtual task training,” in *2009 IEEE/RSJ International Conference on Intelligent Robots and Systems*, pp. 3697–3702, IEEE, 2009.

[38] S. Roderick, M. Liszka, and C. Carignan, “Design of an arm exoskeleton with scapula motion for shoulder rehabilitation,” in *ICAR’05. Proceedings., 12th International Conference on Advanced Robotics, 2005.*, pp. 524–531, IEEE, 2005.

[39] A. Montagner, A. Frisoli, L. Borelli, C. Procopio, M. Bergamasco, M. C. Carboncini, and B. Rossi, "A pilot clinical study on robotic assisted rehabilitation in vr with an arm exoskeleton device," in *2007 Virtual Rehabilitation*, pp. 57–64, IEEE, 2007.

[40] D. H. de la Iglesia, A. S. Mendes, G. V. González, D. M. Jiménez-Bravo, and J. F. de Paz Santana, "Connected elbow exoskeleton system for rehabilitation training based on virtual reality and context-aware," *Sensors*, vol. 20, no. 3, p. 858, 2020.

[41] C. Pan, Z. Lin, P. Sun, C. Chang, S. Wang, C. Yen, and Y. Yang, "Design of virtual reality systems integrated with the lower-limb exoskeleton for rehabilitation purpose," in *2018 IEEE International Conference on Applied System Invention (ICASI)*, pp. 498–501, IEEE, 2018.

[42] H. K. Yap, J. H. Lim, F. Nasrallah, and C.-H. Yeow, "Design and preliminary feasibility study of a soft robotic glove for hand function assistance in stroke survivors," *Frontiers in neuroscience*, vol. 11, p. 547, 2017.

[43] S. Baik, S. Park, and J. Park, "Haptic glove using tendon-driven soft robotic mechanism," *Frontiers in bioengineering and biotechnology*, vol. 8, p. 541105, 2020.

[44] A. Mohammadi, J. Lavranos, P. Choong, and D. Oetomo, "Flexo-glove: a 3d printed soft exoskeleton robotic glove for impaired hand rehabilitation and assistance," in *2018 40th Annual International Conference of the IEEE Engineering in Medicine and Biology Society (EMBC)*, pp. 2120–2123, IEEE, 2018.

[45] A. Borboni, M. Mor, and R. Faglia, "Gloreha—hand robotic rehabilitation: Design, mechanical model, and experiments," *Journal of Dynamic Systems, Measurement, and Control*, vol. 138, no. 11, 2016.

[46] M. Malvezzi, T. L. Baldi, A. Villani, F. Ciccarese, and D. Prattichizzo, "Design, development, and preliminary evaluation of a highly wearable exoskeleton," in *2020 29th IEEE International Conference on Robot and Human Interactive Communication (RO-MAN)*, pp. 1055–1062, IEEE, 2020.

[47] Y. Park, I. Jo, J. Lee, and J. Bae, "A dual-cable hand exoskeleton system for virtual reality," *Mechatronics*, vol. 49, pp. 177–186, 2018.

[48] J. Arata, K. Ohmoto, R. Gassert, O. Lambercy, H. Fujimoto, and I. Wada, "A new hand exoskeleton device for rehabilitation using a three-layered sliding spring mechanism," in *2013 IEEE International Conference on Robotics and Automation*, pp. 3902–3907, IEEE, 2013.

[49] M. Fontana, S. Fabio, S. Marcheschi, and M. Bergamasco, "Haptic hand exoskeleton for precision grasp simulation," *Journal of Mechanisms and Robotics*, vol. 5, no. 4, 2013.

[50] I. Sarakoglou, A. Brygo, D. Mazzanti, N. G. Hernandez, D. G. Caldwell, and N. G. Tsagarakis, "Hexotrac: A highly under-actuated hand exoskeleton for finger tracking and force feedback," in *2016 IEEE/RSJ International Conference on Intelligent Robots and Systems (IROS)*, pp. 1033–1040, IEEE, 2016.

[51] I. Jo and J. Bae, "Design and control of a wearable hand exoskeleton with force-controllable and compact actuator modules," in *2015 IEEE International Conference on Robotics and Automation (ICRA)*, pp. 5596–5601, IEEE, 2015.

[52] N. Secciani, C. Brogi, M. Pagliai, F. Buonamici, F. Gerli, F. Vannetti, M. Bianchini, Y. Volpe, and A. Ridolfi, "Wearable robots: An original mechatronic design of a hand exoskeleton for assistive and rehabilitative purposes," *Frontiers in Neurorobotics*, vol. 15, 2021.

[53] F. Zhang, L. Hua, Y. Fu, H. Chen, and S. Wang, "Design and development of a hand exoskeleton for rehabilitation of hand injuries," *Mechanism and Machine Theory*, vol. 73, pp. 103–116, 2014.

[54] S. Ueki, H. Kawasaki, S. Ito, Y. Nishimoto, M. Abe, T. Aoki, Y. Ishigure, T. Ojika, and T. Mouri, "Development of a hand-assist robot with multi-degrees-of-freedom for rehabilitation therapy," *IEEE/ASME Transactions on mechatronics*, vol. 17, no. 1, pp. 136–146, 2010.

[55] C. N. Schabowsky, S. B. Godfrey, R. J. Holley, and P. S. Lum, "Development and pilot testing of hexorr: hand exoskeleton rehabilitation robot," *Journal of neuroengineering and rehabilitation*, vol. 7, no. 1, pp. 1–16, 2010.

[56] H. K. Yap, J. H. Lim, F. Nasrallah, J. C. Goh, and R. C. Yeow, "A soft exoskeleton for hand assistive and rehabilitation application using pneumatic actuators with variable stiffness," in *2015 IEEE international conference on robotics and automation (ICRA)*, pp. 4967–4972, IEEE, 2015.

[57] A. P. Tjahyono, K. C. Aw, H. Devaraj, W. Surendra, E. Haemmerle, and J. Travas-Sejdic, "A five-fingered hand exoskeleton driven by pneumatic artificial muscles with novel polypyrrole sensors," *Industrial Robot: An International Journal*, 2013.

[58] J. Li, R. Zheng, Y. Zhang, and J. Yao, "ihandrehab: An interactive hand exoskeleton for active and passive rehabilitation," in *2011 IEEE International Conference on Rehabilitation Robotics*, pp. 1–6, IEEE, 2011.

[59] Y. Yun, P. Agarwal, J. Fox, K. E. Madden, and A. D. Deshpande, "Accurate torque control of finger joints with ut hand exoskeleton through bowden cable sea," in *2016 IEEE/RSJ International Conference on Intelligent Robots and Systems (IROS)*, pp. 390–397, IEEE, 2016.

[60] A. Wege, K. Kondak, and G. Hommel, "Mechanical design and motion control of a hand exoskeleton for rehabilitation," in *IEEE International Conference Mechatronics and Automation, 2005*, vol. 1, pp. 155–159, IEEE, 2005.

[61] NASA, "Nasa-std-3000 the man-system integration standards, revision b july 1995," 1995.

[62] M. Bianchi, F. Fanelli, E. Meli, A. Ridolfi, F. Vannetti, M. Bianchini, and B. Allotta, "Optimization-based scaling procedure for the design of fully portable hand exoskeletons," *Meccanica*, vol. 53, no. 11, pp. 3157–3175, 2018.

[63] S. Andrea, C. Giovanni, M. Stefano, A. Ridolfi, B. Allotta, J. Gelli, L. Bartalucci, M. Bianchi, N. Secciani, A. DELLA VALLE, *et al.*, "Sistema esoscheletrico modulare," 2020.

[64] E. Pennestrì, "Dinamica tecnica e computazionale-sistemi multibody," 2002.